POLITECNICO
MILANO 1863

SCUOLA DI INGEGNERIA INDUSTRIALE
E DELL'INFORMAZIONE

Light-induced Floquet states with few-femtosecond pulses

Tesi di Laurea Magistrale in
Engineering Physics - Ingegneria Fisica

Author: **Matteo Talarico**

Student ID: 944666
Advisor: Prof. Matteo Lucchini
Co-advisors: Dr. Fabio Medeghini
Academic Year: 2020-21

Abstract

Floquet theory was introduced to aid the study of periodical systems. A laser impinging onto a material is able to provide this periodicity. Yet, some applications such as ultrafast pump-probe spectroscopy require few-cycle pulses, which can be so short (few femtoseconds) to be no longer periodic. In this thesis we wish to verify whether Floquet theory may still be applied in the case of ultrashort pulses. We employ a pump-probe spectroscopy technique on a Ne gas target. Two sets of pulses are produced: the probe, in the extreme-ultraviolet (XUV) range, and the pump, in the infrared (IR) region. Our aim is to verify the system behaviour as a function of the IR intensity for long IR pulses, and to investigate the effect of a finite driving pulse on the induced Floquet states. In our setup, the probe is generated through High-order Harmonic Generation and selected through a Time Delay-Compensated Monochromator. The pump passes through a hollow-core fibre compression setup and through a delay stage. The two beams meet in a Time-of-Flight spectrometer, where the XUV pulses ionise the gas, producing free electrons which constitute the main band, and the IR beam dresses the states of the systems, generating multiple sidebands. When this is done for many time delays, it results in a spectrogram, which is analysed together with the figures of merit of the two beams. One of the methods employed to retrieve the pulse characteristics is a custom algorithm named STRIPE. Then, we study the theoretical aspect of the problem, starting from the Strong Field Approximation and performing a frequency expansion considering Gaussian pulses. In the long IR range we describe sideband amplitudes with generalised Bessel functions depending on the IR intensity. In the short IR range, we find that the amplitude of the dressed states decreases with short IR pulses. When comparing these descriptions to the acquired data, we find a good agreement (aside from a correction factor) in the long IR range. In the short IR range we can reconstruct the general trend through STRIPE, but the actual values are different due to unforeseen variations in IR intensity and wavelength, which can be accounted for in a more sophisticated data analysis. This work will impact the study of Floquet engineering and of the ultrafast behaviour of novel materials for electronics.

Keywords: Floquet theory, pump-probe, femtosecond pulses, ultrafast optics, laser physics

Abstract in lingua italiana

La teoria di Floquet fu introdotta per lo studio di sistemi periodici, come quelli generati da un laser incidente su un materiale. Tuttavia, alcune applicazioni come gli esperimenti di pompa-sonda ultraveloci richiedono impulsi a pochi cicli, che risultano così brevi (pochi femtosecondi) da non essere più periodici. In questa tesi verificheremo se la teoria di Floquet possa essere ancora applicata in caso di impulsi ultrabrevi. Impieghiamo una tecnica di spettroscopia pompa-sonda su un bersaglio di Ne in stato di gas. Vengono generati due set di impulsi: la sonda nell'estremo ultravioletto (XUV), e la pompa nell'infrarosso (IR). Il nostro scopo è verificare il comportamento del sistema in funzione dell'intensità dell'IR per impulsi IR lunghi, e indagare l'effetto di impulsi finiti sugli stati di Floquet indotti. Nel setup, la pompa è prodotta tramite generazione di armoniche di ordine elevato e selezionata da un monocromatore compensato in tempo. La sonda invece passa attraverso un sistema di compressione a fibra cava e un ritardatore. I due fasci si incontrano in uno spettrometro a tempo di volo, in cui gli impulsi XUV ionizzano il gas, creando elettroni liberi che compongono la banda principale, e il fascio IR veste gli stati del sistema, popolando più bande laterali. Se svolto per più ritardi temporali ciò genera uno spettrogramma, analizzato assieme alle figure di merito dei due fasci. Uno dei metodi impiegati per ricavare le caratteristiche degli impulsi è un apposito algoritmo chiamato STRIPE. Andiamo poi a studiare l'aspetto teorico del problema iniziando dall'Approssimazione di Campo Forte per poi eseguire un'espansione in frequenza considerando impulsi gaussiani. Per impulsi IR lunghi possiamo descrivere le ampiezze delle bande con funzioni generalizzate di Bessel dipendenti dall'intensità dell'IR. Per impulsi IR brevi troviamo una decrescita di ampiezze degli stati vestiti a durate più brevi. Comparando queste descrizioni con i dati acquisiti abbiamo un buon accordo (a meno di un fattore correttivo) per impulsi IR lunghi. Per impulsi IR brevi riusciamo a ricostruire l'andamento generale attraverso STRIPE, ma i valori effettivi sono differenti a causa di variazioni impreviste di lunghezza d'onda e intensità dell'IR. Questo lavoro avrà un impatto sull'ingegneria di Floquet e lo studio del comportamento ultraveloce di nuovi materiali per l'elettronica.

Parole chiave: teoria di Floquet, pompa-sonda, impulsi nei femtosecondi, ottica ultraveloce, fisica dei laser

Contents

Introduction

0.1. Floquet theory

Floquet theory was develped by Gaston Floquet in the late 19th century. [11]. This theory is vastly useful in the treatment of linear differential equations with periodic coefficients, and lends itself to the description of numerous physical phenomena which present a periodicity, as we are going to see in this introductory chapter.

The most relevant result of this theory is the aptly-named *Floquet theorem* (sometimes also referred to as Floquet-Lyapunov theorem), first written by Floquet himself in 1883 [16]. It states that even though they might not retain the exact periodicity of the coefficients, the solutions to such differential equations can nonetheless be written as the product of a function with that same periodicity and a constant phase term.

In more mathematical terms [6], we can start by considering the following linear differential equation, also called *Floquet system*

$$\dot{\mathbf{x}}(t) = \mathbf{A}(t) \cdot \mathbf{x}(t) \tag{0.1.1}$$

where the derivative of $\mathbf{x}(t)$ is indicated as $\dot{\mathbf{x}}(t)$, and $\mathbf{A}(t)$ is a piecewise continuous function which is periodic in t with a period T, so that we can write

$$\mathbf{A}(t) = \mathbf{A}(t + T)$$

If we wish to solve this kind of equation, the Floquet theorem states that given the fundamental matrix $\mathbf{\Phi}(t)$ that is a solution of the previous system of Eq. (0.1.1) in $\mathbf{x}(t)$, it must not be periodic in itself, yet needs to assume the form of

$$\mathbf{\Phi}(t) = \mathbf{P}(t) \cdot e^{\mathbf{B}t} \tag{0.1.2}$$

where it is the factor $\mathbf{P}(t)$ to hold the actual periodicity in t, therefore making it possible

to write

$$\mathbf{P}(t) = \mathbf{P}(t+T)$$

and the matrix $\mathbf{B}$ is a complex matrix.

An analogous form of writing Eq. (0.1.2) is also

$$\mathbf{\Phi}(t+T) = \mathbf{\Phi}(t) \cdot e^{\mathbf{B}T} \tag{0.1.3}$$

This was the principal formulation of the Floquet theorem, which can be applied in classical mechanics in various cases. For instance, it is fundamental to demonstrate the stability and behaviour of certain systems, such as the abruptly driven classical oscillator, or the harmonically driven classical oscillator [22, 41].

Yet, it may also be adapted to quantum mechanics, where the majority of applications lie. If we consider the Hamiltonian $\hat{H}(t)$ inside the *Time-Dependent Schrödinger Equation* (TDSE) [34, 41]

$$i\hbar\frac{\partial}{\partial t}\left|\psi(t)\right\rangle = \hat{H}(t)\left|\psi(t)\right\rangle$$

then we may write that the Floquet theorem applies whenever $\hat{H}(t) = \hat{H}(t+T)$, where $T = \frac{2\pi}{\omega_F}$ and ω_F is the *Floquet frequency*, i.e. whenever the system is periodically driven (linearity is already guaranteed from the beginning in the TDSE). Hence, in this intance Eq. (0.1.2) can be interpreted as follows

$$\left|\psi(t)\right\rangle = \left|\phi(t)\right\rangle e^{-i\epsilon t} \tag{0.1.4}$$

where ϵ is the so-called *Floquet quasi-energy* and

$$\left|\phi(t)\right\rangle = \left|\phi(t+T)\right\rangle$$

Moreover, since $\left|\phi(t)\right\rangle$ is periodic, we may also expand it in series as follows:

$$\left|\phi(t)\right\rangle = \sum_{n=-\infty}^{+\infty} A_n e^{-in\omega t} \tag{0.1.5}$$

from which we have also

$$|\psi(t)\rangle = e^{-i\epsilon t} \sum_{n=-\infty}^{+\infty} A_n e^{-in\omega t} \tag{0.1.6}$$

and

$$\begin{aligned} \hat{H}(t) = \hat{H}(t+T) = \sum_{n=-\infty}^{+\infty} \hat{H}_n e^{in\omega t} \\ \hat{H}_n = \frac{1}{T}\int_0^T \hat{H}(t) e^{-in\omega t} dt \end{aligned} \tag{0.1.7}$$

The results of Eqs. (0.1.6) and (0.1.7) find application in a plethora of research areas, as we are going to see shortly.

It is worth noting that we only focused of a time-dependent Hamiltonian, but if we consider a dependence of $\hat{H}$ on space we obtain a parallel theorem pertaining to the realm of solid-state physics, *Bloch's theorem*. As may be known, crystals present a regular structure, with atoms disposed in a periodic configuration, thus generating a periodic potential. Bloch's theorem claims this periodicity causes the solution to the static Schrödinger equation to take the form of a *Bloch wave*, which is composed of plane waves modulated by a periodic function. Consequently, this theorem can be written in two analogous formulations:

$$\begin{aligned} \psi(\mathbf{r}) = u(\mathbf{r}) \cdot e^{i\mathbf{k}\cdot\mathbf{r}} \\ \psi(\mathbf{r}+\mathbf{R}) = \psi(\mathbf{r}) \cdot e^{i\mathbf{k}\cdot\mathbf{R}} \end{aligned} \tag{0.1.8}$$

where the latter representation is akin to that of Eq. (0.1.3), in which the periodicity is given by the spatial vector $\mathbf{R} = a_1 R_1 + a_2 R_2 + a_3 R_3$, which in turn has that R_i is the period in the direction $i = x, y, z$, and a_i is an integer number; on the other hand, in the first formula describing Bloch waves $u(\mathbf{r})$ is the function with period $\mathbf{R}$, so to have $u(\mathbf{r}+\mathbf{R}) = u(\mathbf{r})$. This solution resembles Eq. (0.1.2), and that is the reason why these solutions to the TDSE are also referred to as Floquet-Bloch Ansatz for the TDSE [11, 41].

Going back to a time-dependent Hamiltonian, countless systems are present which can be described by means of Floquet theory, especially from a quantum mechanics point of view. While many uses are also present in theoretical physics (see for example Floquet Supersymmetry, or FSUSY [19]), we are interested in a more applied approach.

We could start by mentioning a few applications in solid-state physics. For instance, Floquet topological insulators[1] (FTI) [26] are a topic of interest. It is in fact possible to induce a topological state in a semiconductor quantum well via microwave irradiation, without changing the structure of the well itself. By means of this time-periodic radiation it is feasible to generate new differential operators with spectra of topological insulators, which exhibit peculiar properties especially in out-of-equilibrium conditions. In particular, it is possible to control the spectral properties of the surface states and rapidly vary the transport of electrons in these edge-states. This in turn may have a practical application in the creation of ultrafast switches, as seen in [23].

A further relevant application is found in solid-state nuclear magnetic resonance (NMR) spectroscopy [3, 20]. Here in fact the Hamiltonian of the system presents a time periodicity which is caused by the so-called magic-angle spinning (MAS)[2], which in turn generates sidebands in the analysed spectrum at multiples of the rotor frequency. These sidebands patterns (Figure 1), while not exactly straightforward to calculate, may be considerably simplified through the utilisation of Floquet theory, which allows for a Fourier series expansion of the periodic Hamiltonian and an overall ease of calculation.

Another way through which the Hamiltonian is rendered periodic and the sidebands are generated is shining RF (radio frequency) pulses or resonant oscillating radiation onto the sample. This leads us to realise that an analogous logic may be applied using optical frequencies and pulses in the far THz $\div$ PHz range. In fact, optics and spectroscopy are perfect candidates to apply Floquet theory.

[1] Topological insulators are materials which behave like insulators in their bulk, while still maintaining conductive states in the surface.

[2] Magic-angle spinning, or MAS, is a technique through which the orientational dependence of the NMR anisotropic interactions in solid-phase samples is eliminated by rapidly rotating the sample itself around an axis which is tilted at a particular angle (indeed, the magic angle). Read [38] for more details on the topic.

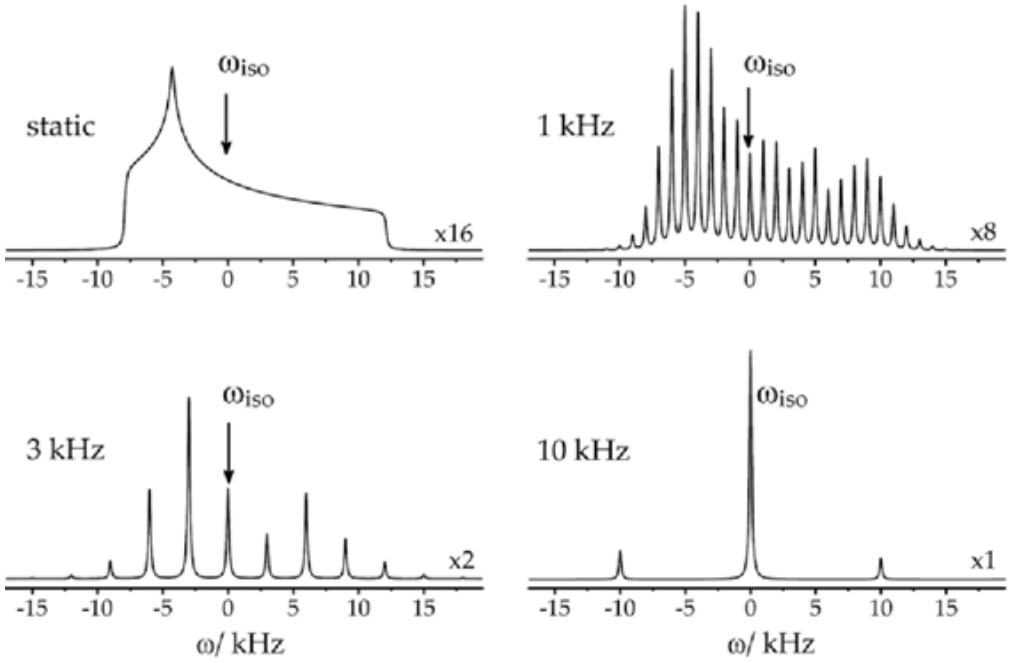

Figure 1: Simulation of MAS sideband pattern using Floquet theory. In this graph we are able to see how spinning the sample at different frequencies generates sidebands which are spaced with a different period which is proportional to the frequency itself. Therefore, the higher the frequency, the fewer the sidebands, and vice versa. From [14].

0.2. Floquet theory in Optics

With the rise in popularity of Floquet theory, a new branch of physics was born, called *Floquet engineering*. It consists in the manipulation and control of quantum systems via periodic driving, usually of the electromagnetic kind. Even though radio frequency waves or microwaves may be used, lasers too are able to provide such a periodicity, be it in continuous wave (CW) or in pulses. A few results of this discipline include Floquet engineering of band topology [21, 37], of quantum gases [4, 13, 50], of quantum materials [11, 37], or of the atomic light-shift [10].

On the topic of band topology, the concept is not unlike what we saw in the previous section regarding FTI. A main difference here is that circularly polarized laser radiation may be utilised instead of microwaves.

Concerning quantum gases, an interesting topic of study is found in the behaviour of ultra-cold atoms in optical lattices (or optical traps) such as the one that arises from the interference caused by two identical counter-propagating laser beams. If the frequency of one of the two beams gets periodically modulated, it is possible to periodically shake the

optical lattice. This would allow to engineer a new Hamiltonian with completely different properties which would not be available in that specific system or in any other static system. This yields consequences on topics like Bose-Einstein condensation, coherent resonant tunneling, and even topological band structures and insulators.

In a similar way, on the subject of quantum materials many phenomena can be described through Floquet theory and can benefit from Floquet engineering. Some examples include: signatures of light-induced or light-enhanced superconductivity, ultrafast switching of hidden electronic phases, phonon-induced magnetization, and ultrafast spintronics, on which we are going to spend a few words. Spintronics is a discipline which stems from the mixture of electronics and magnetism, and it employs the degrees of freedom of the spin of the electrons to transport and store information via spin current and magnetisation. Ultrafast spintronics, in addition, utilises the magnetic component of a laser to control spin and magnetism on a sub-picosecond ($< 10^{-12}$ s) time scale through Zeeman coupling. The idea of Floquet engineering in this case would be to apply a periodic Hamiltonian to the system, with different levels of approximation depending on the spin degrees of freedom.

Regarding the last matter of atomic light-shift, just like quantum gases it is of high relevance when treating optical traps, but it also results to be interesting to determine atomic properties for fundamental physics or in sensing applications. It is usually calculated by means of second-order perturbation theory. However, in considering the case of strong non-linearity and mixing of hyperfine energy levels, the use of another model is required. Indeed, a non-perturbative semiclassical theory based on Floquet's theorem may be successfully employed. Floquet theory can accurately describe light shifts due to multiple lasers of arbitrary polarization with wavelengths close to atomic resonances, being suitable to treat the issues of non-linearity and level mixing, and having a relatively simple mathematics which renders engineering the light-shift and its eventual compensation much easier.

It is worth noting that Floquet engineering cannot be applied in any case, three conditions [13] must apply for it to be a viable option for our purposes:

- the system must be suitable to be driven periodically in time;
- it must be well isolated from the environment so that dissipation processes happen on a much larger time scale than the driving period;
- the Floquet Hamiltonian needs to be calculable theoretically (with reasonable approximations).

Furthermore, Floquet theory finds its value in numerous other applications both in new and exotic subjects, such as phonon-driven spin-Floquet magneto-valleytronics [43], and in more widely-known technologies, like fibre optics [2].

These were only a few of the countless applications of Floquet theory. We are going to focus our work mainly on laser-matter interaction and on photoemission. In particular, up to now the Floquet formalism has been vastly used and tested with quasi-monochromatic light drivings, yet it is not clear if its concept can be extended to the short-pulse limit, where the light-dressed states could be employed to switch the optical properties of materials on ultrafast time scales. Indeed, due to their short duration few-cycle pulses lose their periodicity and border effects become rather relevant, and we may not be able to apply Floquet theory any longer. Hence, the objective of this thesis is to explore the limits of Floquet theory in the case of ultrashort pulses, therefore entering the realm of ultrafast physics and ultrafast optics.

0.3. Floquet theory in Ultrafast Optics

In order to deal with phenomena occurring at a very brief time scale we need to employ techniques which are able to probe sub-picosecond processes. Some of these processes include some chemical reactions [15], plasma processes [33], light-induced phase changes [54], and are even present in photosynthesis [51]. Photoemission is one of such phenomena, since the ionised electrons dynamics takes place on the lower side of the femtosecond (10^{-15} s) time scale.

Then, if we wish to treat these dynamics we have to use a tool possessing the same duration. The only physical object that we can utilise and that can reach such small durations are light pulses. Here *ultrafast optics* comes into play. With current technology we are able to generate light pulses with a duration that can reach down to hundreds of attoseconds (10^{-18} s) [45].

How are we able to create such short pulses? We can use two techniques: mode-locking and Q-switching[3]. According to Fourier theory, the broader the bandwidth we employ, and the higher the frequency used, the shorter the pulses we can generate. This reasoning reaches a physical limit when considering pulses in the order of a few femtoseconds for visible light (single optical cycle). If we wish to go beyond that limit we need to use higher frequency pulses, which cannot be generated like visible light due to the high absorption of the gain materials in that frequency range. Instead, we can use specific techniques such as High-

[3]All these concepts are discussed in detail in [46] and in [52].

order Harmonic Generation (HHG), which will be discussed more in detail in Chapter 1.1.1. On the other hand, a further requirement for these pulses is usually to have an intensity $I > 10^9 \frac{W}{cm^2}$. In order to reach that objective we can use multiple amplification stages, and employ techniques such as Chirped Pulse Amplification (CPA)[3]. Once these pulses have been produced, they can be used to perform the desired experiments.

Ours will be a series of *pump-probe* spectroscopy experiment on a Ne gas target using few-femtosecond pulses of variable duration (between 9 fs and 150 fs). The basic idea is to focus two different types of pulses onto a sample: one will be used to photoionise it, and the other to drive the actual dynamics. In our case the first one (*probe* pulse) will be in the *extreme ultraviolet* region (XUV), while the second one (*pump* pulse) will be in the *infrared* region (IR). In the following we will indicate with τ_{XUV} and τ_{IR} their respective duration. The probe will ionise the outer electrons of the gas, creating free electrons with an energy E_{MB}, while the pump is going to create *dressed states* with energy $E_{SB} = E_{MB} + N \cdot \Delta E$, with ΔE being the energy of a single IR photon and $N \in \mathbb{Z}$ the order of the sideband, with a result which is akin to that of Figure 1. Then, by varying the duration and intensity of the two sets of pulses, we will be able to finally explore the limits of Floquet theory. Specifically, we will first try to comprehend the behaviour of the theory for long IR pulses with different intensities, and then we shall investigate the effect of a finite driving pulse on the induced Floquet states. We will perform the experiments in the case of $\tau_{XUV}, \tau_{IR} >> T_{IR}$, with T_{IR} being the period of the IR pulse. In fact, by taking $\tau_{IR} >> T_{IR}$ we ensure not to have a streaking trace instead of sidebands [5], and if $\tau_{XUV} >> T_{IR}$ we will be able to apply the SVEA approximation, as performed in Chapter 2. Therefore, we will try to gauge how much greater our pulses need to be in relation to T_{IR} and see whether τ_{IR} needs to be larger than τ_{XUV} for us to apply Floquet theory, as in the original understanding of the theory.

0.4. Outline of the work

In this work we are going to examine the population of light-induced Floquet states through the use of few-femtosecond pulses. This study will be carried out bearing in mind the theoretical description given by Floquet theory, of which we wish to investigate the limits of validity both as a function of intensity and of pulses duration.

In this introduction we started to understand the basics of Floquet theory, and we saw a few applications in classical mechanics as well as in quantum mechanics, with an in-depth focus on optics. We also had a brief overview on ultrafast optics and on how the experiment is going to be performed.

In the first chapter we are going to conduct a detailed analysis on the methodology of the experiment. We will start from a general outlook on the experimental setup and on the instrumentation employed, to then have a better insight on the inner workings of each component of the arrangement. In particular we are going to study how the XUV pulse gets generated and the process of HHG, how the correct beam is selected after generation and how it is measured. We are also going to analyse the path of the pump IR pulse through the fibre and what happens when the two pulses meet. We are going to discuss the creation of the main band and the population of sidebands, and we are going to see the resulting spectrograms. Then the characterisation of the pulses in considered, as well as the instruments and techniques employed, such as FROG. In particular, we will describe the STRIPE algorithm utilised for the XUV phase reconstruction. The process of sideband characterisation and noise removal is also presented in detail.

The second chapter contains all the theoretical discussion on the topic of Floquet theory applied to our system. From the derivation of the Strong Field Approximation (SFA) to its simplification, and then passing through the Bessel expansion. Finally, we will see a few examples of the effects of both linear and non-linear dispersion on the pulses, which up to now have been considered either as monochromatic or as Gaussian.

In the third chapter we are going to discuss experimental results. At first we will analyse the long IR pulse regime and verify how the amplitude of the bands changes depending on the IR intensity; then, we shall study the case of different IR durations and non-Gaussian pulses, and how this affects the behaviour of experiment in relation to our model.

At last, the fourth and final chapter will be devoted to final comments and remarks, in which we will draw conclusions on the work and give future perspectives on the topic.

1 | Methodology

1.1. Experimental setup

Before explaining the raw theory behind the experiment, it is crucial to discuss the setup and the principles behind the experiment, so to have a better comprehension of their final objective. The experimental setup is illustrated in Figure 1.1.

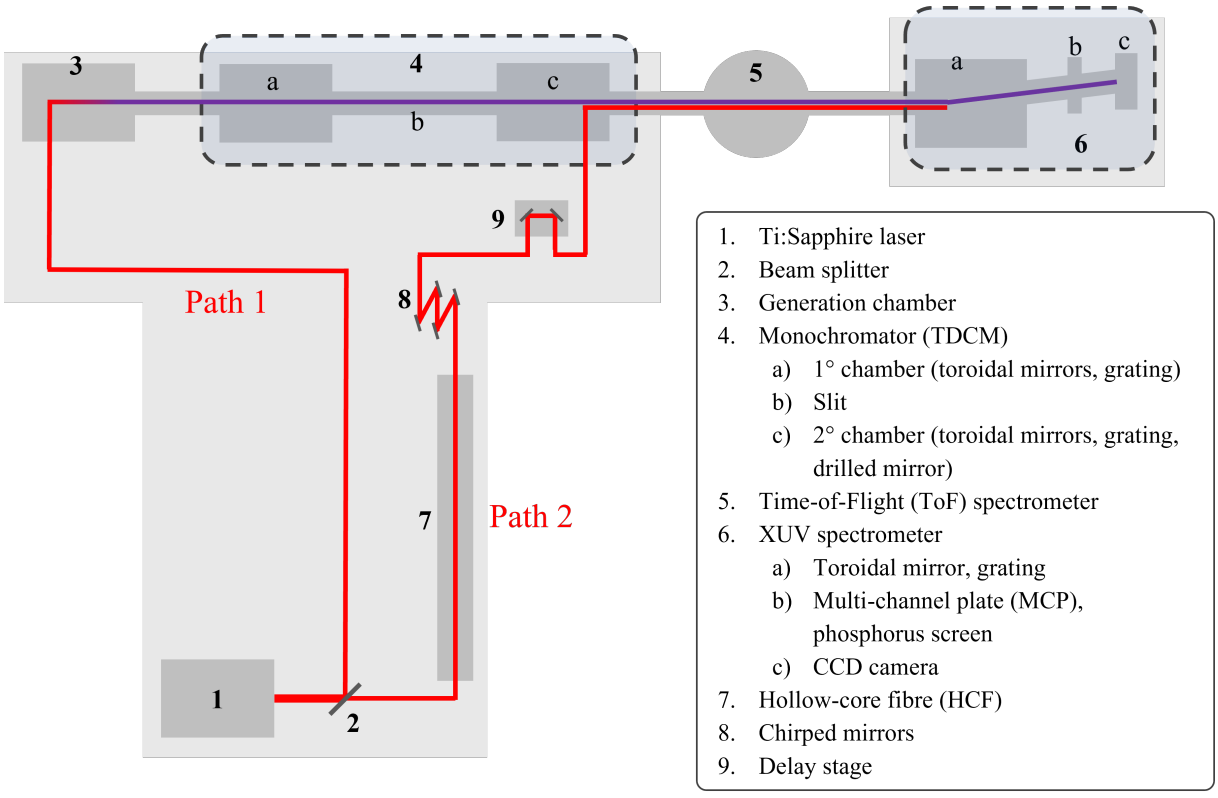

Figure 1.1: Simplified schematics of the optical setup and of the path travelled by the laser. In red, IR radiation ($\lambda_{IR} = 811$ nm); in purple, XUV radiation ($\lambda_{XUV} = 35.26$ nm).

The main light source that was employed consists of an ultrafast Ti:Sapphire laser operating in mode-locking regime used as a seed, with a wavelength of $\lambda_{IR} = 811$ nm (frequency: $\nu_{IR} = 370$ THz) and a repetition rate of $f_{rep} = 1$ kHz [8]. It is then amplified up to an

output energy of $E_{out} = 7$ mJ through a chirped-pulse amplification (CPA) stage [7], which employs high-power Q-switched laser as a pump [9].

At the laser exit, a beam splitter divides the beam into two paths. The first path ($P_{IR,1} = 1.2$ W) leads to the generation of the XUV pulse, which acts as the probe in the pump-probe experiment, while the second one ($P_{IR,2} = 1$ W) leads to a *hollow-core fibre (HCF)* compressione setup, which shapes the pulse in order to function as the pump.

Following the former, we encounter the generation chamber first, which allows to produce XUV pulses through *High-order Harmonic Generation (HHG)* [34]. Subsequently, the desired harmonic is selected through a *Time Delay-Compensated Monochromator (TDCM)* [39], and ultimately measured through an *XUV spectrometer* placed at the end of the setup, after traversing the *Time-of-Flight spectrometer (ToF)*.

If we follow the second path instead, the laser beam is collimated into the HCF, which modulates the duration and the shape of the pulses depending on the amount of gas it is filled with, and therefore on its pressure. Chirped mirrors at the output of the fibre enable chirp compensation.

Afterwards, a piezoelectric actuator is used in a delay stage to vary the temporal distance between the two paths, fundamental to obtain a complete spectrogram of our pump-probe experiment. The laser is finally deflected into the second chamber of the monochromator, where it recombines with the first path.

The two pulsed laser beams co-propagate inside the ToF spectrometer, where they are focused onto our sample, a cloud of Ne gas, thus performing the experiment.

1.1.1. XUV generation

In order to perform our pump-probe experiment with Ne gas it is required to have a highly energetic pulse to ionise the electrons. IR radiation is not capable of such a task due to its low photon energy ($E_{IR} = 1.53$ eV, while $E_{ion.,Ne} = 21.56$ eV)[1], whereas XUV radiation already has an energy of $E_{XUV} = 35.23$ eV $> E_{ion.,Ne}$. Therefore, we need to generate said XUV pulse. To do so, we deflect the beam inside the vacuum chamber of Figure 1.2, kept at a pressure of $p \sim 10^{-9}$ bar. This is to prevent air from absorbing all the XUV radiation. Then, aided by a converging mirror we focus the beam into an HHG cell. The HHG cell is a metal cell filled with Ar in gaseous form, which is kept confined by aluminium tape. Once the beam is focused onto the cell, it burns the aluminium and gets in contact with the gas, thus generating high order harmonics in the XUV range.

[1] We would need a 14-or-higher photon absorption process, requiring a very high IR intensity.

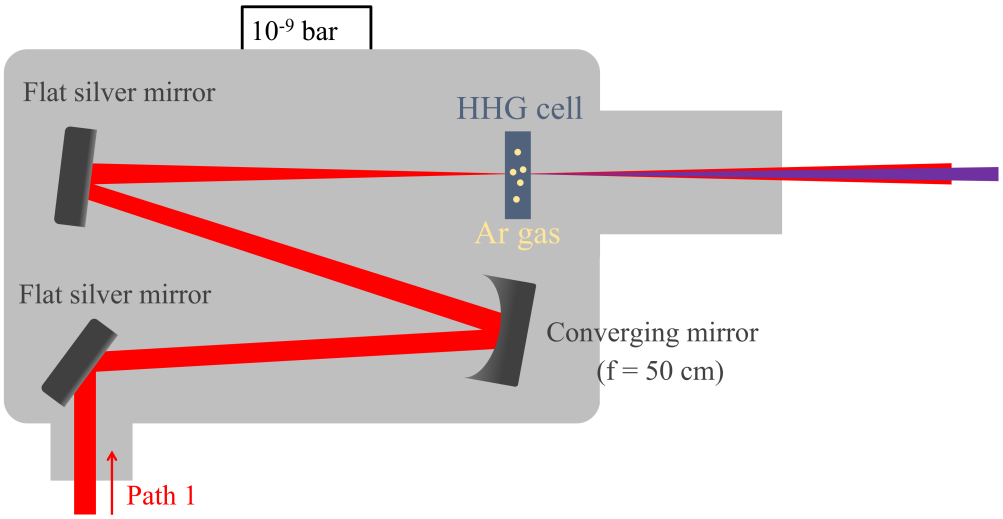

Figure 1.2: Generation chamber schematic.

To understand what happens from a physical point of view, we can use the *three-step model*[2] [52]. As the name implies, we can subdivide the phenomenon into three stages, as shown in Figure 1.3:

1. **Ionisation:** the Coulomb potential experienced by the electrons of each Ar atom is strongly distorted by the presence of the so-called *driving pulse* (our IR pulse), resulting in the generation of a potential barrier which may be overcome through tunnel ionisation by the outer-most electrons.

2. **Acceleration:** the ionised electron is accelerated far from the nucleus at first, following the path of least resistance (i.e. the direction in which the potential is the lowest); however, the driving pulse keeps varying the shape of the potential well in an oscillating pattern, and the free electron is soon led back towards the parent ion.

3. **Recombination:** the free electron collides with the ion, thus recombining; its kinetic energy is then released in the form of a high-energy XUV photon, which constitutes the high-order odd harmonics of the initial IR pulse ($E_{XUV} = [2k+1] \cdot E_{IR}$); it is worth noting that this recollision happens with an efficiency of $10^{-8} \div 10^{-6}$.

[2]We will not delve into mathematical detail, which is outside the scope of this thesis.

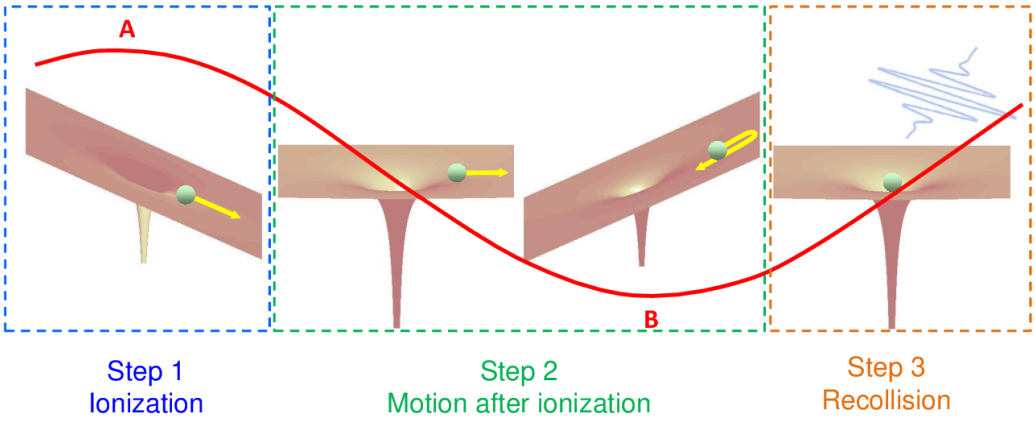

Figure 1.3: Three-step model representation. Figure from [36].

1.1.2. Time-Delay Compensated Monochromator (TDCM)

After exiting the first vacuum chamber, two kinds of pulse are present: the generating IR pulse and the XUV pulse. Since we only need the higher energy one, we will consider just the XUV line. We could eliminate the IR radiation by intercepting it with an Al filter upon entering the second vacuum chamber (which is kept at around 10^{-10} bar for reasons akin to the first one), but this would decrease the overall fluence of a factor 10.

Furthermore, the XUV pulses would remain composed of several high-order harmonics, i.e. they would not be monochromatic. In order to revise our pump-probe experiment, we need to separate them and select one, and we do so by means of a **Time-Delay Compensated Monochromator (TDCM)**. The TDCM is composed of two identical structures separated by a slit. Each structure comprises two *gold-plated toroidal mirrors* and a *grating*. The first toroidal mirror is used to collimate the beam, the grating spectrally disperses the radiation, while the second toroidal mirror focuses the beam. The beam is focused in correspondence of the slit, which blocks all the harmonics but one, which is the one we wish to study (in our case it will be H23, i.e. the 23^{rd} harmonic). The pulses that are let through are then compensated both temporally (*broadening compensation*) and spatially (*spectral dispersion compensation*) by the second structure, which is placed inside the third vacuum chamber (10^{-8} bar).

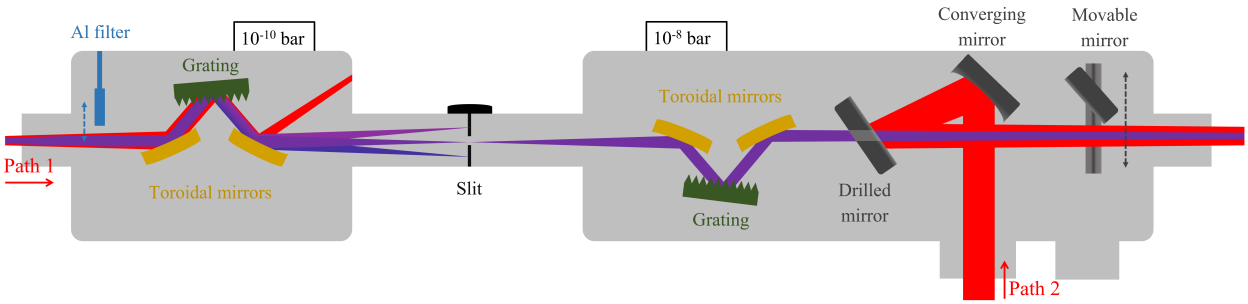

(a) Order (1,1) - one harmonic is selected for the experiment.

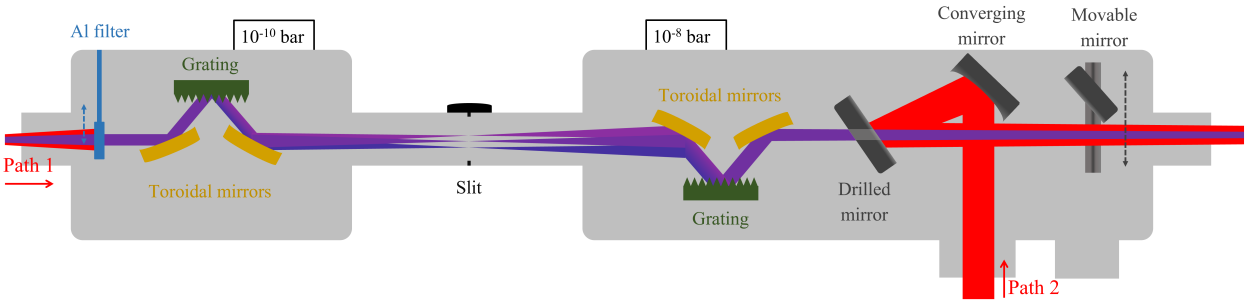

(b) Order (0,0) - several harmonics passing for calibration purposes.

Figure 1.4: Second and third vacuum chamber. The second chamber contains the Al filter, two toroidal mirrors and a grating. Between the two chambers, a slit. The third chamber accommodates two toroidal mirrors and a grating for the XUV line, and a converging mirror and a drilled mirror for the IR line. The drilled mirror lets the XUV from the first path through while reflecting most of the IR from the second path. A movable mirror may be inserted to deflect the IR pulses and make power, spectrum or beam profile measurements (see Chapter 1.3).

Taking a closer look at how the gratings operate, we observe that they diffract light depending on its wavelength and on the angle at which it impinges onto the grooves. In fact, given an incident angle α, a generic diffracted angle θ, and a distance between grooves d, we have

$$\sin\theta = \sin\alpha + \frac{m \cdot \lambda}{d} \ ,$$

where m is the *order of diffraction*. As we can see both from the previous formula and from Figure 1.5, if $m = 0$ we have no dependence from the wavelength, hence the grating acts as a mirror. If, on the other hand, we are at order $m = 1$ or higher, the sine of the diffracted angle is linearly dependent on λ, and a splitting of all the present colours is

manifested.

Therefore, if we allow the grating to rotate, we are able to precisely select the frequency we desire to work with, obstructing all the others with the slit. In our setup both gratings are able to rotate, and to run the experiments we wish to operate at order (1,1), meaning that both gratings need to be at order 1. We will use order (0,0) with an open slit for calibration instead, as described in Chapter 1.3.2.

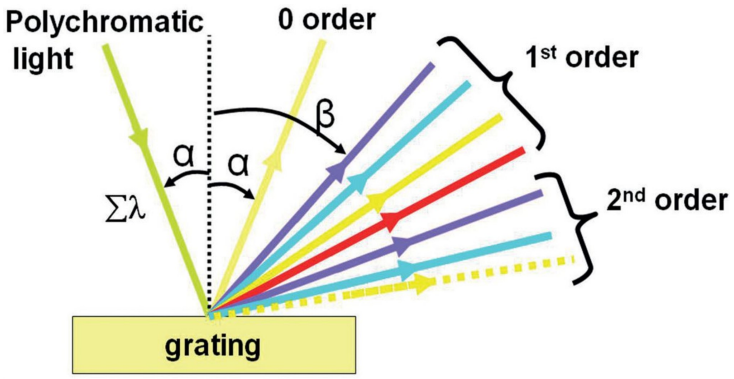

Figure 1.5: A diffraction grating. While order 0 still contains all frequencies, orders 1 and 2 spatially spread the spectrum of the beam.

1.1.3. XUV spectrometer

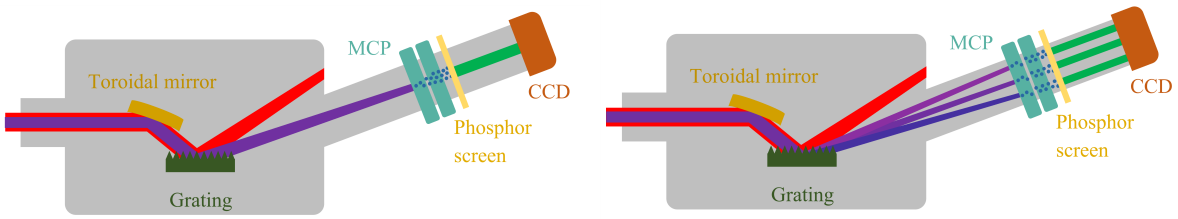

(a) (b)

Figure 1.6: XUV spectrometer in the case of monochromatic light (1.6a) - i.e. order (1,1) of the monochromator - and in the case of superimposed harmonics (1.6b) - i.e. order (0,0).

After recombining with the IR pulse (path 2) in the second TDCM chamber and entering the Time-of-Flight spectrometer (which we will discuss in detail in Chapter 1.1.5), the XUV radiation (path 1) travels further, to finally be detected by the **XUV spectrometer**.

The XUV spectrometer is made up mainly of five elements: another *gold-plated toroidal mirror*, followed by a *grating*, a *micro channel plate (MCP)*, a *phosphor screen*, and at last a *CCD camera*.

The first two elements act exactly as mentioned in the previous section: if we are at order (1,1) with a closed slit, it simply reflects the beam with a wavelength-dependent angle (Figure 1.6a); if we are at order (0,0) and the slit is open, it parts the frequencies which were collimated again by the second grating in the TDCM (Figure 1.6b).

After the grating, the pulses hit the micro channel plate (MCP) in *Chevron configuration* (see Figure 1.7). Photons from the XUV pulses hit the micro channels, ionising the metal and generating electrons. These charges travel along the channels striking their walls and producing more and more electrons. This cascade of electrons then collides with the phosphor screen, which in turn converts electrons into photons. Naturally, the more the photons reaching the MCP, the more the electrons ending up on the screen, and the more the photons generated moving towards the CCD camera, which finally observes the shape and intensity of the pulse.

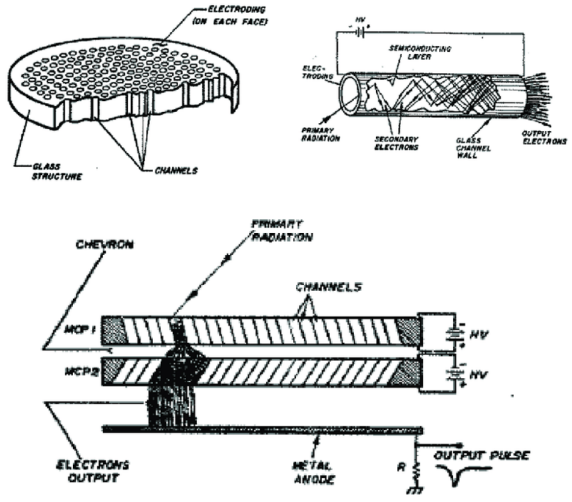

Figure 1.7: Micro channel plate scheme. Top left: section of single MCP. Top right: single channel of MCP and electron chain ionisation. Bottom: MCP in Chevron configuration. Adapted from [25].

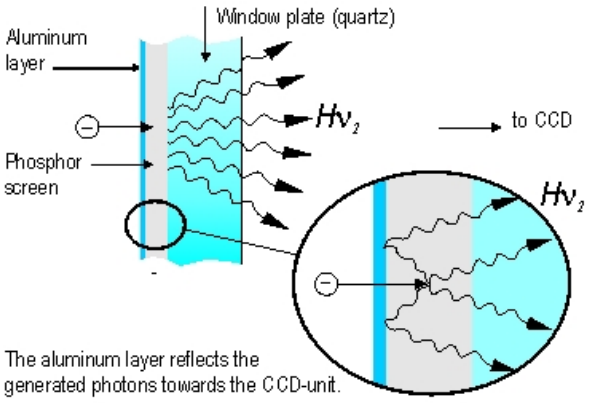

Figure 1.8: Phosphor screen. Converts accelerated electrons into photons. From [44].

The following images represent what can be observed at CCD output in the (0,0) order case with an open slit, and in the (1,1) order case with a closed slit.

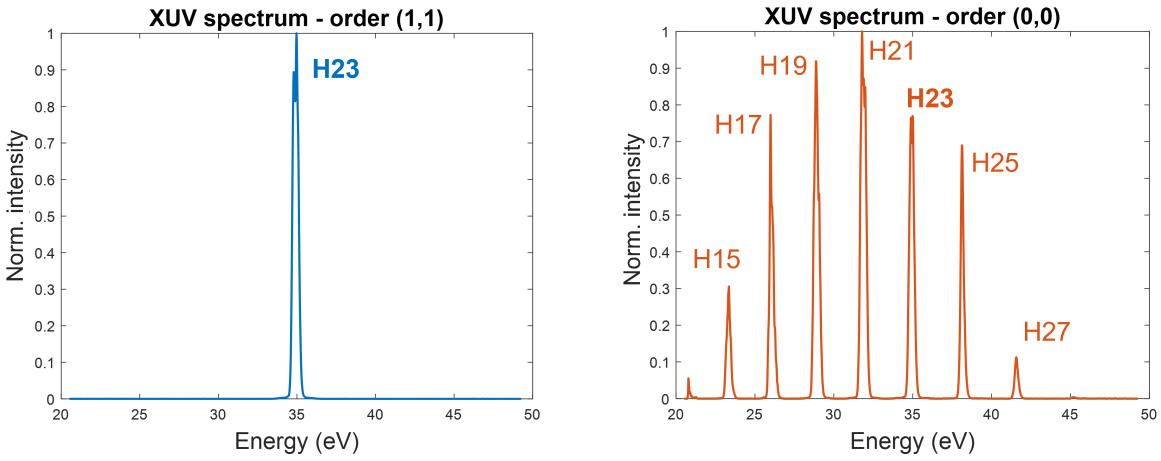

(a) (b)

Figure 1.9: XUV spectrum in the case of (1,1) order with a closed slit (1.9a), and in case of (0,0) monochromator order with an open slit (1.9b).

1.1.4. Hollow-core fibre (HCF)

Now that the XUV path is clear, we will examine the IR line, starting from the role of the **hollow-core fibre (HCF)**.

The HCF is an optical fibre composed of a glass cladding ($n \simeq 1.5$) and an empty core guiding the IR pulses. Having a hollow core is fundamental, as it can be filled with Ne gas to modulate the refractive index n seen by the pulse ($n_{gas} = 1 \div 1.00011896326$[3]), and therefore to alter the pulse shape. The more gas we input into the fibre, the higher the refractive index is.

As a result, we are able to use *self-phase modulation (SPM)* and *self focusing* to vary the spectral and spatial profile of the pulse. In fact, according to *Kerr effect* the resulting refractive index is:

$$n(z,t) = n_0 + n_2 \cdot I(z,t) \ ,$$

with n_0 and n_2 distinct for each material and I the intensity, dependent on z and t, the propagation direction and time respectively. From a spatial point of view this means that, together with the coupling of laser and fibre, we are able to get a high-intensity mode which is very close to Gaussian. From a temporal point of view, SPM modifies the phase ϕ of the pulse, together with its spectrum ω, and we have both *spectral broadening*, and

[3]Calculated through [42] at $p = 1.8$ bars.

a *positive frequency chirp*:

$$\omega(t) = \frac{\mathrm{d}\phi}{\mathrm{d}t} = \omega_0 - \frac{\omega_0 n_2 z}{c}\frac{\mathrm{d}I}{\mathrm{d}t} \ ,$$

where

$$\phi(t,z) = \omega_0 t - kz = \omega_0 t - \frac{\omega_0}{c}\Big(n_0 + n_2 I(t,z)\Big)z$$

and where c represents the speed of light in vacuum, and ω_0 is the laser central frequency. While the first phenomenon implies the generation of new frequencies, never possessed before by the pulse, the second one suggests that some frequencies tend to arrive at later times than others. In particular, in case of a positive chirp lower frequencies arrive earlier than higher frequencies. Now, according to Fourier theory having a broader spectrum implies the possibility of a pulse that is shorter in time, and this is in fact achieved through a series of chirped mirrors[4] at fibre output, which compensate the positive chirp. Hence, by regulating the pressure of the gas inside the fibre we are capable of generating pulses with a duration calculated at full width at half maximum (FWHM) which ranges from 50 fs (empty fibre) down to 9 fs (1.8 bars).

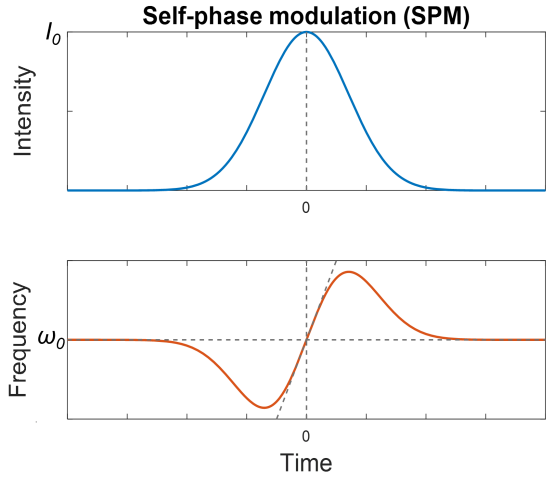

Figure 1.10: Self-phase modulation graph. In blue, the pulse intensity. In orange, the spectrum of the pulse. As we can see, different frequencies arrive at different times.

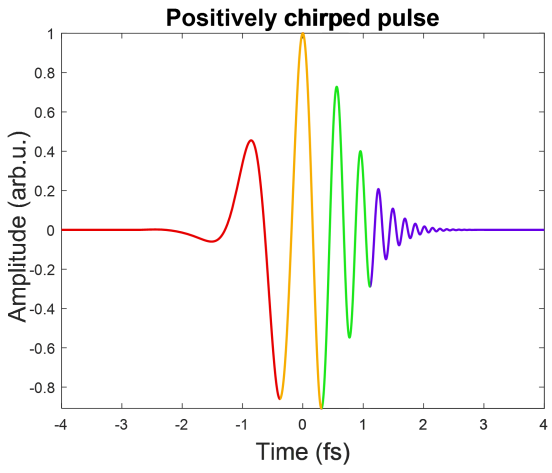

Figure 1.11: Example of positively chirped pulse. Higher frequencies arrive at later times with respect to lower ones.

[4]Chirped mirrors are a particular type of dielectric mirrors with variable layer size which delay lower-energy, "faster" frequencies, so to reunite them temporally with the higher-energy, "slower" ones (see Figure **??**).

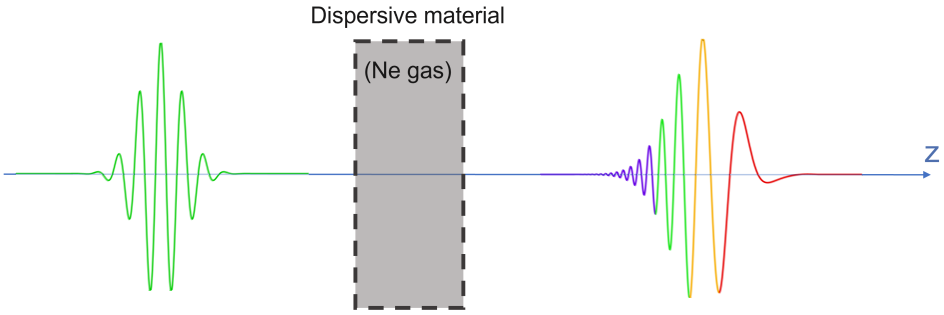

Figure 1.12: Generation of a positively chirped pulse from a Gaussian one.

1.1.5. Time-of-Flight spectrometer (ToF)

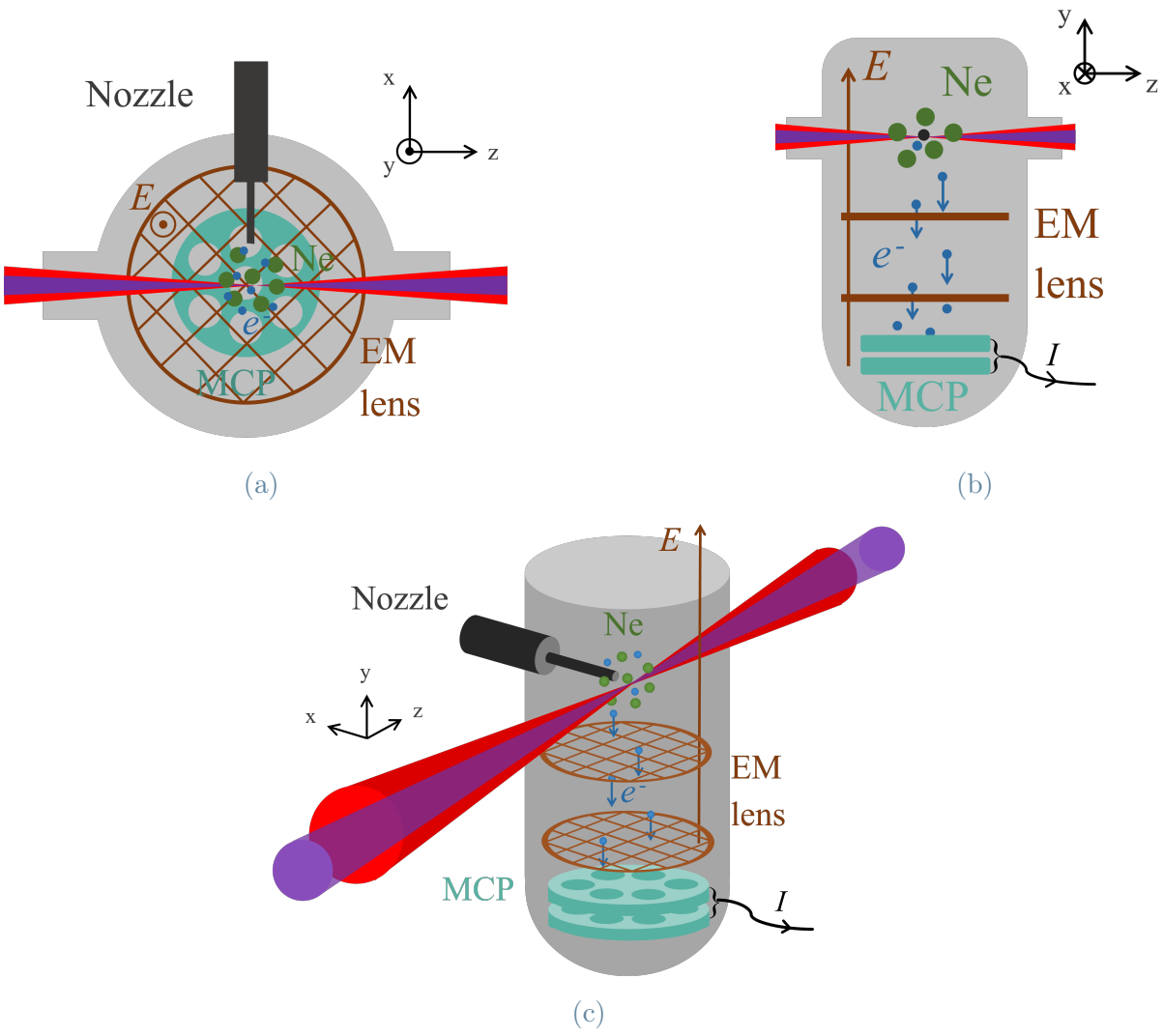

Figure 1.13: Time-of-Flight spectrometer (ToF) seen from the top (1.13a), from the side (1.13b), and a 3D representation (1.13c).

In this penultimate section we finally see what happens inside the **Time-of-Flight spectrometer (ToF)**.

Both XUV (path 1) and IR (path 2) pulse meet inside the second TDCM chamber (see Figure 1.1.2). On one hand, the XUV pulse arrives from the gratings of the TDCM itself and passes through a drilled mirror; on the other, the IR radiation enters the vacuum chamber from the side and strikes a converging mirror, which deflects the beam onto the drilled mirror. Even if part of the pulse is discarded (namely its peak) diminishing its intensity, the majority of photons is reflected inside the ToF.

Both beams are then focused near the tip of a needle (or nozzle) inside the ToF, from which *Ne gas* (our sample) is ejected. The light ionises the gas (more details in Chapter 1.2), yielding free electrons that are accelerated by means of an electric field generated through electromagnetic lenses. The charges travel towards an MCP in Chevron configuration (Figure 1.7) at the bottom of the ToF, and generate a current that is proportional to the quantity of electrons that hit said MCP, and resolved in the time they take to travel from gas cloud to plate (i.e.: *time of flight*). The signal is displayed onto the computer screen immediately afterwards.

Subsequently, the XUV line continues along its path to be detected by the XUV spectrometer, whereas the IR is deflected away by the last grating in the following vacuum chamber.

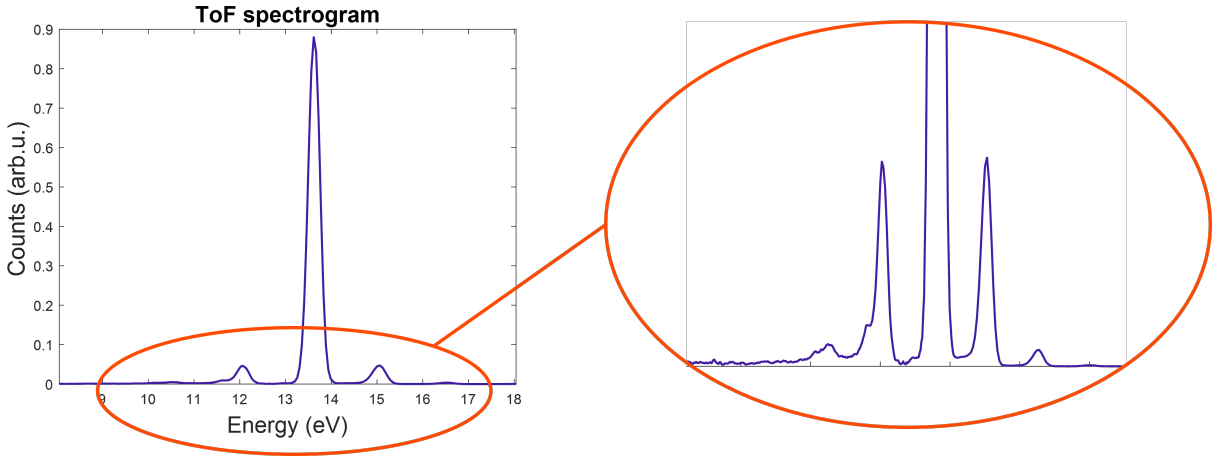

Figure 1.14: Example of experimental ToF spectrogram for a given delay between the pulses. A more detailed analysis of this spectrogram will be conducted in Chapter 1.3.5.

1.2. Pump-probe experiment

Now we are going to briefly illustrate the concept behind the kind of experiment performed. Before reaching the ToF spectrometer, the TDCM is used to select the 23^{rd} harmonic of the IR beam ($E_{XUV} = 35.23$ eV, or $\lambda_{XUV} = 35.26$ nm). This beam is used to ionise the gas inside the ToF and generate photoelectrons with an energy of $E_{MB} = E_{XUV} - E_{ion.,Ne} = 13.67$ eV, which we will call *main band*, MB; if an opportunely delayed IR pulse ($E_{IR} = 1.53$ eV, or $\lambda_{XUV} = 811$ nm) is added to the process, its field dresses the photoelectron final state inducing the formation of sideband peaks in the photoelectron spectrum. Those shall be indicated as $\mathrm{SB}^{N\pm}$, with $E_{SB^{N\pm}} = E_{MB} \pm N \cdot E_{IR} = 13.67 \pm N \cdot 1.53$ eV, and with $N \in \mathbb{N}$ being the number of photons absorbed (+) or emitted (-), following the scheme of Figure 1.15. As we will see, the number of generated sidebands depends on the IR laser intensity. Naturally, the more IR photons impinge onto the ionised electrons, the more sidebands are visible, having a higher intensity. Furthermore, the main band becomes more depleted, accordingly to particle conservation. Actually, if we keep increasing the IR intensity with respect to the XUV one, we will reach a point in which the sidebands will start to empty too in order to fill higher order ones. More details about these phenomena are given in Chapter 2.

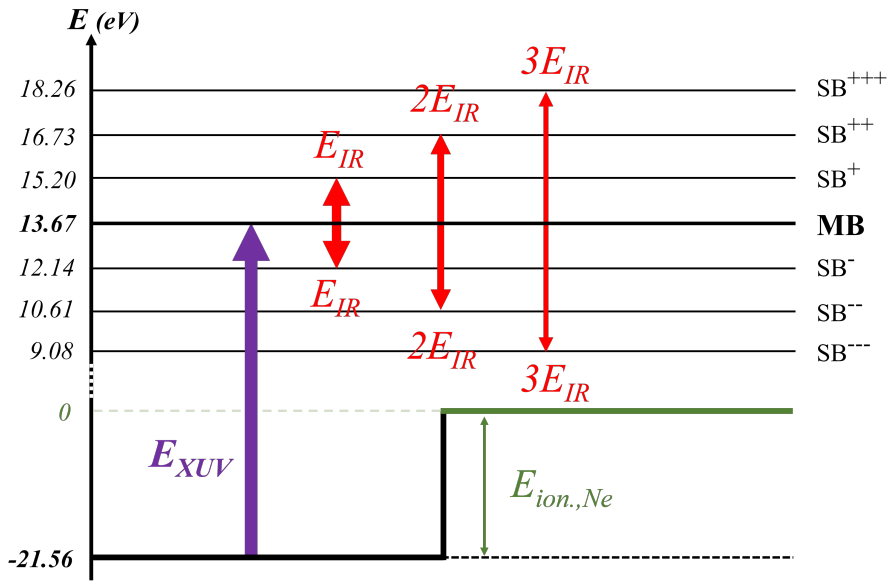

Figure 1.15: Visual representation of the ionisation of photoelectrons and formation of main band (MB) and sidebands (SB).

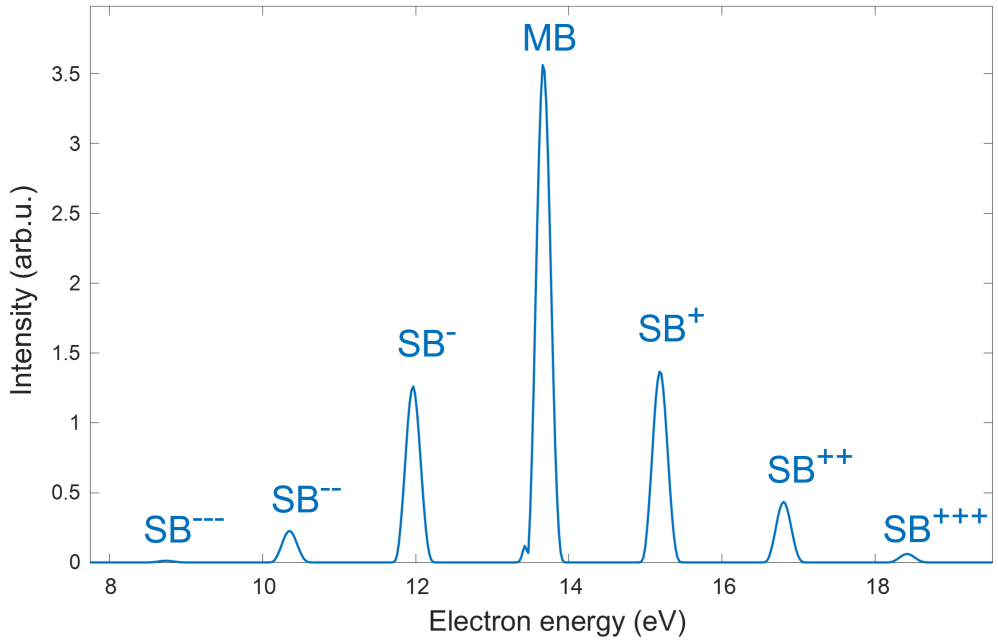

Figure 1.16: Simulated intensity of the sidebands as a function of the energy of ionised photoelectrons at null delay.

In order for this to happen, it is crucial to overlap the pulses both spatially and temporally, due to the rapidity of electron dynamics. This is why the two paths of the XUV and IR beams must have the same length. Furthermore, to follow the complete dynamics of photoelectrons, probing needs to happen at different delays with respect to pump excitation[5]. This is what the delay stage is for. It is composed of a pair of mirrors mounted onto a moving sled at 90° one with respect to the other; the sled is in turn connected to an electronically controlled piezoelectric actuator that expands or shrinks depending on the current it receives, consequently moving the mirrors and varying the time delay.

[5]Think of it as a film: to have a "moving image", you need to have a sequence of frames, of snapshots taken at different times. By probing the phenomenon at different delays from the event of the pump, you are effectively taking many pictures which allow a reconstruction of photoelectronic behaviour during and after ionisation.

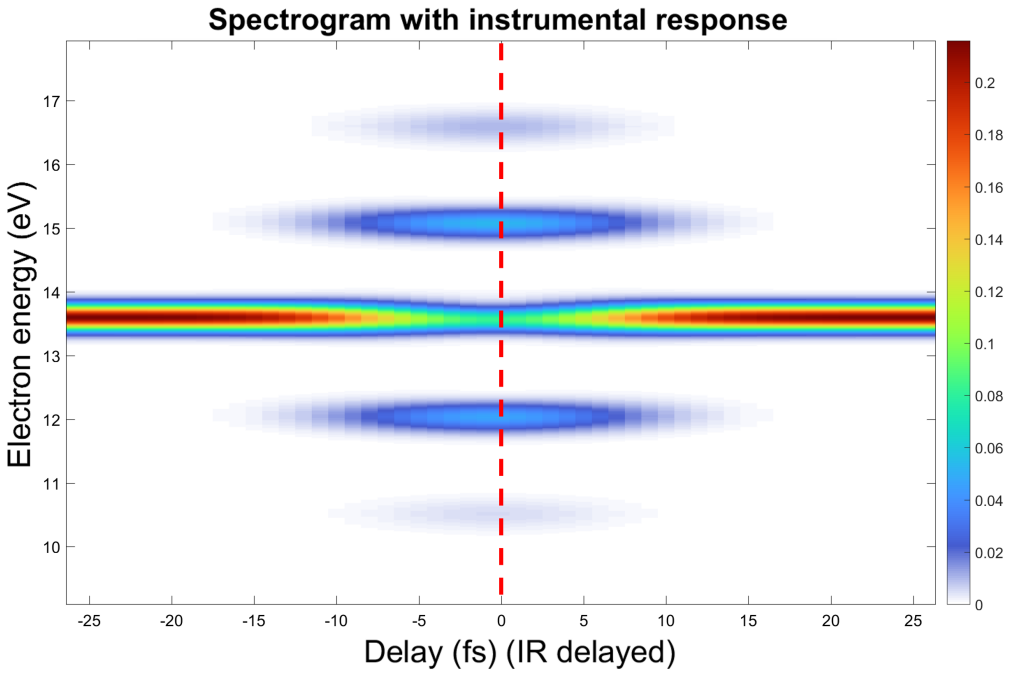

Figure 1.17: Example of SHS simulation. In this 3D graph it is possible to notice 2 sidebands on each side of the main band. These are SB^{+} and SB^{++} on the upper end, and SB^{-} and SB^{--} on the lower part of the plot. It is also clear that the main band is weaker in correspondence of the peak of the sidebands. The 2D graph at null delay (dashed line) corresponds to Figure 1.16.

By doing as such, we are able to plot a colourmap of the intensity of the sidebands and of the main band as a function of the energy of the photoelectrons and of the delay between IR and XUV pulses. We are therefore plotting a so-called *single-harmonic spectrogram (SHS)*. In Figure 1.17 we can observe a simulation of an SHS. The shape that sidebands can assume may vary, and it is usually far from the smooth and regular shape of Figure 1.17, the principal reason being that the pulses we used in the previous simulation possess a Gaussian temporal distribution, while in reality our pulses have a more complex structure. This depends on a series of factors which will be explored in detail in Chapter 2.3, and cannot be attributed solely to experimental noise, whose influence on the matter may be disregarded. For the moment we will limit to show a few examples of real traces (Figures 1.18 and 1.19).

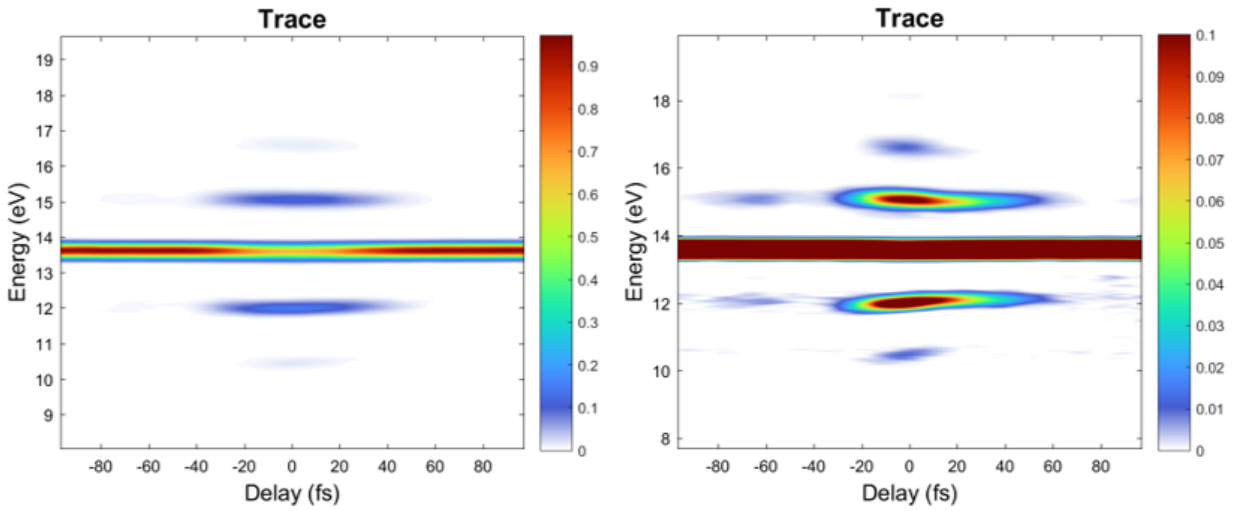

(a) (b)

Figure 1.18: Some examples of experimental SHS plots. In Figure 1.18a, two sidebands are visible on each side of the main band, and the depletion of the main band is also evident. In Figure 1.18b, another spectrogram has been over-saturated to better display the shape of the sidebands, which are clearly centred around the expected energies, yet do not possess an elliptical shape.

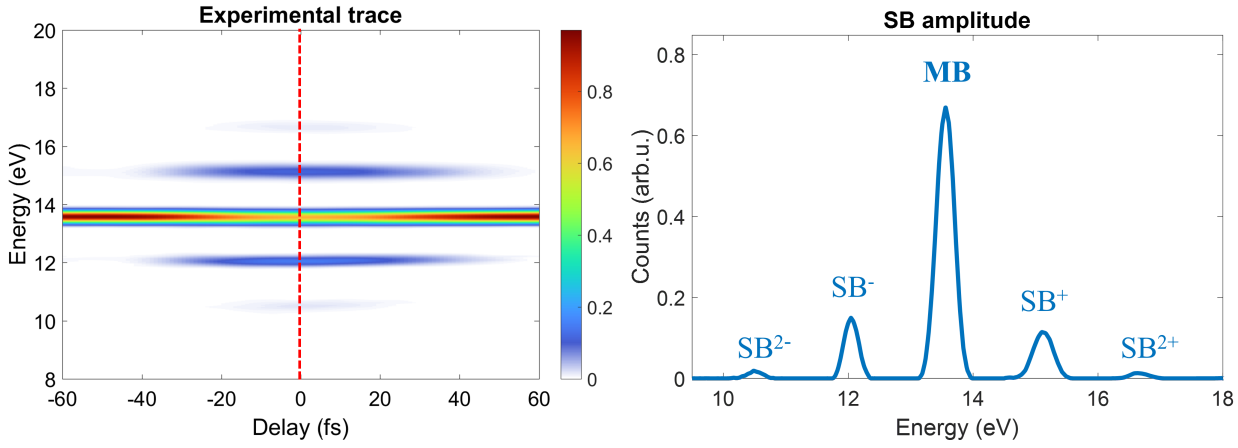

(a) (b)

Figure 1.19: (a) Example of experimental spectrogram as a function of energy and time delay τ. (b) SB amplitudes as a function of energy at $\tau = 0$ fs and $I_{IR} = 6.58 \cdot 10^{11} \frac{W}{cm^2}$.

1.3. Beam characterisation

In this section we will study the techniques employed to measure and calculate the pulse intensity and temporal characteristics. We will also have a glimpse of the results of our beam characterisation, so to have an idea of the type of pulses employed in our experiment. Later on, this will help us have further insight on the effects of non-idealities and on the reasons behind given outcomes. We will also see how to correctly characterise the experimental spectrograms we retrieved.

1.3.1. Intensity measurement

A fundamental part of beam characterisation is knowing the intensity of the pulses we use in our experiments. Intensity cannot be measured directly, we require two quantities to calculate it: the **beam profile**, and the **power** of the beam.

The spatial distribution of the pulse can be measured by means of a **beam profiler**, which detects the distribution of photons inside the beam. It allows to have an idea of the spatial FWHM of the pulse and to check whether the mode is Gaussian or it has any kind of non-ideality, astigmatism being the most frequent. Hence, it is a way to determine the beam quality and of calculating its M^2 factor[6]. In our configuration the laser from the second TDCM chamber gets deviated by the movable mirror towards the device. In the same position we employ a **power meter** to measure the average power of the beam. Knowing both power and beam profile, we can now calculate the intensity of our IR pulses.

[6]For further details about M^2 see [52].

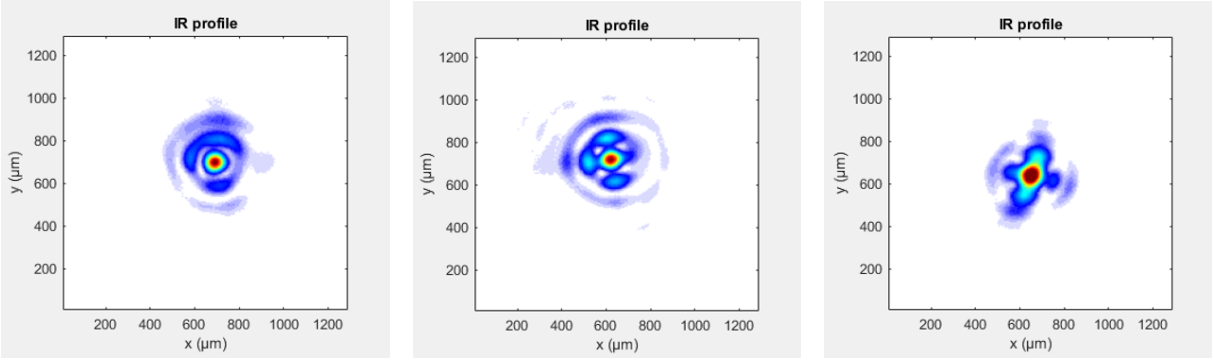

(a) (b) (c)

Figure 1.20: Three examples of IR beam profile. While the first one from the left can be interpreted as a quasi-Gaussian beam, the second one is less so. The last one is undoubtedly aberrated, and in particular it manifests an evident astigmatism, which elongates the beam in one direction and compresses it along its orthogonal.

1.3.2. Spectral characterisation

In order to characterise our ultrashort pulses we can start by using a **spectrometer**, which will measure the spectrum of our pulses[7]. In a spectrometer, light will enter the device and travel towards a first focusing mirror. This mirror will send the beam to a diffraction grating, which will disperse the different wavelengths of the light source. We now have the spectrum of the beam. Subsequently, the different frequencies move in the direction of a second focusing mirror, that will focus each part of the beam onto a stripe of pixels, each dedicated to a wavelength, acting as the detector.

Seeing as now we have the intensity of every wavelength shining onto each pixel, in order to have a physically meaningful signal we convert the units of the x axis of the detector from pixels (px) into energy (eV). Therefore, we need to **calibrate** our axis. To do this we are going to require the gratings at order (0,0). This way we will be able to see all the harmonics and their intensity (Figure 1.21a). Then, we are going to integrate along the y axis (Figure 1.21c), apply a multi-Gaussian fit, and find the peak position in pixels for each high harmonic. We will be able to associate to each pixel a value in energy (Figure 1.21b), and finally plot the harmonics as a function of the energy instead of the pixels (Figure 1.21d).

[7]For the XUV pulse, the spectrometer is the one presented in Chapter 1.1.3. For the IR beam, a movable mirror is present inside the third vacuum chamber (right side of Figure 1.4) which will deviate the path of the IR laser towards the spectrometer when inserted.

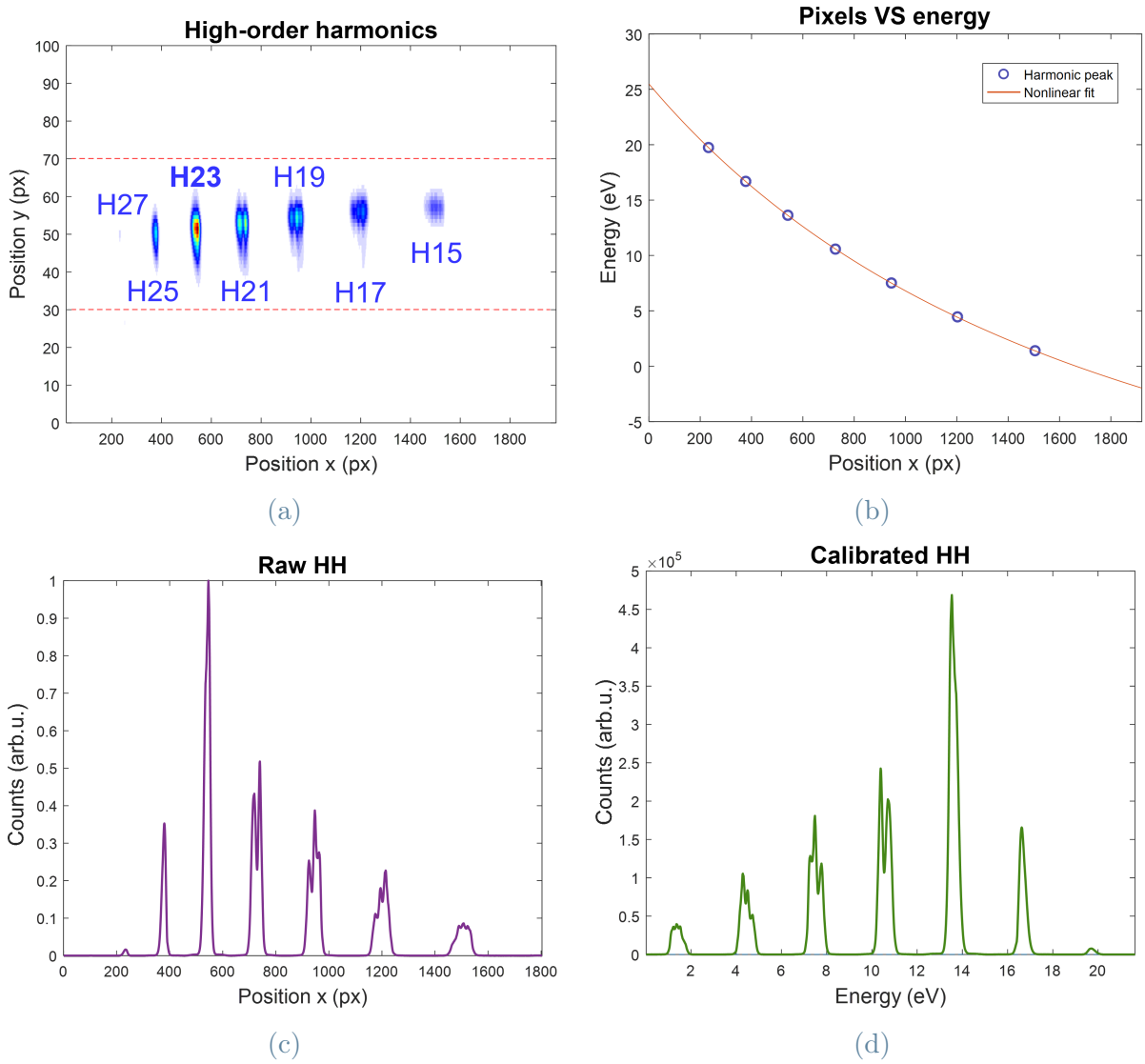

Figure 1.21: In Figure 1.21a, the output of our spectrometer, in which many high-order harmonics are visible. Integrating along the y-axis the previous signal we obtain Figure 1.21c. Figure 1.21b represents the axis conversion from pixels to energy, which allows to obtain the final result of Figure 1.21d, in which the signal is plotted as a function of energy, and as a consequence all the harmonics result equidistant.

Now that we have the spectrum, we can use Fourier theory to Fourier transform what we obtained in the frequency domain into the time domain. The narrower the spectrum, the larger the pulse in time, and vice versa. Hence, we are able to retrieve a duration for the pulses by calculating the FWHM of the Fourier transform of the spectrum.

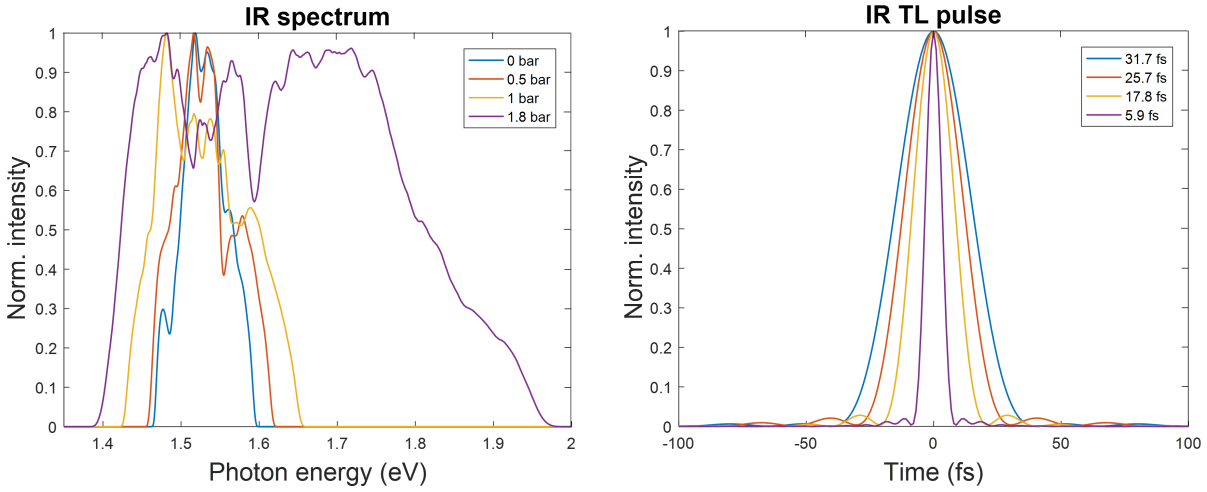

(a) (b)

Figure 1.22: Four examples of different IR spectra (1.22a) and their associated pulse duration (1.22b). A broader spectrum corresponds to a narrower duration of the transform limited pulse.

There is only one issue: we are not able to retrieve the *phase* of these pulses. In fact, it is not possible to fully reconstruct the pulse only by means of a spectrometer, and what we calculate is the TL (transform limited) duration, that is the minimum duration it is possible to achieve. Hence, we need to follow another approach: we will use the so-called FROG technique.

1.3.3. FROG reconstruction

Frequency-Resolved Optical Gating, otherwise known as **FROG**, is one of the main techniques to gather information about ultrashort pulses[8]. It is a spectrographic technique capable of retrieving the shape, duration and, above all, *phase* of a pulse. It is in fact impossible, due to the sheer rapidity and briefness of the pulse itself, to use exclusively electronic devices to characterise the beam. We could say that *electronics is too slow*, and the relaxation of electrons in a common detector cannot follow the dynamics of light.

There are several types of FROG, including self-diffraction FROG (SD-FROG), polarization-gated FROG (PG-FROG), cross-correlation FROG (XFROG), or transient-grating FROG (TG-FROG) [17, 48]. What we are going to use is *second-harmonic generation FROG*, or *SHG-FROG*.

[8]In the context of our setup, this method is exploited in order to characterise the IR pulses, and is realised "ex-situ". For this reason it is important to ensure that the pulses led to the FROG experience the same dispersion encountered on the path towards the sample.

How does SHG-FROG work? Since our objective is reconstructing the electric field $E(t)$ of the pulse, we wish to recover the temporal distribution of its frequencies. In order to capture this temporal distribution of frequencies, we can define a *gate function* $g(t-\tau)$, which will sample the electric field with a delay τ varying with respect to our pulse. The resulting signal from the presence of both pulse and gate will be $E_{sig}(t,\tau) = E(t)g(t-\tau)$. This gated signal in the Fourier domain appears as:

$$\tilde{E}_{sig}(\omega,\tau) = \mathcal{F}[E_{sig}(t,\tau)] = \int_{-\infty}^{+\infty} E(t)g(t-\tau)e^{-i\omega t}dt$$

Therefore, if we are able to acquire a spectrogram of this signal, we will find:

$$S(\omega,\tau) \propto \left|\tilde{E}_{sig}(\omega,\tau)\right|^2 = \left|\int_{-\infty}^{+\infty} E(t)g(t-\tau)e^{-i\omega t}dt\right|^2$$

Now, being FROG a *self-referenced technique*, it only makes use of one beam, which will act both as the pulse to investigate ($E(t)$) and as our gate function ($E(t-\tau)$). Hence, the final spectrogram obtained is going to be

$$S(\omega,\tau) \propto \left|\int_{-\infty}^{+\infty} E(t)E(t-\tau)e^{-i\omega t}dt\right|^2$$

From this, we will be able to calculate $E(t)$ through an iterative algorithm (shown later on).

The way in which the spectrogram is performed is shown in Figure 1.23. The pulses are sent onto a 50:50 beam splitter, which separates them into two paths. One path heads straight in the direction of a second 50:50 beam splitter, whereas the other one leads to a delay line regulating the difference in the time of arrival of the two beams, to then go towards the beam splitter. The second beam splitter guides the two beams onto a converging mirror, which in turn focuses them onto a $\chi^{(2)}$ crystal (BBO, i.e. β-barium borate - BaB_2O_4), allowing for second-harmonic generation. At last, these new pulses doubled in frequency are picked and sent through another focusing lens to a spectrometer to be analysed, thus giving origin to the sought spectrogram.

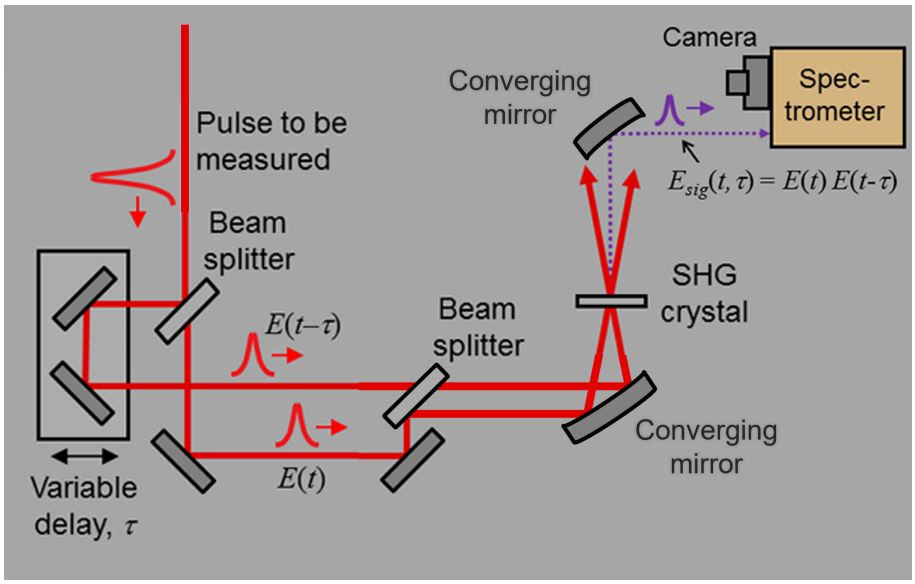

Figure 1.23: SHG-FROG scheme. Adapted from [47].

The following is the iterative algorithm used to retrieve $E(t)$ from $S(\omega,\tau)$:

- start with a guess of the initial electric field $E(t)$. Usually, a null phase ($\phi = 0$) is assumed and the transform limited (TL) pulse is used;
- multiply $E(t)$ by the gating function $E(t-\tau)$, to get $E_{sig}(t,\tau) = E(t)E(t-\tau)$;
- find $\tilde{E}_{sig}(\omega,\tau) = \mathcal{F}[E_{sig}(t,\tau)]$;
- calculate a new quantity, $\tilde{E'}_{sig}(\omega,\tau) = \frac{\tilde{E}_{sig}(\omega,\tau)}{|\tilde{E}_{sig}(\omega,\tau)|}\sqrt{S(\omega,\tau)}$. This way the phase is still unknown, but we substitute the correct modulus inside the formula.
- antitransform the new quantity, to obtain $E'_{sig}(t,\tau) = \mathcal{F}^{-1}[\tilde{E'}_{sig}(\omega,\tau)]$;
- integrate $E'_{sig}(t,\tau)$ in $d\tau$, so to have $\int_{-\infty}^{+\infty} E'_{sig}(t,\tau)d\tau = \int_{-\infty}^{+\infty} E'(t)E(t-\tau)d\tau$;
- since $E'(t)$ does not depend on τ, we can take it out of the integral and calculate it by knowing $E'_{sig}(t,\tau)$ and $E(t-\tau)$, and we do it as $E'(t) = \frac{\int_{-\infty}^{+\infty} E'_{sig}(t,\tau)d\tau}{\int_{-\infty}^{+\infty} E(t-\tau)d\tau}$;
- compare $E'(t)$ and $E(t)$. If they are similar and their difference lays within a previously set margin of error, $E'(t)$ can be considered the electric field of the pulse; otherwise, substitute $E'(t)$ to $E(t)$ and repeat the process until the desired conditions are met.

There are some drawbacks to this method, the main one being that it is not feasible to have information about the sign of the chirp due to the symmetry of $S(\omega,\tau) = S(\omega,-\tau)$. Furthermore, the presence of an iterative algorithm implies an outcome which is not direct,

and we require to scan for many delays, which results in a process that may be lengthy (in the order of a few minutes).

The following are some of the results of FROG reconstructions.

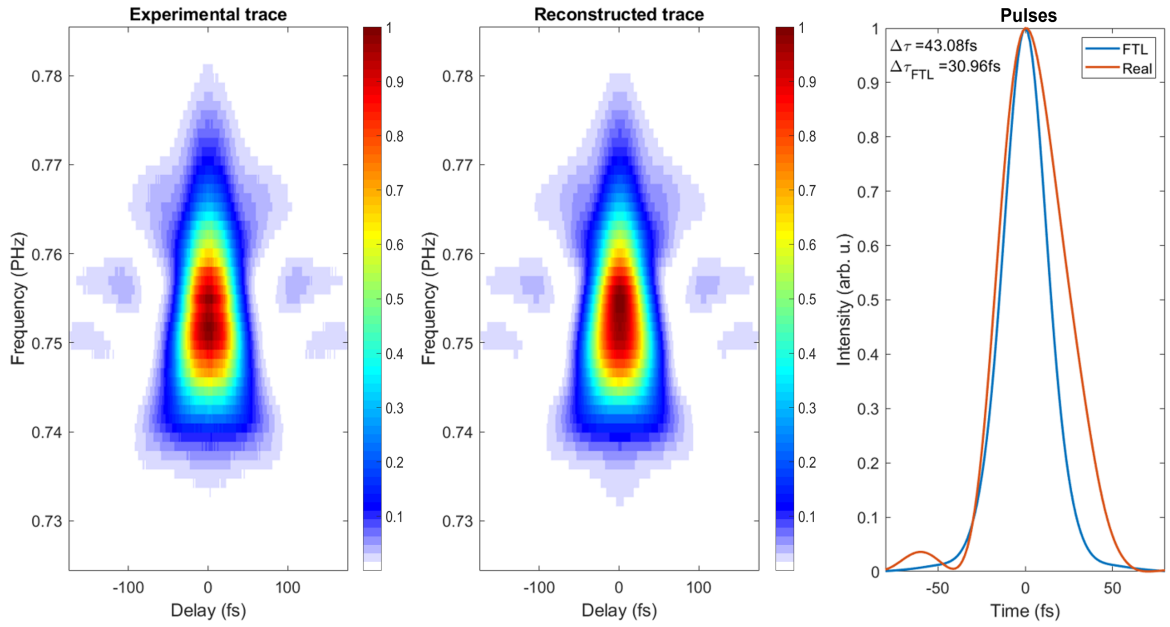

Figure 1.24: FROG example #1.

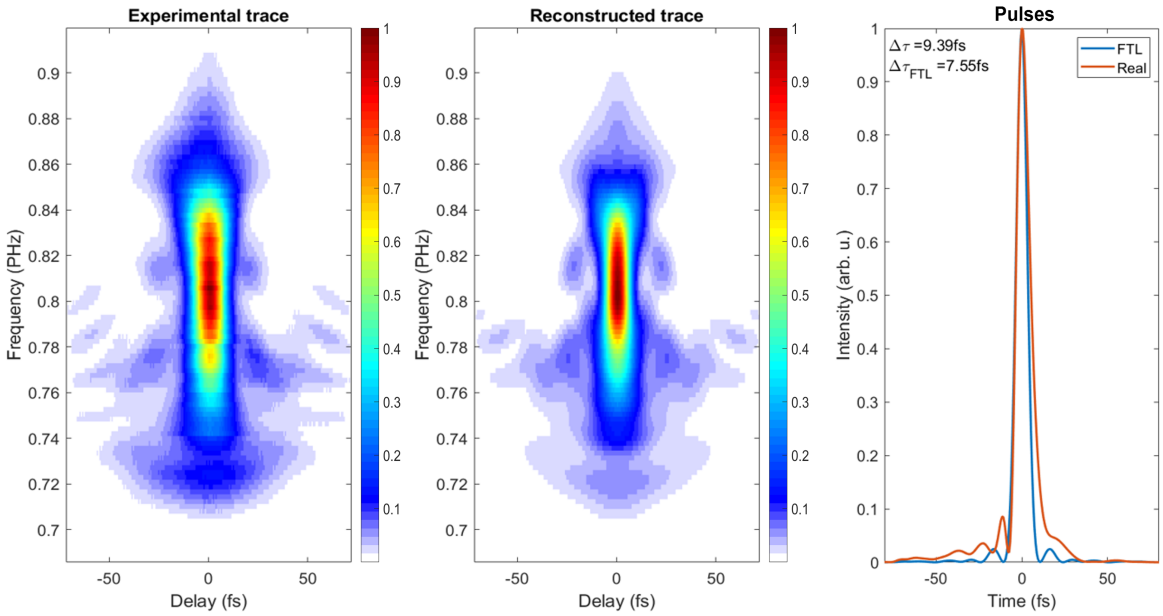

Figure 1.25: FROG example #2.

In the case of Figure 1.24 we have the experimental trace (i.e. the spectrogram) on the left, the FROG reconstruction in the centre, and the reconstructed pulse on the right (orange line), together with its transform limited (blue line). This experiment was performed with an empty fibre ($p = 0$ bars). We can notice that the peak of the IR pulse is around ν_{IR} = 0.755 PHz and its duration is around $\Delta\tau \simeq 44.07$ fs (TL duration of $\Delta\tau_{TL} \simeq 28.87$ fs).

In Figure 1.25, performed at $p = 1.8$ bars, it is possible to find our signal peaking at around $\nu_{IR} = 0.81$ PHz. The duration, on the other hand, is decreased to $\Delta\tau \simeq 9.39$ fs ($\Delta\tau_{TL} \simeq$ 7.55 fs). This is due to the effect of the gas inside the fibre. In fact, the spectrum of the IR beam is not symmetric, and during pulse compression the peak is shifted to higher frequencies. Furthermore, the presence of gas renders the pulse shorter in time, as already explained in Chapter 1.1.4, due to self-focusing and self-phase modulation. Another clear implication is that the spectrogram is broader in frequency due to Fourier theory, going from a $\Delta\nu \simeq 0.045$ PHz to a $\Delta\nu \simeq 0.2$ PHz.

1.3.4. STRIPE reconstruction

Another method used for pulse reconstruction is the **Simplified Trace Reconstruction In the Perturbative regimE** [32]. **STRIPE** is a reconstruction algorithm built on a simplified theoretical model which will be explained in Chapter 2.1.2, based on the *Strong Field Approximation (SFA)* for the free electron in an electric field. Unlike FROG, it is capable of reconstructing pulses "in-situ", which means directly at the sample position. It is also fast and reliable in case of large noise measurements. Moreover, it allows background removal and spurious signal elimination. We are going to use it for the retrieval of the XUV phase and the reconstruction of the XUV pulses.

The main idea behind the algorithm is the following: given in input the IR pulse shape, the XUV spectrum and the experimental spectrogram, a guess is made of the XUV phase (usually null, to begin with); then, a new spectrogram is simulated from those values, it is convoluted with the instrumental response of the ToF spectrometer, and it is compared to the real spectrogram; based on this difference, a new guess is made for the XUV phase, and this process is iterated until the difference between the two spectrograms is close to null within a certain margin. See Figure 1.26 for the final steps of a STRIPE reconstruction.

As we might expect, even with different duration IR pulses the reconstructed XUV pulses are similar one to the other, since in our experiment we only act on the characteristics of the IR pulse (Figure 1.27).

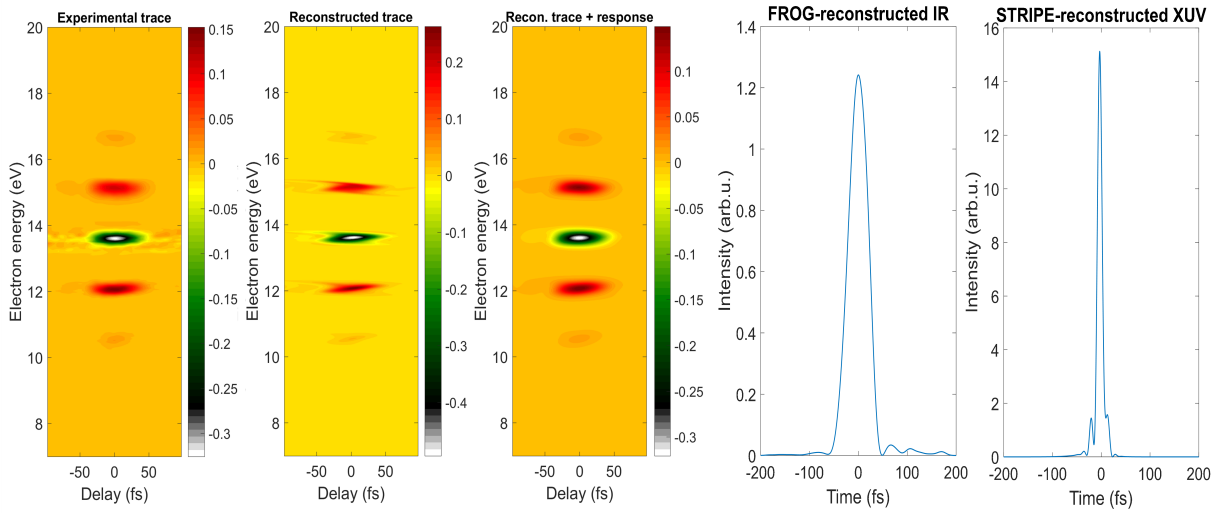

Figure 1.26: From left to right: experimental SHS, STRIPE-reconstructed SHS, convolution of reconstructed SHS and instrumental response, IR pulse, and reconstructed XUV pulse.

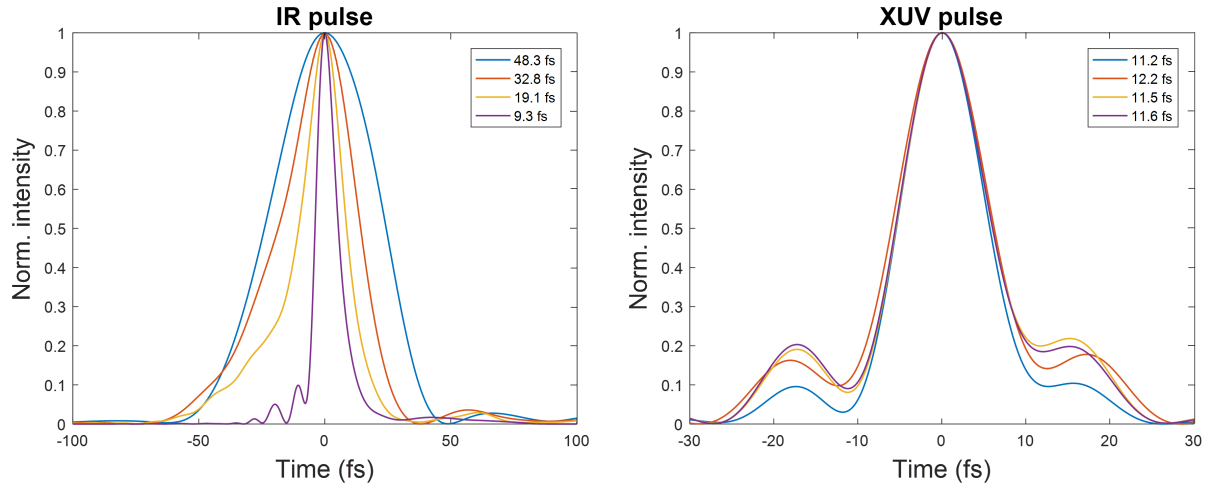

(a) (b)

Figure 1.27: (a) IR pulses with a diverse duration (τ_{IR} = 48.3 fs, 32.8 fs, 17.2 fs, 9.3 fs); (b) XUV pulses with similar features ($\tau_{XUV} \simeq$ 11.6 fs and similar dispersion).

The instrumental response was found experimentally by comparing the energy FWHM of the XUV photons of H23 with the electronic FWHM obtained. It is possible to note that, even if their relation should be linear, it will start to deviate the more we go towards zero. In fact, we will have a non-zero electronic FWHM for a null photonic FWHM. This instrumental response is around 250meV (Figure 1.28).

A few more details on the STRIPE algorithm can be found at the end of Chapter 2.1.2.

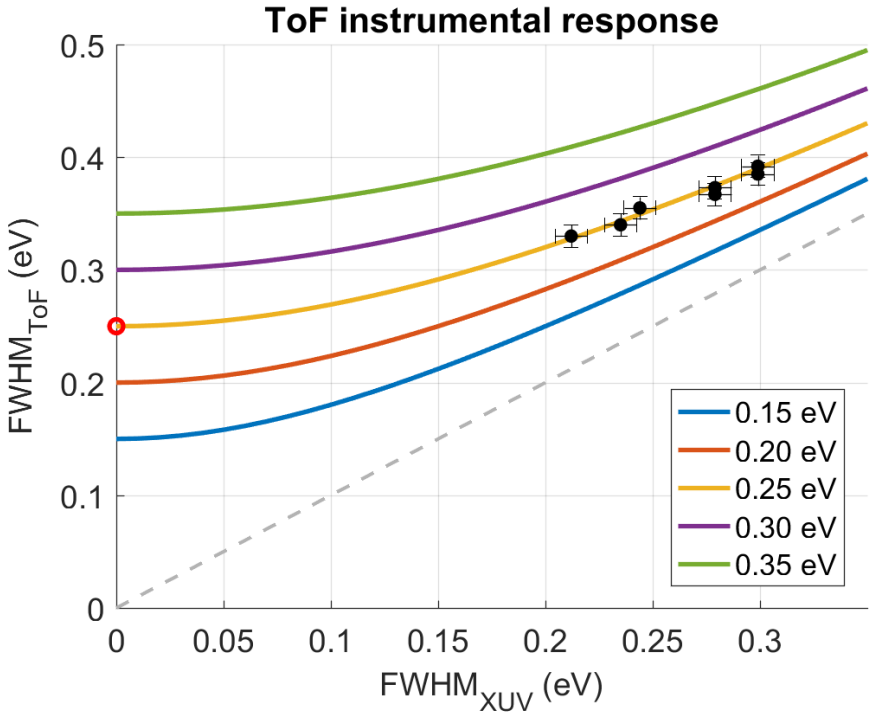

Figure 1.28: Instrument response of ToF spectrometer. Assuming Gaussian curves, we have that $FWHM^2_{Inst.Resp.} = FWHM^2_{ToF} - FWHM^2_{XUV}$, where $FWHM_{ToF}$ is the total FWHM resulting from the convolution, $FWHM_{Inst.Resp.}$ is the one of the instrumental response and $FWHM_{XUV}$ is that of the light pulses. If we measure experimentally $FWHM_{ToF}$ and we have $FWHM_{XUV} = 0$, we find our instrument response. While the yellow line represents the response with XUV pulses of different linewidth, the red circle at 0.25 eV is the actual instrument response with no XUV, and the gray dashed line is the theoretical line, i.e. what should happen if no instrument response was present.

1.3.5. Sideband characterisation and noise removal

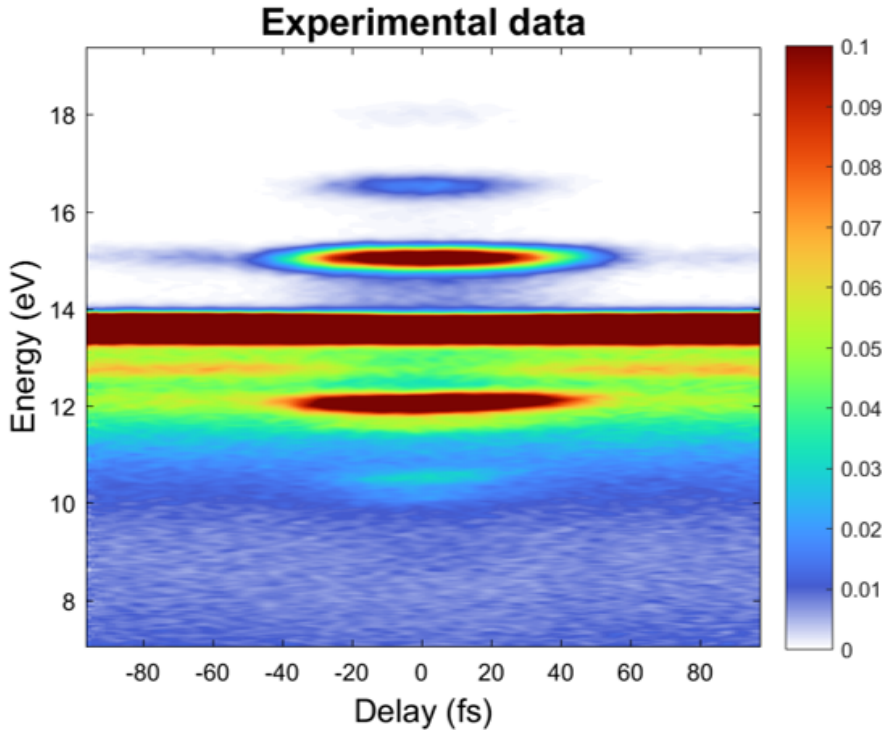

Figure 1.29: SHS raw data of experimental trace. Over-saturated for clarity.

Let us consider an experimental SHS trace, such as the one in Figure 1.29. We immediately notice that noise must be eliminated from the trace. This is a major issue deriving from various electronic effects affecting the trace[9]. This is the reason why the energy profile of our sidebands is never going to be perfectly Gaussian (as we would expect, since the spectrum of the harmonics is Gaussian itself), and instead presents a tail at lower energies. Then, our main goal now is removing this tail to render the sidebands Gaussian.

Firstly, we start by considering a single time delay between pulses, for instance $\tau = 0$. By examining the XUV-only trace, i.e. the trace taken without the presence of IR pulses (Figure 1.30b), we observe that this signal is composed of two parts: a smooth hunch, and a few bounces right before the peak. We are going to remove the smooth part first through a background removal algorithm (Figure 1.31a). This leaves us with the bounces at lower energies. If we draw a Gaussian fit starting from the higher energy end of the spectrum down to where the curve is still roughly Gaussian (Figure 1.31b), we are able to isolate the remaining part of the tail (Figure 1.31c). Finally, we can add up the two

[9]The electronics will behave like an RC circuit, thus possessing a response which resembles a decreasing exponential more than a Dirac delta, which gives our signal its characteristic tail at low energies.

contributions.

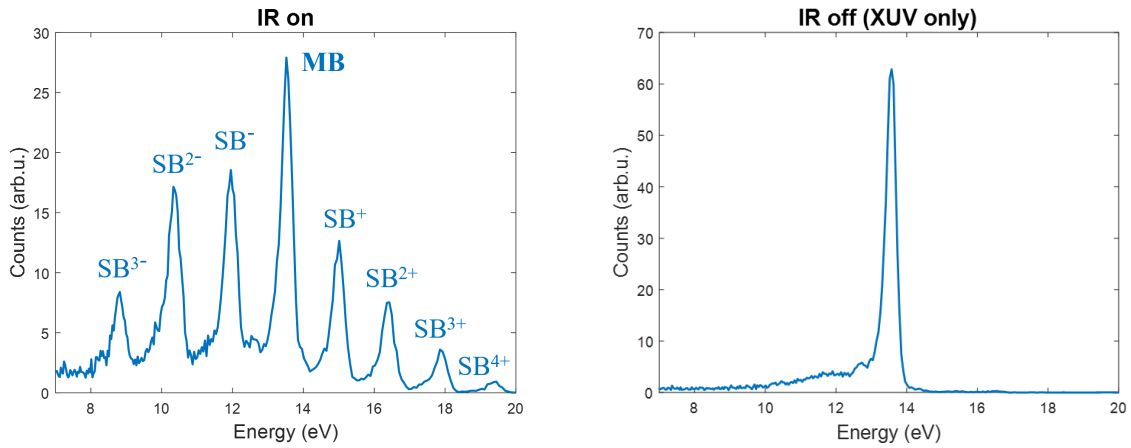

(a) (b)

Figure 1.30: (a) raw signal, which needs to be rid of noise; (b) XUV-only signal, employed for noise characterisation.

If we observe the final shape of the tail, we can see how the noise actually does not go to zero at lower energies. Instead, it seems to be increasing linearly (Figure 1.31d). This is caused by another type of noise, which is due to the presence of the metallic nozzle near the cloud of gas. Some of its electrons are in fact ionised and travel relatively slowly towards the MCP of the ToF, resulting in a linear distribution of low-energy electrons that contributes to the overall noise. Therefore, we are going to remove this noise from the tail to see its actual shape. This final noise tail is present under every peak of the signal, and from previous characterisations we know that it is linearly proportional to the number of counts of each peak of the signal. Now we only need to scale this noise and subtract it from every peak in order to remove it.

Our next step towards noise removal becomes applying another fit to Figure 1.30a to discern the position of the peaks of the main band and sidebands and their area. This in turn will make the tail calculation possible for each of the sidebands and for the main band. After that, we shall subtract the calculated tails from the respective sidebands and main band, starting from the higher energies since they often affect also the lower ones. Afterwards, we are going to remove the linear noise once over the whole signal. Now we have a clean signal for a given time delay (Figure 1.32a). Finally, we are going to use a *super-Gaussian filter* (Figure 1.32b) to remove the residual noise between the peaks, which will also allow an accurate retrieval of the amplitude.

As a last step, for each time delay we are going to normalise our trace, remove the noise,

and then apply the multi-Gaussian fit, so to obtain a complete trace which is devoid of noise (Figure 1.33).

Hence, we now have a full reconstruction of the sidebands and main band amplitude as a function of their energy and the time delay.

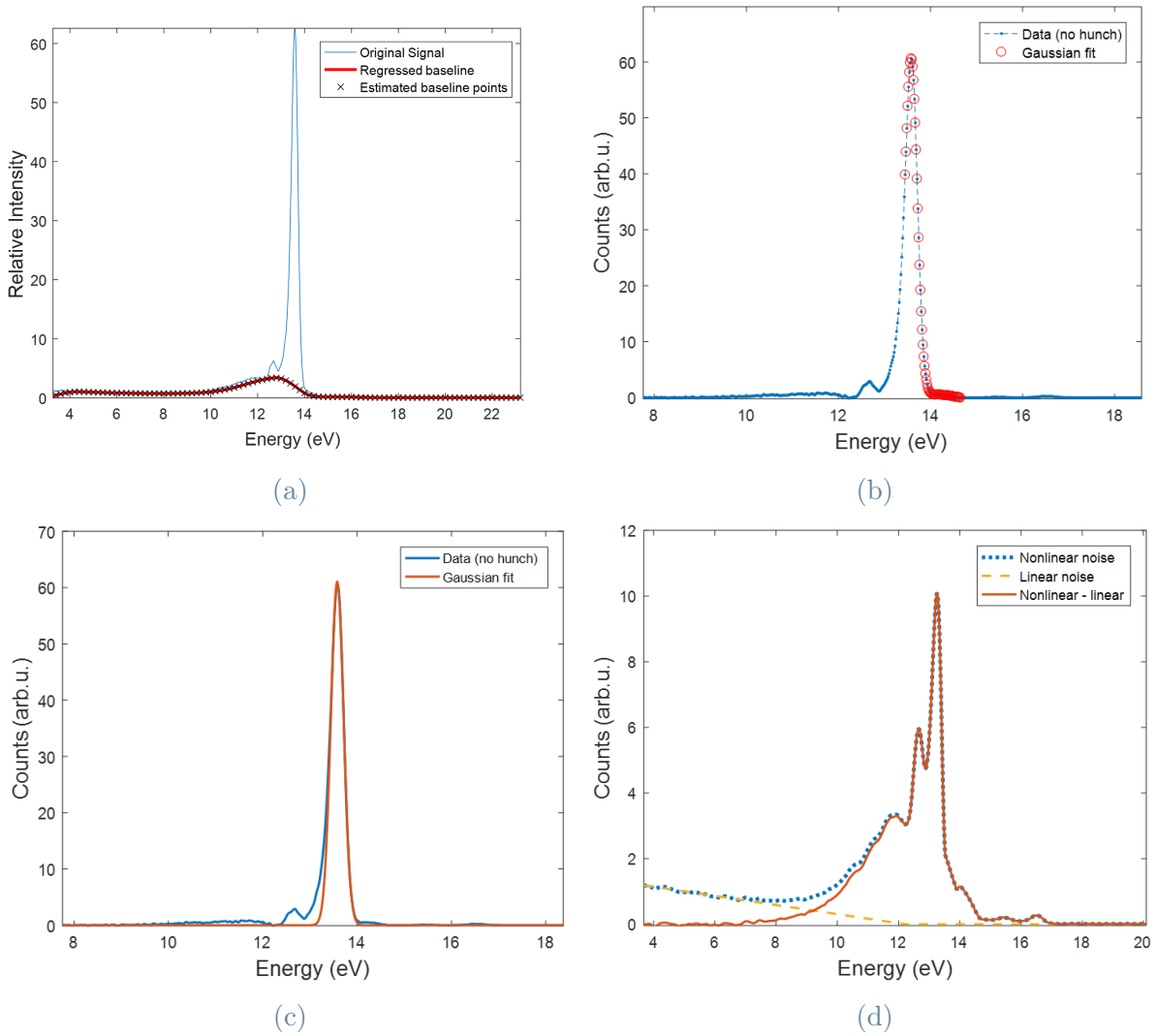

Figure 1.31: Noise tail characterisation. (a) The smooth hunch is found and subtracted; (b) the Gaussian fit is applied on the data (red circles); (c) comparison between Gaussian fit (orange) and original signal (blue), in which the bounces at lower energies are evident; (d) sum of hunch and bounces (blue), linear noise (yellow), and subtraction of the two (orange), which gives the final shape of the tail.

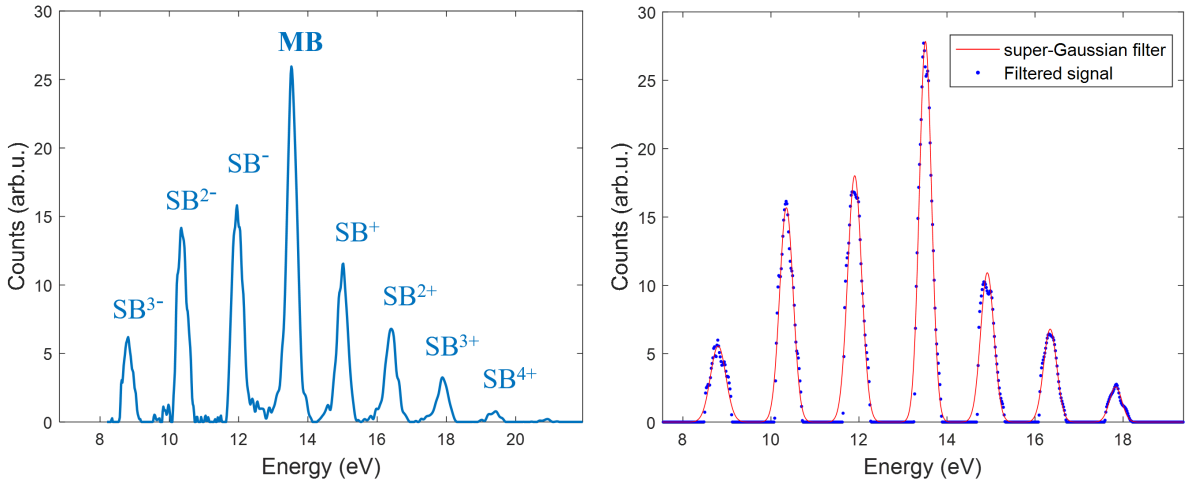

(a) (b)

Figure 1.32: (a) Clean signal; (b) super-Gaussian filter.

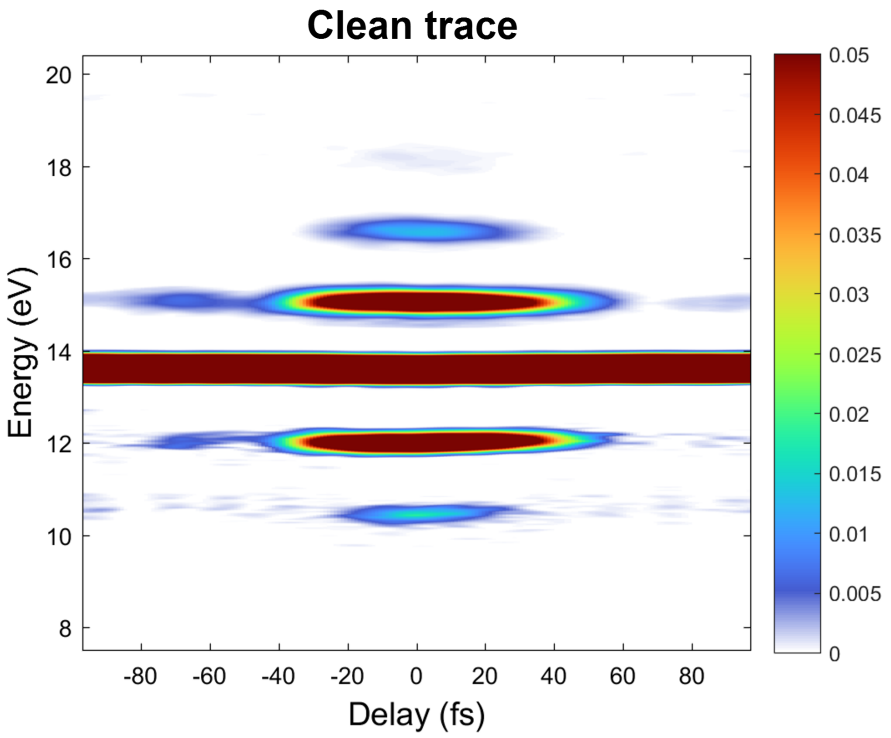

Figure 1.33: Example of clean SHS spectrogram. Over-saturated for clarity.

2 | Floquet theory in the Strong Field Approximation

We already discussed the basic mathematics behind Floquet theory and some of its implications in the Introduction. Now we dive deep into further calculations to apply it to the current case study. We will start from the Strong Field Approximation, to then derive different levels of approximation which are going to frame the main physical parameters driving the phenomenon. We will also investigate how the various approximations relate to one another, and which model we believe to be more reliable.

2.1. Strong Field Approximation (SFA)

Also known as *Keldysh-Faisal-Reiss theory* [24, 29, 34, 49], the **Strong Field Approximation**, or **SFA**, allows to describe numerous phenomena, such as High-order Harmonic Generation (HHG), Above-Threshold Ionisation (ATI), Non-Sequential Multielectron Ionisation (NSMI), or laser-assisted photoelectric effect [1, 29, 34]. Two-colour photoexcitation is no exception.

To introduce such a relevant approach, we start by describing the framework in which it is defined. To start, it is important to specify how we are going to treat both light and matter. We are in fact using a *semi-classical approach*. Therefore, we are choosing to deal with matter as a *quantum* object, while still viewing light in a *classical* way.

Let us start by considering matter. First of all, none of the investigated particles will reach velocities so high to be comparable to the speed of light. Hence, we assume to be working in a *non-relativistic framework*. Second of all, to simplify our discussion, we will consider the *Single Active Electron (SAE)* formulation. This implies the presence of exclusively one electron, which evolves according to the *Time Dependent Schrödinger Equation (TDSE)*:

$$\hat{H}\,|\psi\rangle = i\hbar\frac{\partial}{\partial t}\,|\psi\rangle \tag{2.1.1}$$

in which ψ represents the electron wave function, and the Hamiltonian for light-matter interaction $\hat{H}$ takes the form of

$$\hat{H} = \frac{1}{2m}(\hat{\mathbf{p}} + e\mathbf{A})^2 - e\phi \tag{2.1.2}$$

where we indicated as $\hat{\mathbf{p}}$ the *momentum operator*, $\mathbf{A}$ is the *vector potential*, ϕ is the *scalar potential*, and e and m are the absolute value of the charge of the electron and its mass respectively.

Now let us take a look at the radiation aspect of the model. We will have that it is described on a microscopic level by the *Maxwell equations*:

$$\begin{aligned} \boldsymbol{\nabla} \times \mathbf{E} &= -\frac{\partial \mathbf{B}}{\partial t} \\ \boldsymbol{\nabla} \cdot \mathbf{E} &= \frac{\rho}{\epsilon_0} \\ \boldsymbol{\nabla} \times \mathbf{B} &= \frac{1}{c_0^2}\frac{\partial \mathbf{E}}{\partial t} + \mu_0 \mathbf{J} \\ \boldsymbol{\nabla} \cdot \mathbf{B} &= 0 \end{aligned} \tag{2.1.3}$$

where $\mathbf{E}$ and $\mathbf{B}$ are the electric and magnetic field respectively, ρ is the density of charges, $\mathbf{J}$ is the density of current, ϵ_0 and μ_0 are the dielectric and magnetic constants in vacuum, and c_0 is the speed of light, also calculated in vacuum. Now, usually $\mathbf{E} = \mathbf{E}(\mathbf{r}, t)$, and the same holds for $\mathbf{B}$. Though, here comes into play the first approximation we make: the *dipole approximation*. In the dipole approximation (Figure 2.1) we assume that λ, the wavelength of the electromagnetic field, is so large with respect to the size of the atom ($\lambda >> a$, with a = atomic radius) that it is perceived as uniform in the region in which the particle is present, meaning that $\mathbf{E}(\mathbf{r}, t) \simeq \mathbf{E}(t)$. This approximation has also a dependence on the intensity of the beam (it is therefore valid in the so-called "oasis zone" [30], Figure 2.2), but this does not concern the range of intensities which we are going to utilise.

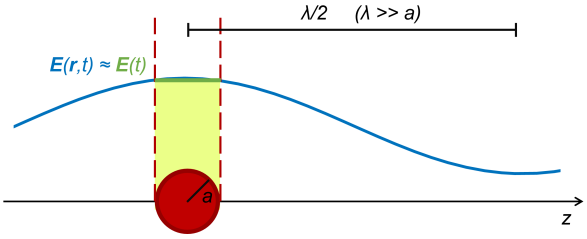

Figure 2.1: Representation of dipole approximation. The field (in blue) is almost constant (green line) in the region in which the particle (red) is present.

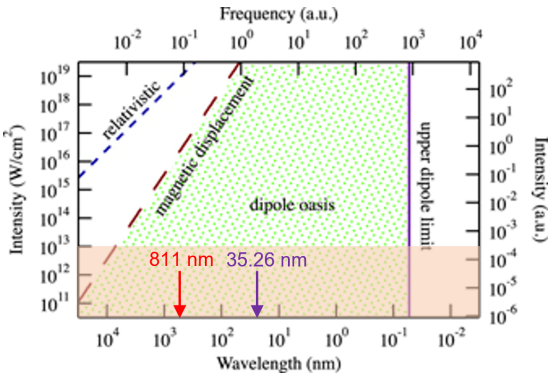

Figure 2.2: Oasis region. Adapted from [30]. In orange, the region of intensities in which we operate. In red and purple, the wavelengths we use.

From this moment forward, we are going to use *atomic units (a.u.)*, i.e. we are going to render some of the main constants we use unitary, namely $\hbar = m = e = 4\pi\epsilon_0 = 1$ a.u. This is mainly for simplicity in calculation. Due to this variation, our TDSE from Eq. (2.1.1) becomes the following:

$$\hat{H}\,|\psi\rangle = i\frac{\partial}{\partial t}\,|\psi\rangle \tag{2.1.4}$$

which has a solution in the Schrödinger picture[1] equal to:

$$|\psi(t)\rangle = e^{-i\int_{t_0}^{t}\hat{H}(t')dt'}\,|\psi(t_0)\rangle \tag{2.1.5}$$

Here, $\hat{H}$ can be written in a way which is akin to Eq. (2.1.2):

$$\hat{H}(t) = \frac{1}{2}(\hat{\mathbf{p}} + \mathbf{A}(t))^2 + V_C \tag{2.1.6}$$

where we substituted ϕ with the Coulomb potential V_C. This is the so-called *velocity gauge*. Actually, this is not the only form that the Hamiltonian can take. Another manner in which it can be written is in fact the *length gauge*:

[1]The Schrödinger picture differs from the Heisenberg picture due to the fact that in the first one wave functions are time dependent, while in the second one operators are. There is also the interaction picture, in which both evolve in time, which is in turn different from both the Schrödinger and the Heisenberg one. All these pictures are equivalent and lead to the same result, albeit we choose to utilize the first one.

$$\hat{H}(t) = -\frac{1}{2}\boldsymbol{\nabla}^2 + V_C + \hat{\mathbf{r}} \cdot \mathbf{E}(t) = \frac{1}{2}\hat{\mathbf{p}}^2 + V_C + \hat{\mathbf{r}} \cdot \mathbf{E}(t) \tag{2.1.7}$$

in which $\hat{\mathbf{r}}$ is our position operator and $\mathbf{E}(t)$ is the electromagnetic field[2].

Now, in order to take a step forward in the direction of the SFA, we start precisely by considering the length gauge[3]. We begin by partitioning the Hamiltonian into two terms, $\hat{H}_0 = -\frac{1}{2}\boldsymbol{\nabla}^2 + V_C$ and $\hat{H}_I(t) = \hat{\mathbf{r}} \cdot \mathbf{E}(t)$, so to have:

$$\hat{H}(t) = \hat{H}_0 + \hat{H}_I(t) \tag{2.1.8}$$

Hence, our solution of Eq. (2.1.5) can be demonstrated[4] to be equal to:

$$|\psi(t)\rangle = -i \int_{t_0}^{t} e^{-i\int_{t'}^{t} \hat{H}(t'')dt''} \hat{H}_I(t') e^{-i\int_{t_0}^{t'} \hat{H}_0(t'')dt''} dt' \, |\psi(t_0)\rangle + e^{-i\int_{t_0}^{t} \hat{H}_0(t'')dt''} |\psi(t_0)\rangle \tag{2.1.9}$$

At this point, we can project the previous solution onto a continuum state $|v\rangle$, so to obtain a coefficient $c(t)$, which taken its square modulus ($|c(t)|^2 = |\langle v|\psi\rangle|^2$) represents the probability to find the electron in a continuum at time t. The aforementioned coefficient takes the shape of:

$$c(t) = -i \int_{t_0}^{t} \langle v| \, e^{-i\int_{t'}^{t} \hat{H}(t'')dt''} \hat{H}_I(t') e^{-i\int_{t_0}^{t'} \hat{H}_0(t'')dt''} dt' \, |\psi(t_0)\rangle + \langle v| \, e^{-i\int_{t_0}^{t} \hat{H}_0(t'')dt''} |\psi(t_0)\rangle \tag{2.1.10}$$

Since $\hat{H}_0$ is time independent, $\displaystyle\int_{t_0}^{t} \hat{H}_0(t'')dt'' = E_0(t - t_0)$ in the second part of the previous formula, and the whole exponential can be brought out of the bracket ($\langle v| \, e^{-i\int_{t_0}^{t} \hat{H}_0(t'')dt''} |\psi(t_0)\rangle = e^{-iE_0(t-t_0)}\langle v|\psi(t_0)\rangle$. This term is therefore negligible because it does not contain any relevant information about the electronic transition. On the other hand, the first term is quite significant, representing the ionisation probability. This term is named *time reversed S-matrix amplitude* ($a(t)$), and it is of fundamental importance for the SFA:

[2] We also recall that $\hat{\mathbf{p}} = -i\boldsymbol{\nabla}$, should it not be obvious from the previous equation.

[3] The same result that we will see in Eq. (2.1.11) can be obtained through the velocity gauge too.

[4] Through a set of equations called Dyson equations [49], which we will not be treating.

$$a(t) = -i \int_{t_0}^{t} \langle v|\, e^{-i\int_{t'}^{t} \hat{H}(t'')dt''} \hat{H}_I(t') e^{-i\int_{t_0}^{t'} \hat{H}_0(t'')dt''} dt'\, |\psi(t_0)\rangle \tag{2.1.11}$$

Finally, it is time to apply the Strong Field Approximation. The SFA takes this result and neglects the effect of Coulomb interaction after ionisation. Therefore, we have that

$$\hat{H}(t) \to \hat{H}(t) = \frac{1}{2}\hat{\mathbf{p}}^2 + \hat{\mathbf{r}} \cdot \mathbf{E}(t) = \frac{1}{2}(\hat{\mathbf{p}} + \mathbf{A}(t))^2 \tag{2.1.12}$$

to substitute inside Eq. (2.1.11). Again, a choice of gauge presents to us. Due to the approximations introduced, it appears that not all gauges result in an accurate description of the physics. As a result, we are forced to decide what to use, and in our case only the length gauge leads to an exact representation. Nevertheless, going against our instincts we shall start by viewing the problem in the velocity gauge, only to switch to the more correct representation towards the end.

Thus, in velocity gauge (here represented by the (V) apex) we have:

$$\hat{H}^{(V)}(t) = \frac{1}{2}\hat{\mathbf{p}}^2 + \hat{\mathbf{r}} \cdot \mathbf{E}(t)$$

We now consider to use as eigenvectors $|v\rangle = |\mathbf{v}(t)\rangle$, where $|\mathbf{v}(t)\rangle$ represents the velocity states, which means that the electron at time t has a velocity $\mathbf{v}$ and a kinetic energy $E_k = \frac{1}{2}|\mathbf{v}|^2$.

Therefore, we wish to solve the following equation, in order to find the first part of the integral in Eq. (2.1.11):

$$\langle v|\, e^{-i\int_{t'}^{t} \hat{H}^{(V)}(t'')dt''} = \langle \mathbf{v}(t)|\, e^{-i\int_{t'}^{t} \hat{H}^{(V)}(t'')dt''} = \langle \Phi(t')|^{(V)} \tag{2.1.13}$$

with $\langle \Phi(t')|^{(V)}$ a generic state, evaluated in the velocity gauge.

The next step is to consider a property of momentum space, which is *completeness*. In general, for a complete and finite set of vectors $|u_k\rangle$, we have

$$\sum_k |u_k\rangle \langle u_k| = 1$$

If extended to a continuum set of vectors such as $|\tilde{\mathbf{p}}\rangle$, the previous formula translates to

$$\int |\tilde{\mathbf{p}}\rangle \langle \tilde{\mathbf{p}}| \, d^3\tilde{p} = 1$$

Hence, we can write:

$$\langle \mathbf{v}(t)| \, e^{-i\int_{t'}^{t} \hat{H}^{(V)}(t'')dt''} = \int \langle \mathbf{v}(t)|\tilde{\mathbf{p}}\rangle \langle \tilde{\mathbf{p}}| \, e^{-i\int_{t'}^{t} \hat{H}^{(V)}(t'')dt''} d^3\tilde{p} = \int \langle \mathbf{v}(t)|\tilde{\mathbf{p}}\rangle \langle \tilde{\mathbf{p}}| \, e^{-i\int_{t'}^{t} \hat{H}^{(V)}(t'',\tilde{\mathbf{p}})dt''} d^3\tilde{p} \tag{2.1.14}$$

where the last equivalence is demonstrated in [49].

At this point, if we define a velocity operator $\hat{\mathbf{v}}(t) = \hat{\mathbf{p}} + \mathbf{A}(t)$ such that $\hat{\mathbf{v}}(t)\,|\mathbf{v}(t)\rangle = \mathbf{v}(t)\,|\mathbf{v}(t)\rangle$, then we can see how we can also define a $\mathbf{p} = \mathbf{v}(t) - \mathbf{A}(t)$ that satisfies $\hat{\mathbf{p}}\,|\mathbf{v}(t)\rangle = \mathbf{p}\,|\mathbf{v}(t)\rangle$. Hence, since we have momentum conservation, at different times t and t' we can write:

$$\mathbf{p} = \mathbf{v}(t) - \mathbf{A}(t) = \mathbf{v}'(t') - \mathbf{A}(t') \tag{2.1.15}$$

resulting in

$$|\mathbf{v}'(t')\rangle = |\mathbf{v}(t) + \mathbf{A}(t') - \mathbf{A}(t)\rangle \tag{2.1.16}$$

Then, our Eq. (2.1.13) becomes:

$$\langle v| \, e^{-i\int_{t'}^{t} \hat{H}^{(V)}(t'')dt''} = \langle \mathbf{v}(t) + \mathbf{A}(t') - \mathbf{A}(t)| \, e^{-i\mathcal{S}(t,t')} \tag{2.1.17}$$

where we have defined the *semi-classical action* $\mathcal{S}(t,t')$ as

$$\mathcal{S}(t,t') = \int_{t'}^{t} \frac{1}{2}(\mathbf{v}(t) - \mathbf{A}(t) + \mathbf{A}(t''))^2 dt'' = \int_{t'}^{t} \frac{1}{2}(\mathbf{p} + \mathbf{A}(t''))^2 dt'' \tag{2.1.18}$$

Now it is time to go back to the length gauge (apex (L)), and we do it by applying the correct transformation, which simply consists in a product with an exponential:

$$\langle \Phi(t')|^{(L)} = \langle \Phi(t')|^{(V)} \, e^{-i\hat{\mathbf{r}}\cdot\mathbf{A}(t')} \tag{2.1.19}$$

By applying the above-mentioned transformation, and by considering $|0\rangle$ as the initial

state $\psi(t_0)$, we obtain a new formula for the a coefficient, also known as the *Keldysh amplitude*:

$$a(t)^{(L)} = -i \int_{t_0}^{t} e^{i(I_P(t'-t_0)-\mathcal{S}(t,t'))} \langle \mathbf{v}(t) + \mathbf{A}(t') - \mathbf{A}(t)| \, e^{-i\hat{\mathbf{r}}\cdot\mathbf{A}(t')} \hat{\mathbf{r}} \cdot \mathbf{E}(t') \, |0\rangle \, dt' \tag{2.1.20}$$

in which I_P is the ionisation potential of the atom.

At last, if we exploit again the property of completeness as we did in Eq. (2.1.14), using this time the position vectors $|\mathbf{r}\rangle$, we can get (after a few calculations, see [49]) a final formula for the Keldysh amplitude:

$$a(t)^{(L)} = -i \int_{t_0}^{t} \mathbf{E}(t') \cdot \mathbf{d}[\mathbf{p} + \mathbf{A}(t')] e^{i(I_P(t'-t_0)-\mathcal{S}(t,t'))} dt' \tag{2.1.21}$$

where $\mathbf{d}[\mathbf{p} + \mathbf{A}(t')]$ represents the *dipole transition*.

2.1.1. SFA for two-colour interaction

Now let us analyse the mathematical consequences of having both an XUV and an IR field.

Given the interaction between a single atom (SAE) and two pulses, a weak XUV ($I_{XUV} \sim 10^6 \div 10^8 \frac{W}{cm^2}$) and a higher IR intensity ($I_{IR} = 10^9 \div 10^{13} \frac{W}{cm^2}$), we can adapt Eq. (2.1.21) to become:

$$a(t) = -i \int_{t_0}^{t} (\mathbf{E}_{IR}(t') + \mathbf{E}_{XUV}(t')) \cdot \mathbf{d}[\mathbf{p} + \mathbf{A}_{IR}(t') + \mathbf{A}_{XUV}(t')] e^{i(I_P(t'-t_0)-\mathcal{S}(t,t'))} dt' \tag{2.1.22}$$

with a semi-classical action redefined as

$$\mathcal{S}(t,t') = \int_{t'}^{t} \frac{1}{2} (\mathbf{p} + \mathbf{A}_{IR}(t'') + \mathbf{A}_{XUV}(t''))^2 dt'' \tag{2.1.23}$$

We can then split $a(t)$ into two components, one depending on E_{IR} and one depending on E_{XUV}:

$$\begin{aligned} a^{IR}(t) &= -i \int_{t_0}^{t} (\mathbf{E}_{IR}(t')) \cdot \mathbf{d}[\mathbf{p} + \mathbf{A}_{IR}(t') + \mathbf{A}_{XUV}(t')] e^{i(I_P(t'-t_0) - \mathcal{S}(t,t'))} dt' \\ a^{XUV}(t) &= -i \int_{t_0}^{t} (\mathbf{E}_{XUV}(t')) \cdot \mathbf{d}[\mathbf{p} + \mathbf{A}_{IR}(t') + \mathbf{A}_{XUV}(t')] e^{i(I_P(t'-t_0) - \mathcal{S}(t,t'))} dt' \end{aligned} \tag{2.1.24}$$

In particular, $a^{IR}(t)$ is the contribution to photoelectron emission due to the IR field, while $a^{XUV}(t)$ is the term related to the direct ionisation caused by the XUV.

Now we need to introduce a series of approximations, which will help us simplify the previous formulas. The first assumption is to have the same linear polarization for both XUV and IR. Then, as previously stated, the XUV beam is much weaker than the IR one. Therefore, it is safe to assume that $|\mathbf{A}_{XUV}| << |\mathbf{A}_{IR}|$. From this, a third approximation stems: a new semi-classical action can be defined as such

$$\begin{aligned} \mathcal{S}(t,t') &= \int_{t'}^{t} \frac{1}{2}(\mathbf{p} + \mathbf{A}_{IR}(t''))^2 dt'' = \\ &= \frac{1}{2}p^2(t-t') + \int_{t'}^{t} \mathbf{p} \cdot \mathbf{A}_{IR}(t'') + \frac{\mathbf{A}_{IR}^2(t'')}{2} dt'' = \\ &= \frac{1}{2}p^2(t-t') - \phi(\mathbf{p}, t') \end{aligned} \tag{2.1.25}$$

Subsequently, we can also make a couple of statements about the initial and final observation times, t and t_0. In fact, we can claim that the observation starts long before the interaction happens, and ends long after it is done, hence we may set $t_0 \to -\infty$ and $t \to +\infty$. This not only changes the extremes of integration in Eqs. (2.1.24), but also eliminates any t dependence from all the complex exponentials. In fact, e^{iQt}, with Q any constant and $t \to \infty$, is a constant phase term which does not influence our final result and may as well be removed.

To summarise, the approximations made are:

- same linear polarization for XUV and IR;
- $|\mathbf{A}_{XUV}| << |\mathbf{A}_{IR}|$;
- $\mathcal{S}(t,t') = \int_{t'}^{t} \frac{1}{2}(\mathbf{p} + \mathbf{A}_{IR}(t''))^2 dt''$;
- $t_0 \to -\infty$;
- $t \to +\infty$;

- $e^{iQt} \xrightarrow{t\to\infty} 0$.

After all these approximations, our coefficients become the following:

$$\begin{aligned} a^{IR}(t) &= -i\int_{-\infty}^{+\infty} \mathbf{E}_{IR}(t')\cdot\mathbf{d}[\mathbf{p}+\mathbf{A}_{IR}(t')]e^{i\phi(\mathbf{p},t')}e^{i(\frac{1}{2}p^2+I_P)t'}dt' \\ a^{XUV}(t) &= -i\int_{-\infty}^{+\infty} \mathbf{E}_{XUV}(t')\cdot\mathbf{d}[\mathbf{p}+\mathbf{A}_{IR}(t')]e^{i\phi(\mathbf{p},t')}e^{i(\frac{1}{2}p^2+I_P)t'}dt' \end{aligned} \tag{2.1.26}$$

At last, we can focus exclusively on the second coefficient $a^{XUV}(t)$ by introducing the delay τ between IR and XUV. Thus, if we rename t' to t for simplicity, we are able to write

$$a(\tau) = -i\int_{-\infty}^{+\infty} \mathbf{E}_{XUV}(t+\tau)\cdot\mathbf{d}[\mathbf{p}+\mathbf{A}_{IR}(t)]e^{i\phi(\mathbf{p},t)}e^{i(\frac{1}{2}p^2+I_P)t}dt \tag{2.1.27}$$

which results in the spectrogram[5]

$$S(\omega,\tau) = |a(\tau)|^2 = \left|\int_{-\infty}^{+\infty} \mathbf{E}_{XUV}(t+\tau)\cdot\mathbf{d}[\mathbf{p}+\mathbf{A}_{IR}(t)]e^{i\phi(\mathbf{p},t)}e^{i(\frac{1}{2}p^2+I_P)t}dt\right|^2 \tag{2.1.28}$$

As a final approximation, we will assume the dipole not to vary significantly due to the flat response of Ne to those XUV frequencies and long durations (many optical cycles), and therefore we assume it to be nearly constant and fix it to $\mathbf{d}\simeq 1$.

$$S(\omega,\tau) = \left|\int_{-\infty}^{+\infty} \mathbf{E}_{XUV}(t+\tau)e^{i\phi(\mathbf{p},t)}e^{i(\frac{1}{2}p^2+I_P)t}dt\right|^2 \tag{2.1.29}$$

where we recall that

$$\phi(\mathbf{p},t) = -\int_{t}^{+\infty} \mathbf{p}\cdot\mathbf{A}_{IR}(t') + \frac{A_{IR}^2(t')}{2}dt' \tag{2.1.30}$$

Thanks to this final formula we are able to model numerically the physics of the experiment happening inside the ToF spectrometer. The following are some of the results obtained through this method.

[5]Not to be confused with the semi-classical action.

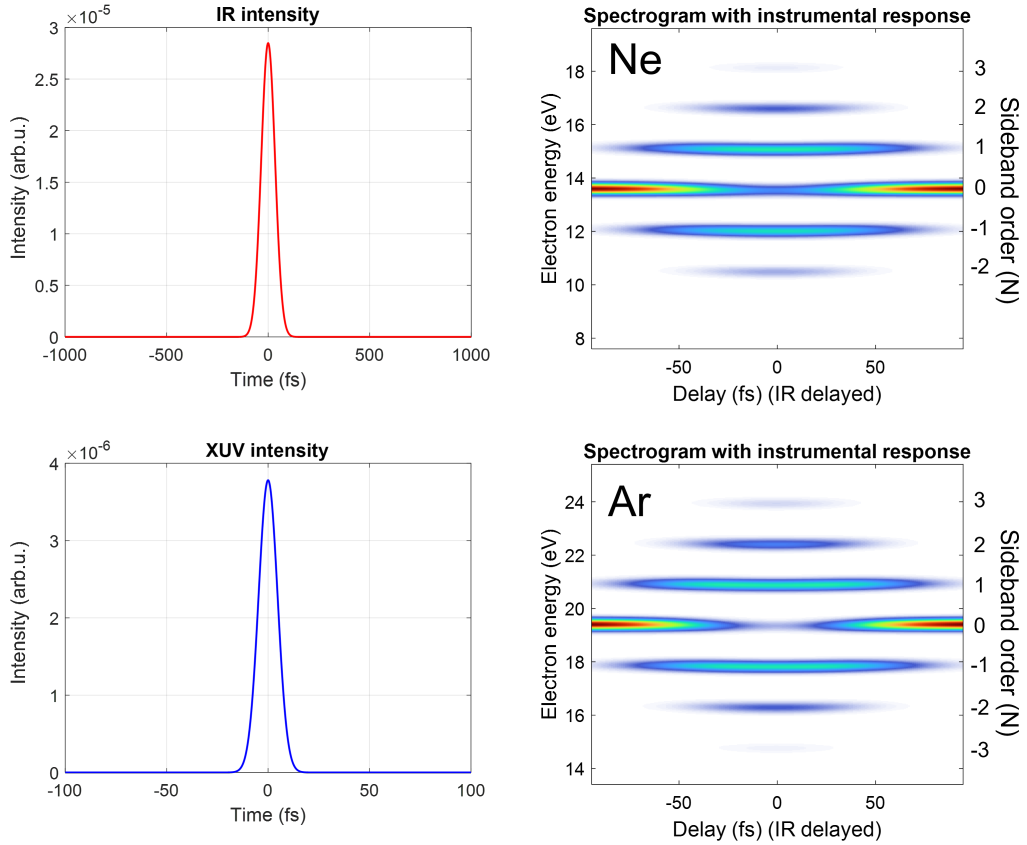

Figure 2.3: Simulation of SFA in the case of Ne and Ar gases. On the left, the generating IR (red) and XUV (blue) pulses. On the right, The results of the simulation in case of Ne (up) and Ar (down) gas. We can see how a different I_P ($I_P^{Ne} = 21.56$ eV, $I_P^{Ar} = 15.76$ eV) allows to obtain different results in terms of the final energy of the main band and of the sidebands.

2.1.2. Simplified SFA model

Now we wish to further simplify this model of Strong Field Approximation. We may start from Eq. (2.1.29) and assume the IR beam to have the shape of

$$\mathbf{A}_{IR} = A_0(t)\cos(\omega_0 t + \varphi) \tag{2.1.31}$$

with $A_0(t)$ being the amplitude, ω_0 the IR frequency, and φ the phase.

Then the IR electric field becomes

$$\mathbf{E}_{IR}(t) = -\frac{\mathrm{d}\mathbf{A}_{IR}(t)}{\mathrm{d}t} = -\frac{\mathrm{d}A_0(t)}{\mathrm{d}t}\cos(\omega_0 t + \varphi) + A_0(t)\omega_0 \sin(\omega_0 t + \varphi) \tag{2.1.32}$$

The next step is to apply the *Central Momentum Approximation (CMA)*: we assume the dependence of ϕ from the momentum $\mathbf{p}$ to be more or less negligible, so that ϕ evaluated in any $\mathbf{p}$ is similar to ϕ calculated in its central value $\mathbf{p}_C$. Hence, $\phi(\mathbf{p}, t) \simeq \phi(\mathbf{p}_C, t) = \phi(t)$.

In particular,

$$p_C = \sqrt{2(\omega_x + N \cdot \omega_0 - I_P)} \tag{2.1.33}$$

where ω_x is the XUV frequency and N indicates the order of the sideband, which may be either positive or negative (or null in case of the main band).

A further assumption we need to make is that the IR intensity is low enough to neglect the second power of $\mathbf{A}_{IR}$ inside the same phase $\phi(t)$. Therefore, our new phase will be

$$\phi(t) = -\int_t^{+\infty} \mathbf{p}_C \cdot \mathbf{A}_{IR}(t')dt' \tag{2.1.34}$$

From this we get

$$S(\omega, \tau) = \left| \int_{-\infty}^{+\infty} \mathbf{E}_{XUV}(t+\tau) e^{-i\int_t^{+\infty} \mathbf{p}_C \cdot \mathbf{A}_{IR}(t')dt'} e^{i(\frac{1}{2}p^2 + I_P)t} dt \right|^2 \tag{2.1.35}$$

Let us work further on the phase term inside Eq. (2.1.35):

$$e^{-i\int_t^{+\infty} \mathbf{p}_C \cdot \mathbf{A}_{IR}(t')dt'} = e^{+i\int_{-\infty}^{t} \mathbf{p}_C \cdot \mathbf{A}_{IR}(t')dt'} \tag{2.1.36}$$

Now, if we consider the previous integral and keep in mind Eq. (2.1.32), we can further explicit the formula as

$$\begin{aligned} \int_{-\infty}^{t} \mathbf{p}_C \cdot \mathbf{A}_{IR}(t')dt' &= \int_{-\infty}^{t} \mathbf{p}_C \cdot \int_{-\infty}^{t'} -\mathbf{E}_{IR}(t'')dt''dt' \simeq \\ &\simeq p_C \int_{-\infty}^{t} \int_{-\infty}^{t'} -A_0(t'')\omega_0 \sin(\omega_0 t'' + \varphi)dt''dt' \simeq \\ &\simeq p_C \frac{A_0}{\omega_0} \sin(\omega_0 t + \varphi) \end{aligned} \tag{2.1.37}$$

in which we have assumed the *long pulse limit* for Eq. (2.1.32) and thus we have approximated $\frac{\mathrm{d}A_0(t)}{\mathrm{d}t} \simeq 0$, so to obtain

$$\mathbf{E}_{IR}(t) \simeq A_0\omega_0 \sin(\omega_0 t + \varphi) \tag{2.1.38}$$

and we have considered $A_0(t) \simeq A_0$ constant inside the integral. We applied the so-called *Slowly-Varying Envelope Approximation (SVEA)*, which treated our IR field as near-monochromatic. From now on, to simplify we will consider the IR beam to be perfectly monochromatic, until otherwise specified.

Hence, we can substitute our result inside Eq. (2.1.39) and obtain the following:

$$e^{+i\int_{-\infty}^{t}\mathbf{p}_C\cdot\mathbf{A}_{IR}(t')dt'} = e^{ip_C\frac{A_0}{\omega_0}\sin(\omega_0 t+\varphi)} \tag{2.1.39}$$

which in turn becomes

$$S(\omega,\tau) = \left|\int_{-\infty}^{+\infty}\mathbf{E}_{XUV}(t+\tau)e^{ip_C\frac{A_0}{\omega_0}\sin(\omega_0 t)}e^{i\omega t}dt\right|^2 \tag{2.1.40}$$

if we substitute Eq. (2.1.39) inside the spectrogram. A further step which has been made in Eq. (2.1.40) is to condense the argument of the second exponential to $i\omega t$, where $\omega = \frac{1}{2}p^2 + I_P$. This was done exclusively for the sake of simplicity. For the same reason, we also set the phase $\varphi = 0$.

We notice that the previous equation corresponds to a Fourier transform, i.e. is in the form $F(\omega) = \mathcal{F}[f(t)] = \int_{-\infty}^{+\infty} f(t)e^{i\omega t}dt$, where f in our case is equal to

$$f(t,\tau) = \mathbf{E}_{XUV}(t+\tau)e^{ip_C\frac{A_0}{\omega_0}\sin(\omega_0 t)} = \mathbf{E}_{XUV}(t+\tau)e^{i\mathbf{p}_C\cdot\frac{\mathbf{E}_{IR}(t)}{\omega_0^2}} \tag{2.1.41}$$

By substituting the final result of Eq. (2.1.41) inside Eq. (2.1.40) we obtain what we named the *simplified model*, which is the one used in STRIPE. This model is way faster to compute than the plain SFA, yet it gives results which are not too different from the ones that can be obtained through mere Strong Field Approximation[6].

At this point, we can make a Fourier frequency expansion of the function $f(t,\tau)$ to obtain a result similar to that of Eq. (0.1.5).[7]

[6] This is true only for weaker IR fields, for which the term $\frac{A_{IR}^2(t')}{2}$ is not truly relevant.

[7] Originally, a time expansion was performed, which did not yield accurate results. Although it was not utilised in the final analysis, it is shown for completeness in Appendix A.

STRIPE Let us open a brief parenthesis on the algorithm employed by STRIPE. We already mentioned in Chapter 1.3.4 the general concept behind STRIPE: the main idea is to use a set of fixed quantities (the IR spectrum, the IR phase, and the XUV spectrum) together with the experimental differential spectrogram to reconstruct the actual phase of the XUV pulse; by starting with a guess of the XUV trace and comparing the reconstructed trace to the real one we manage to achieve such a task.
We start by calculating the spectrogram of IR and XUV, obtained through the product of spectrum and phase:

$$\begin{aligned} S_{IR}(\omega) &= S_{0,IR}(\omega) \cdot e^{-i\phi_{IR}(\omega)} \\ S_{XUV}(\omega) &= S_{0,XUV}(\omega) \cdot e^{-i\phi_{XUV}(\omega)} \end{aligned} \tag{2.1.42}$$

where $S_{0,IR}$ and $S_{0,XUV}$ have already been measured and $\phi_{IR}(\omega)$ is known, while $\phi_{XUV}(\omega)$ is input as a guess. Typically the first guess sees the XUV phase set to 0.
Then, once the two spectrograms have been calculated (one being truly the correct spectrogram and the other being a guess), the two E fields are calculated through the inverse Fourier transform:

$$\begin{aligned} E_{IR}(t) &= \mathcal{F}^{-1}[S_{IR}(\omega)] \\ E_{XUV}(t) &= \mathcal{F}^{-1}[S_{XUV}(\omega)] \end{aligned} \tag{2.1.43}$$

to then be input inside Eq. (2.1.40) as such:

$$S(\omega,\tau) = \left| \int_{-\infty}^{+\infty} \mathbf{E}_{XUV}(t+\tau) e^{i\mathbf{p}_C \cdot \frac{\mathbf{E}_{IR}(t)}{\omega_0^2}} e^{i\omega t} dt \right|^2 = \left| \mathcal{F}\left[\mathbf{E}_{XUV}(t+\tau) e^{i\mathbf{p}_C \cdot \frac{\mathbf{E}_{IR}(t)}{\omega_0^2}} \right] \right|^2 \tag{2.1.44}$$

As a next step, the simulated differential spectrogram is computed by taking the difference between Eq. (2.1.44) and $\left|\mathcal{F}\left[\mathbf{E}_{XUV}(t+\tau)\right]\right|^2$, which is the Fourier transform of the XUV-only trace (no IR present).
Finally, the process is iterated until the difference between experimental trace and calculated trace is minimised within chosen limits.

2.2. Frequency (Bessel) expansion

If we take a look at Eq. (2.1.41), we notice that the exponential term is written in the form $e^{iz\sin(\vartheta)}$, and therefore we are able to use the *Jacobi-Anger expansion*:

$$e^{iz\sin(\vartheta)} = \sum_{n=-\infty}^{+\infty} J_n(z)e^{in\vartheta} \tag{2.2.1}$$

In this equation $J_n(z)$ represents the *Bessel function of the first kind* of order n, and it is dependent on z, which in our case equals to $p_C\frac{A_0}{\omega_0}$. Moreover, $\vartheta = \omega_0 t$.

We are therefore able to write Eq. (2.1.41) as follows:

$$f(t,\tau) = \mathbf{E}_{XUV}(t+\tau)\sum_{n=-\infty}^{+\infty} J_n\left(p_C\frac{A_0}{\omega_0}\right)e^{in\omega_0 t} \tag{2.2.2}$$

Now we recall that the sine function is an odd function, so to be able to write

$$\sum_{n=-\infty}^{+\infty} J_n(z)e^{in\vartheta} = e^{iz\sin(\vartheta)} = e^{-iz\sin(-\vartheta)} = \sum_{n=-\infty}^{+\infty} J_n(-z)e^{-in\vartheta} \tag{2.2.3}$$

As a final step, we can write the XUV electric field in its complex representation, that is

$$\mathbf{E}_{XUV}(t) = \frac{E_{XUV}(t)}{2}e^{-i\omega_x t} + c.c. \tag{2.2.4}$$

where ω_x is the XUV frequency. The consequence of Eq. (2.2.4) is then

$$S(\omega,\tau) = \left|\mathcal{F}\left[\frac{E_{XUV}(t+\tau)}{2}e^{-i\omega_x(t+\tau)}\sum_{n=-\infty}^{+\infty} J_n\left(-p_C\frac{A_0}{\omega_0}\right)e^{-in\omega_0 t}\right]\right|^2 \tag{2.2.5}$$

in which we discarded the complex conjugate (*c.c.*) because it would have contributed with negative frequencies, which are clearly not physical.

It is now plain to see how each term in Eq. (2.2.5) represents a single sideband. In fact, by analysing the phase term we notice that the resulting frequency of each term is equal to the sum of the central XUV frequency ω_x, and a multiple of the IR frequency ω_0. For instance, for $n = 0$ we find the main band, at frequency ω_x; at $n = \pm 1$ we have the first two sidebands with a frequency of $\omega_x \pm \omega_0$, i.e. SB^+ and SB^-; if $n = \pm 2$ the frequency will

be $\omega_x \pm 2\omega_0$, representing SB^{++} (or SB^{2+}) and SB^{--} (or SB^{2-}), and so on. This is quite useful, for not every model has this kind of one-to-one correspondence (see Appendix A).

In order to further approximate Eq. (2.2.5) we can also consider the XUV field to be almost monochromatic, therefore losing its time dependence and having $E_{XUV}(t+\tau) \simeq E_x$. Moreover, we can discard the term $e^{-i\omega_x\tau}$, being a pure phase term. This results in having

$$S(\omega,\tau) = \left| \mathcal{F}\left[E_x \sum_{n=-\infty}^{+\infty} J_n\left(-p_C \frac{A_0}{\omega_0}\right) e^{-i(\omega_x + n\omega_0)t} \right] \right|^2 \tag{2.2.6}$$

Consequently, If we normalise with respect to the XUV spectral area $E_{XUV} \simeq E_x$ and we consider the SB amplitude as a function of I_{IR}, we find that each amplitude is represented by the square modulus of a Bessel function in which the SB order corresponds to the order n of the function, thus having: $MB = \left|J_0\left(-p_C\frac{A_0}{\omega_0}\right)\right|^2$, $SB^{\pm} = \left|J_{\pm1}\left(-p_C\frac{A_0}{\omega_0}\right)\right|^2$, $SB^{2\pm} = \left|J_{\pm2}\left(-p_C\frac{A_0}{\omega_0}\right)\right|^2$, etc..., which depend on the central momentum[8], on the IR amplitude, and on the IR frequency.

The following graphs (Figure 2.4) show how the amplitude of the sidebands behaves at different intensities in correspondence of $\tau = 0$.

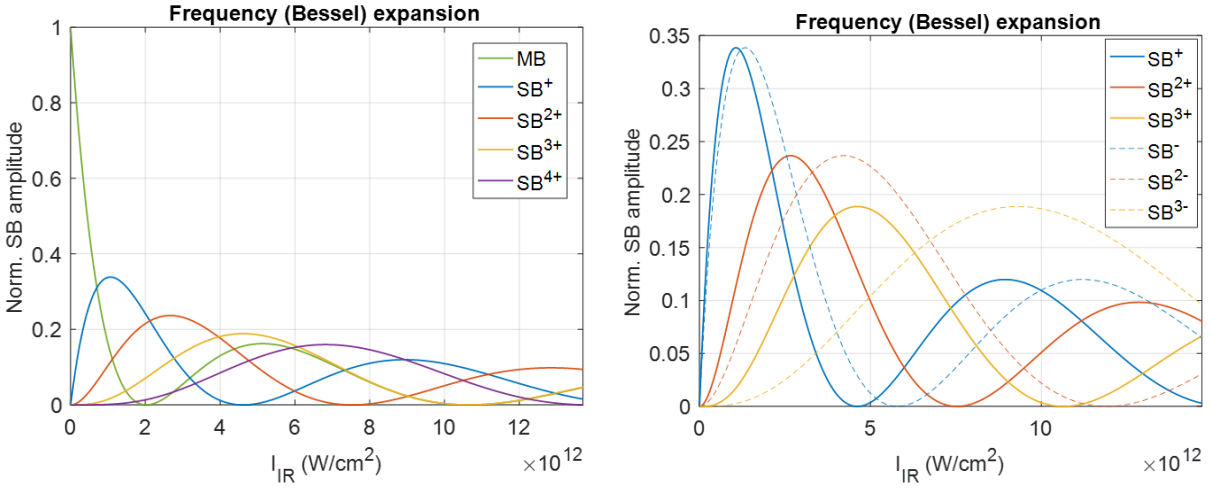

(a) (b)

Figure 2.4: (a) Main band and first four positive sidebands for monochromatic IR beam; (b) first three positive (solid line) and three negative (dashed line) sidebands for monochromatic IR beam.

[8]Note that to have a higher agreement with the SFA approximation and to have a less severe CMA we consider $\mathbf{p}_C = \mathbf{p}_{C,SB^{\pm}}$ for $SB^{\pm}$, $\mathbf{p}_C = \mathbf{p}_{C,SB^{2\pm}}$ for $SB^{2\pm}$, and so on.

As anticipated in Chapter 1.2 and demonstrated by Figure 2.4, the sidebands do not increase indefinitely, they oscillate instead. After reaching its first peak, each sideband will begin its depletion. The electrons from the depleting sideband end up populating higher-order sidebands, up until the point in which the sideband will be completely empty. Then, it will reprise its growth towards a second, lower peak, which in turn is going to decrease at even higher intensities, and so on. This behaviour is valid for all sidebands, whose amplitudes with respect to the IR intensity all follow this Bessel function shape. It is worth noting that higher order sidebands entail lower peaks at higher intensities.

Nonetheless, if we compare positive and negative sidebands of the same order we notice that even though the height of the peaks is identical, the negative sidebands are going to have peaks at higher intensities, and the Bessel function overall will be more stretched. This is caused by having essentially the same function (recall that $|J_n(z)|^2 = |J_{-n}(z)|^2$) but with a different argument. In fact, the central momentum is going to vary from sideband to sideband, being calculated for a different frequency each time, and this will yield the results of Figure 2.4b.

Up to this moment we only took into consideration monochromatic beams. In our experiments we can replicate said beams by using long duration pulses, but we would also like to know the behaviour of the model in the case of shorter pulses. To do so, we can follow the path of the *non-adiabatic approach*. For this approach we are going to hypothesize *Gaussian pulses* with duration of τ_{XUV} and τ_{IR} for XUV and IR respectively.

2.2.1. Non-adiabatic approach

In Eq. (2.1.38) we considered A_0 to have such slow, adiabatic variations in time to be basically constant. Now let us go back to having fields that are dependent on time. In particular, we choose the IR pulse to have $A_0(t) = \frac{1}{\omega_0} E_0 e^{-\frac{t^2}{\tau_{IR}^2}}$. Similarly, the XUV pulse will reprise its time dependence and we will write $E_{XUV}(t+\tau) = E_x e^{-\frac{(t+\tau)^2}{\tau_{XUV}^2}}$. Then, Eq. (2.2.6) for SB^+ becomes[9]

$$SB^+(\omega,\tau) \doteq S_{SB^+}(\omega,\tau) = \left| \mathcal{F}\left[E_x e^{-\frac{(t+\tau)^2}{\tau_{XUV}^2}} J_1\left(-p_C \frac{E_0}{\omega_0^2} e^{-\frac{t^2}{\tau_{IR}^2}} \right) e^{-i(\omega_x+\omega_0)t} \right] \right|^2 \tag{2.2.7}$$

This is the Fourier transform of a Bessel function of the first kind with a Gaussian argu-

[9] From now on we are going to consider positive sidebands only, since negative ones behave similarly.

ment. Considering the general form of a Bessel function in Eq. (2.2.8), it is possible to calculate a numerical approximation of the SB^+, as indicated in the following steps.

$$J_n(z) = \left(\frac{z}{2}\right)^n \sum_{k=0}^{+\infty} \frac{(-1)^k \left(\frac{z}{2}\right)^{2k}}{k!\,\Gamma(n+k+1)} \tag{2.2.8}$$

with the Γ function indicated below[10]:

$$\Gamma(x) = \int_0^{+\infty} t^{x-1} e^{-t} dt \qquad\qquad \Gamma(x+1) = x!$$

Then, naturally:

$$J_1\left(-p_C \frac{E_0}{\omega_0^2} e^{-\frac{t^2}{\tau_{IR}^2}}\right) = -\frac{p_C E_0}{2\omega_0^2} e^{-\frac{t^2}{\tau_{IR}^2}} \sum_{k=0}^{+\infty} \frac{(-1)^k \left(-\frac{p_C E_0}{2\omega_0^2}\right)^{2k} e^{-2k\frac{t^2}{\tau_{IR}^2}}}{k!\;(k+1)!} \tag{2.2.9}$$

From numerical computations we are able to observe that we can take the Gaussian exponential out of the Bessel function without incurring in a significant error:

$$J_1\left(-p_C \frac{E_0}{\omega_0^2} e^{-\frac{t^2}{\tau_{IR}^2}}\right) \simeq J_1\left(-p_C \frac{E_0}{\omega_0^2}\right) e^{-\frac{t^2}{\tau_{IR}^2}} \tag{2.2.10}$$

Hence, a new analytical formula for the SB^+ amplitude presents to us, which better approximates the results of the SFA. By normalizing to the area of the XUV pulse (i.e. $\sqrt{\pi}\tau_{XUV}E_x$) we get that the value of the sideband amplitude in $\tau = 0$ is

$$SB_0^+ \simeq \left| J_1\left(-p_C \frac{E_0}{\omega_0^2}\right) \right|^2 \frac{1}{\sqrt{1 + \frac{\tau_{XUV}^2}{\tau_{IR}^2}}} \tag{2.2.11}$$

An analogous reasoning can be applied to SB^{2+}, obtaining

$$J_2\left(-p_C \frac{E_0}{\omega_0^2} e^{-\frac{t^2}{\tau_{IR}^2}}\right) \simeq J_2\left(-p_C \frac{E_0}{\omega_0^2}\right) e^{-2\frac{t^2}{\tau_{IR}^2}} \tag{2.2.12}$$

and finally

[10]The Gamma Function $\Gamma(x)$ is an extension of the concept of factorial numbers. It draws a curve which interpolates factorial numbers, giving a value to $x!$ even if $x \notin \mathbb{N}$.

$$SB_0^{2+} \simeq \left| J_2\left(-p_C \frac{E_0}{\omega_0^2}\right)\right|^2 \frac{1}{\sqrt{1+2\frac{\tau_{XUV}^2}{\tau_{IR}^2}}} \,. \tag{2.2.13}$$

More in general, for $N \in \mathbb{Z}$ we obtain

$$SB_0^{N\pm} \simeq \left| J_N\left(-p_C \frac{E_0}{\omega_0^2}\right)\right|^2 \frac{1}{\sqrt{1+|N|\frac{\tau_{XUV}^2}{\tau_{IR}^2}}} \tag{2.2.14}$$

If we analyse again the sideband intensity with respect to the intensity of the IR pulse, we discern a pattern which is quite similar to the previous one, yet holds substantial differences (Figure 2.5).

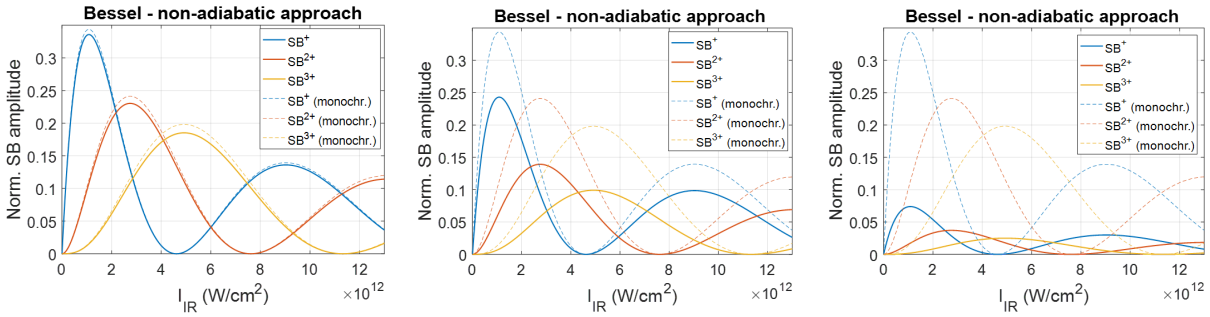

(a) $\tau_{IR} = 50$ fs, $\tau_{XUV} = 11$ fs. (b) $\tau_{IR} = 11$ fs, $\tau_{XUV} = 11$ fs. (c) $\tau_{IR} = 11$ fs, $\tau_{XUV} = 50$ fs.

Figure 2.5: Comparison between non-adiabatic expansion and monochromatic case at different time durations of IR and XUV.

Here we can see how decreasing the IR pulse duration with respect to the XUV one causes a decrease in the sideband amplitude, while still having the zeros of the Bessel functions at the same IR intensity. Indeed, if we calculate the limit for $\frac{\tau_{XUV}^2}{\tau_{IR}^2} \to +\infty$ (i.e. for $\tau_{IR} \to 0$) we find that the square roots in Eq. (2.2.11) and Eq. (2.2.13) tend to 0. On the other hand, if $\frac{\tau_{XUV}^2}{\tau_{IR}^2} \to 0$ (i.e. $\tau_{IR} \to +\infty$)), then the limit of those square roots is 1. For $\tau_{IR} = \tau_{XUV}$ instead we have different results for each sideband. It is worth mentioning that in the case of the first sideband this results in a $\frac{1}{\sqrt{2}}$ decrease in amplitude.

Now let us focus on what happens to the sideband amplitude if we fix the IR intensity and the XUV duration and let τ_{IR} vary. Let us also compare these results with our SFA simulations, where we have assumed to have perfectly Gaussian pulses.

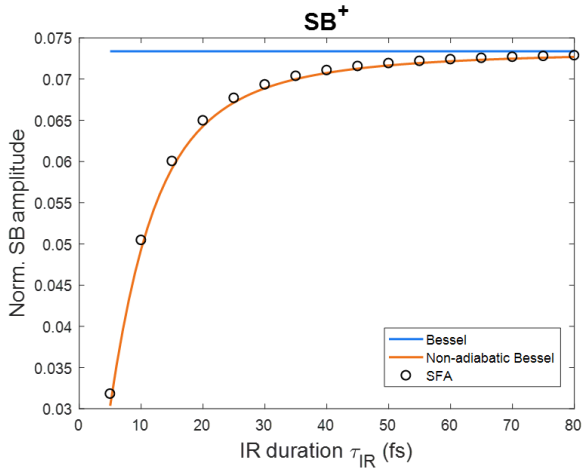

(a) $I_{IR} = 10^{11} \frac{W}{cm^2}$, $\tau_{XUV} = 11$ fs.

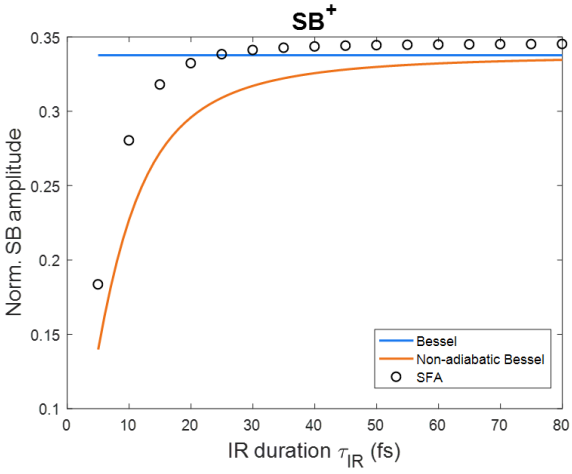

(b) $I_{IR} = 10^{12} \frac{W}{cm^2}$, $\tau_{XUV} = 11$ fs.

Figure 2.6: Dependence of the amplitude of SB^+ on τ_{IR}. In these graphs three models are compared: the time-independent Bessel, the non-adiabatic Bessel, and SFA model.

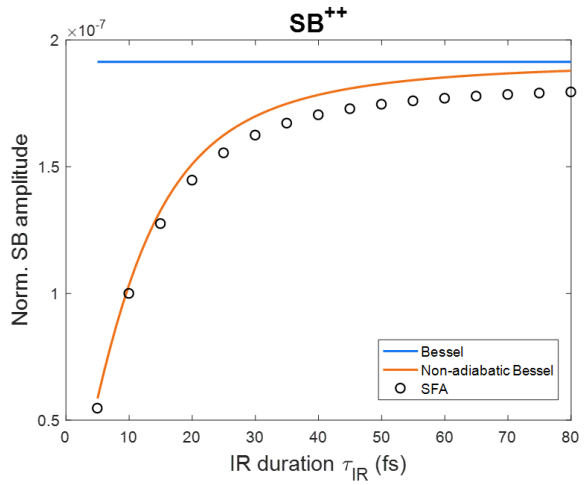

(a) $I_{IR} = 10^{9} \frac{W}{cm^2}$, $\tau_{XUV} = 11$ fs.

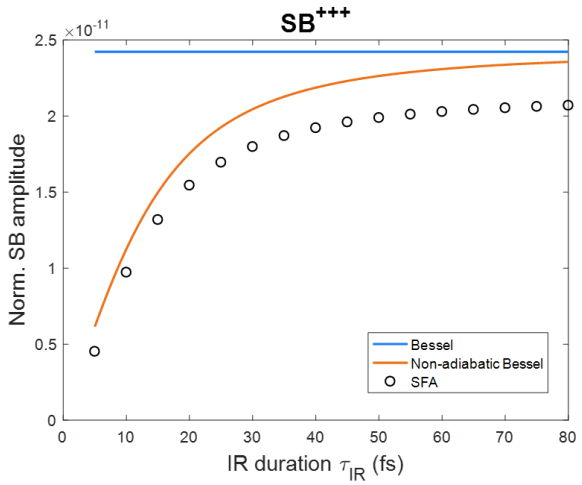

(b) $I_{IR} = 10^{9} \frac{W}{cm^2}$, $\tau_{XUV} = 11$ fs.

Figure 2.7: Dependence of the amplitude of SB^{++} and SB^{+++} on τ_{IR}. In these graphs three models are compared: the time-independent Bessel, the non-adiabatic Bessel, and SFA model.

From Figure 2.6 we immediately notice how our simple Bessel approximation behaves as an asymptote for both the SFA simulations and the non-adiabatic approximation in the case of SB^+. In fact, the simple Bessel function calculated in the previous section was time independent, treating $A_0(t)$ as constant.

If we now focus on the comparison between the non-adiabatic approximation and the

SFA, we notice a solid agreement between the two models for the first sideband up to an intensity of $I_{IR} < 10^{11} \frac{W}{cm^2}$. Afterwards, the two curves start diverging one from the other, more and more for shorter IR pulses. Moreover, at longer IR duration the SFA simulations and the non-adiabatic model do not tend to the same asymptote any longer.

An analogous observation can be made for higher order sidebands (Figure 2.7), for which the agreement between SFA and time-dependent Bessel is already unconvincing at $I_{IR} \simeq 10^9 \frac{W}{cm^2}$. This disagreement is not to be attributed to the CMA, which has a less relevant impact on the matter, but mainly to the missing term $\frac{A_{IR}^2}{2}$ inside Eq. (2.1.30), which is no longer negligible.

2.2.2. Addition of the quadratic term

As we noticed from the previous analysis, the behaviour at higher intensities makes so that we cannot ignore the quadratic term anymore.

By including again $\frac{\mathbf{A}_{IR}^2(t)}{2}$ inside the phase $\phi(\mathbf{p}, t)$ we bring it back to the form of Eq. (2.1.30). Hence, we can separate the integral into two terms as such:

$$\phi(\mathbf{p}, t) = -\int_t^{+\infty} \mathbf{p} \cdot \mathbf{A}_{IR}(t') - \int_t^{+\infty} \frac{A_{IR}^2(t')}{2} dt' \tag{2.2.15}$$

We choose to focus on the last term, since the analysis of the first one yields the same result as before. If we consider that $A_{IR}(t) = A_0(t)\cos(\omega_0 t) = \frac{E_0(t)}{\omega_0}\cos(\omega_0 t)$, then we are able to write

$$A_{IR}^2(t) = \frac{E_0^2(t)}{\omega_0^2}\cos^2(\omega_0 t) = \frac{E_0^2(t)}{\omega_0^2}\left[\frac{1+\cos(2\omega_0 t)}{2}\right] \tag{2.2.16}$$

Here we have assumed $E_0(t)$ to be Gaussian and therefore take the form of $E_0(t) = E_0 e^{-\frac{t^2}{\tau_{IR}^2}}$. Consequently, $E_0^2(t)$ is going to be Gaussian too, but with a time duration which is shorter of $\frac{1}{\sqrt{2}}$. In fact, $E_0^2(t) = E_0^2 e^{-2\frac{t^2}{\tau_{IR}^2}} = E_0^2 e^{-\frac{t^2}{(\tau_{IR}/\sqrt{2})^2}}$.

Now, we can simplify the second term of Eq. (2.2.15) as indicated below:

$$-\int_t^{+\infty} \frac{A_{IR}^2(t')}{2} dt' = -\int_{-\infty}^{+\infty} \frac{A_{IR}^2(t')}{2} dt' + \int_{-\infty}^{t} \frac{A_{IR}^2(t')}{2} dt' \simeq \int_{-\infty}^{t} \frac{E_0^2(t')}{\omega_0^2}\left[\frac{1+\cos(2\omega_0 t')}{4}\right] dt' \tag{2.2.17}$$

where we have neglected the first term, as it yields a constant phase term.

We can further separate the integral of Eq. (2.2.17) into two parts:

$$\int_{-\infty}^{t} \frac{E_0^2(t')}{\omega_0^2}\left[\frac{1+\cos(2\omega_0 t')}{4}\right]dt' = \int_{-\infty}^{t} \frac{E_0^2(t')}{4\omega_0^2}dt' + \int_{-\infty}^{t} \frac{E_0^2(t')}{4\omega_0^2}\cos(2\omega_0 t')dt' \tag{2.2.18}$$

The first term can again be neglected, as it results in an almost linear contribution which is small enough in the limits given by the size of the pulse. The second one can be easily calculated applying the SVEA:

$$\int_{-\infty}^{t} \frac{E_0^2(t')}{4\omega_0^2}\cos(2\omega_0 t')dt' \simeq \frac{E_0^2(t)}{8\omega_0^2}\sin(2\omega_0 t) \tag{2.2.19}$$

As a result, the spectrogram of Eq. (2.1.29) becomes

$$S(\omega,\tau) = \left|\int_{-\infty}^{+\infty} \mathbf{E}_{XUV}(t+\tau)e^{ip_C\frac{E_0(t)}{\omega_0^2}\sin(\omega_0 t)}e^{i\frac{E_0^2(t)}{8\omega_0^3}\sin(2\omega_0 t)}e^{i\omega t}dt\right|^2 \tag{2.2.20}$$

which is the Fourier transform of

$$f(t+\tau) = \mathbf{E}_{XUV}(t+\tau)\sum_{n=-\infty}^{+\infty} J_n\left(p_C\frac{E_0(t)}{\omega_0^2}\right)e^{in\omega_0 t}\cdot\sum_{m=-\infty}^{+\infty} J_m\left(\frac{E_0^2(t)}{8\omega_0^3}\right)e^{im2\omega_0 t}$$

By using a transformation akin to that of Eq. (2.2.3) we can also write it as

$$f(t+\tau) = \mathbf{E}_{XUV}(t+\tau)\sum_{n=-\infty}^{+\infty} J_n\left(-p_C\frac{E_0(t)}{\omega_0^2}\right)e^{-in\omega_0 t}\cdot\sum_{m=-\infty}^{+\infty} J_m\left(-\frac{E_0^2(t)}{8\omega_0^3}\right)e^{-im2\omega_0 t} \tag{2.2.21}$$

That product of sums of Bessel functions can be simplified in notation if we introduce the *generalised Bessel function*

$$\mathcal{J}_n(u,v) = \sum_{m=-\infty}^{+\infty} J_n(u)\cdot J_m(v) \tag{2.2.22}$$

with $u = -p_C \frac{E_0(t)}{\omega_0^2}$ and $v = -\frac{E_0^2(t)}{8\omega_0^3}$. Hence, Eq. (2.2.21) becomes

$$f(t+\tau) = \mathbf{E}_{XUV}(t+\tau) \sum_{n=-\infty}^{+\infty} \mathcal{J}_n(u,v) e^{-i(n+2m)\omega_0 t} \tag{2.2.23}$$

Therefore, we can easily notice that these terms oscillate at frequency $(n+2m)\omega_0$. Then, if we want to consider only the first (upper) sideband, we have to take into account only the terms at a frequency ω_0. This implies having $n+2m=1$, which is possible to obtain for different (n,m) couples. From a numerical analysis it results that the more relevant contributions come from the couples (-1,1) and (1,0).

For this reason, we can reprise Eq. (2.2.11) and write

$$\begin{aligned} SB_0^+ &= \left| \sum_{\substack{n=-\infty \\ n+2m=1}}^{+\infty} \mathcal{J}_n(u,v) \right|^2 \frac{1}{\sqrt{1+\frac{\tau_{XUV}^2}{\tau_{IR}^2}}} \simeq \\ &\simeq \left| J_{-1}\left(-p_C \frac{E_0}{\omega_0^2}\right) J_1\left(-\frac{E_0^2}{8\omega_0^3}\right) + J_1\left(-p_C \frac{E_0}{\omega_0^2}\right) J_0\left(-\frac{E_0^2}{8\omega_0^3}\right) \right|^2 \frac{1}{\sqrt{1+\frac{\tau_{XUV}^2}{\tau_{IR}^2}}} \end{aligned} \tag{2.2.24}$$

The same can be said for SB^{2+}, for which $n+2m=2$ and the most relevant (n,m) couples are (-2,2), (0,1) and (2,0):

$$\begin{aligned} SB_0^{++} &= \left| \sum_{\substack{n=-\infty \\ n+2m=2}}^{+\infty} \mathcal{J}_n(u,v) \right|^2 \frac{1}{\sqrt{1+2\frac{\tau_{XUV}^2}{\tau_{IR}^2}}} \simeq \\ &\simeq \left| J_{-2}(u)J_2(v) + J_0(u)J_1(v) + J_2(u)J_0(v) \right|^2 \frac{1}{\sqrt{1+2\frac{\tau_{XUV}^2}{\tau_{IR}^2}}} \end{aligned} \tag{2.2.25}$$

In general we could say that $n+2m=N$, where N is the order of the chosen sideband ($N<0$ for negative sidebands).

This result could have also been obtained through another method (explored in [29] as well). Let us consider Eq. (2.1.12): the resulting time-dependent Schrödinger equation will be

$$i\frac{\partial\,|\psi(\mathbf{r},t)\rangle}{\partial t} = \left[\frac{\hat{\mathbf{p}}^{\mathbf{2}}}{2} + \hat{\mathbf{p}}\cdot\mathbf{A_{IR}}(t) + \frac{A_{IR}^2(t)}{2}\right]|\psi(\mathbf{r},t)\rangle \tag{2.2.26}$$

With no coupling terms its solution would be a simple plane wave; instead, now our solution takes the form of a *Volkov wave* (or Volkov state). The shape of a generic Volkov wave is

$$|\Psi_v(t)\rangle = |\tilde{\mathbf{p}}\rangle\, e^{-iS(t,t')} \tag{2.2.27}$$

which is basically a plane wave multiplied with the complex exponential of the semi-classical action $S(t,t') = \displaystyle\int_{t'}^{t}\frac{1}{2}\Big(\mathbf{p}+\mathbf{A_{IR}}(t'')\Big)^2 dt''$. In fact, our solution looks like

$$\psi_V(\mathbf{r},t) = \frac{1}{(2\pi)^{3/2}}e^{i\mathbf{p}\cdot\mathbf{r}}e^{-i\int_{t'}^{t}\left(\frac{p^2}{2}+\mathbf{p}\cdot\mathbf{A_{IR}}(t'')+\frac{A_{IR}^2(t'')}{2}\right)dt''} \tag{2.2.28}$$

where the presence of both the plane wave and the semi-classical action is evident.

The integral in the exponential can be calculated to obtain

$$\psi_V(\mathbf{r},t) = \frac{1}{(2\pi)^{3/2}}e^{i\mathbf{p}\cdot\mathbf{r}}e^{-i\mathbf{p}\cdot\frac{\mathbf{A_0(t)}}{\omega_0}\sin(\omega_0 t)-i\frac{A_0^2(t)}{8\omega_0}\sin(2\omega_0 t)}e^{-i\left(\frac{p^2}{2}+\frac{A_0^2}{4}\right)t} \tag{2.2.29}$$

This wave function looks quite familiar: it is in fact explicitly written in the form stated by the Floquet theorem $|\psi(t)\rangle = |\phi(t)\rangle\, e^{-i\epsilon t}$, where we observe that the Floquet quasi-energy is represented by $\epsilon = \frac{p^2}{2}+\frac{A_0^2}{4}$, and the rest of the function is periodic in T (the first exponential is the plane wave and therefore does not depend on time, whereas the second exponential depends on $\sin(\omega_0 t)$ and on $\sin(2\omega_0 t)$, which are both T-periodic functions). This way we have simply shown another way of seeing the relation between our model and Floquet theory.

From here we can use the property of generalised Bessel functions [40] according to which

$$e^{i\left(u\sin(\vartheta)+v\sin(2\vartheta)\right)} = \sum_{n=-\infty}^{+\infty}\mathcal{J}_n(u,v)e^{in\vartheta} \tag{2.2.30}$$

so that we are able to write

$$\psi_V(\mathbf{r},t) = \frac{1}{2\pi^{3/2}} e^{i\mathbf{p}\cdot\mathbf{r}} \sum_{n=-\infty}^{+\infty} \mathcal{J}_n\left(\mathbf{p}\cdot\frac{\mathbf{A_0}(t)}{\omega_0}, \frac{A_0^2}{8\omega_0}\right) e^{-i\left(\frac{p^2}{2}+\frac{A_0^2}{4}+n\omega_0\right)t} \tag{2.2.31}$$

which after CMA and a couple of calculations allows to obtain the exact same results of Eq. (2.2.24) and Eq. (2.2.25).

If we now try to plot this behaviour as we did in the previous sections we find the following:

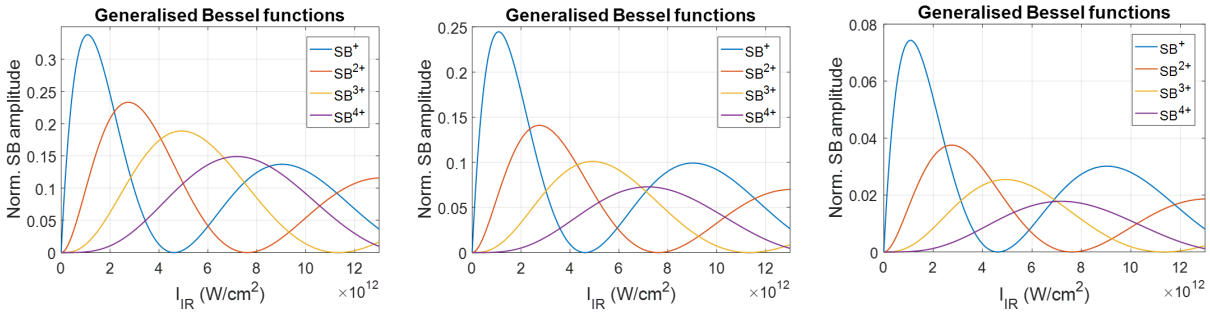

(a) $\tau_{IR} = 50$ fs, $\tau_{XUV} = 11$ fs. (b) $\tau_{IR} = 11$ fs, $\tau_{XUV} = 11$ fs. (c) $\tau_{IR} = 11$ fs, $\tau_{XUV} = 50$ fs.

Figure 2.8: Generalised Bessel functions for positive sidebands spanning from the first to the fourth order.

Little to no changes seem to have occurred in the shape of the functions, aside from the difference in height of the various peaks depending on the ratio between the squared duration of the pulses (Figure 2.8). Although, if we take a closer look and compare this graph with that of the non-adiabatic case, we observe how a variation is actually present. This deviation is nearly null for an $I_{IR} < 10^{13}\frac{W}{cm^2}$, while it increases of a relevant amount once the intensity grows, as demonstrated in Figure 2.9.

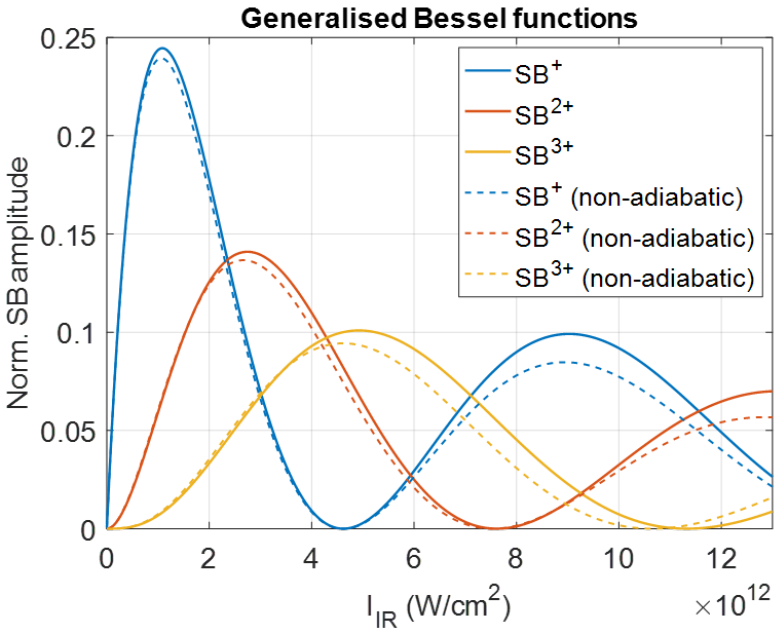

Figure 2.9: Comparison between generalised Bessel expansion and non-adiabatic expansion at different IR and XUV duration.

Let us now consider what happens by halting the expansion of the generalised Bessel function at different terms, to demonstrate that our approximations in Eq.s (2.2.24) and (2.2.25) were valid.

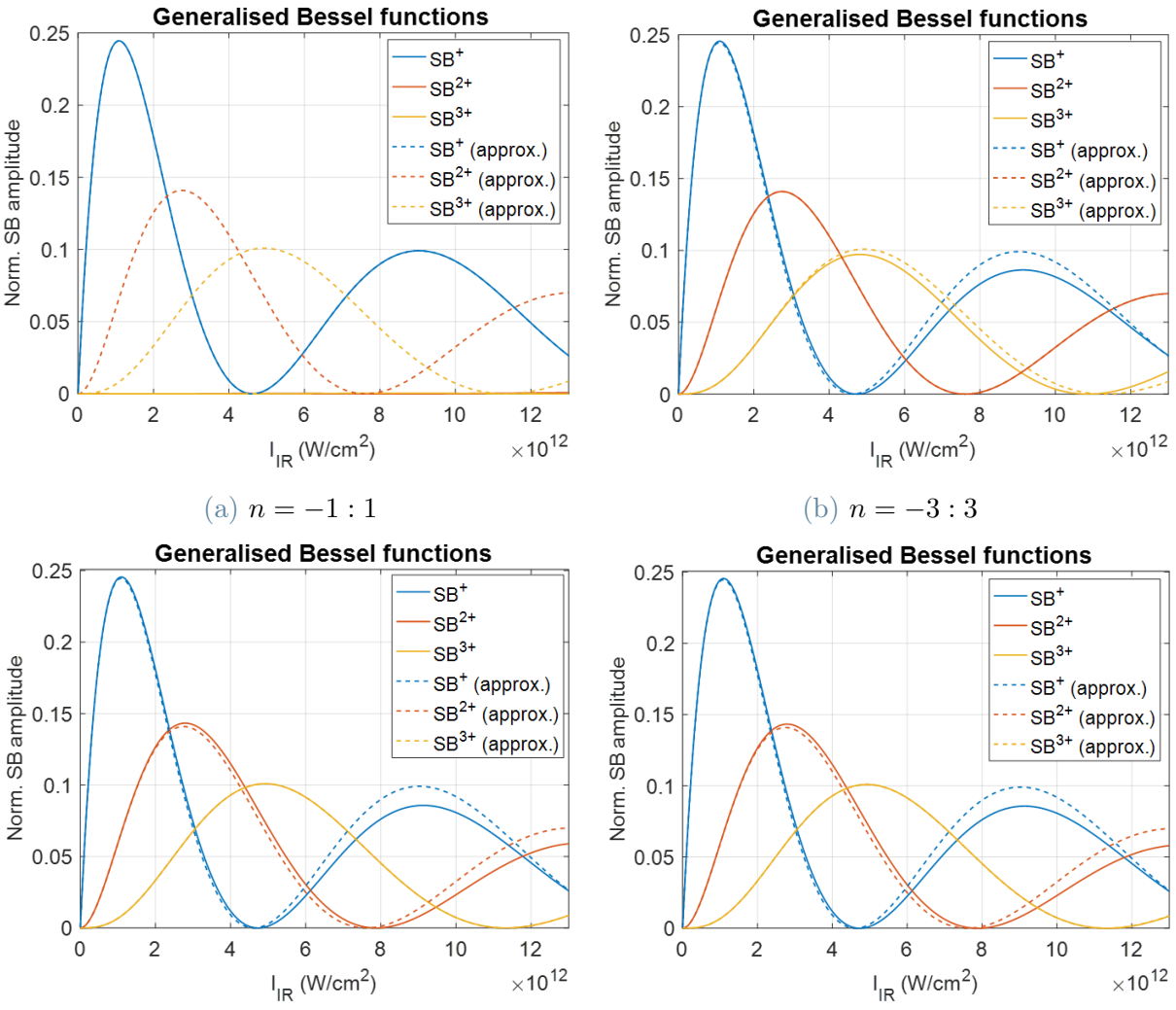

(a) $n = -1 : 1$ (b) $n = -3 : 3$

(c) $n = -5 : 5$ (d) $n = -200 : 200$

Figure 2.10: Generalised Bessel expansion halted at different values of n.

In Figure 2.10a we can see what happens if we truncate the summation after just two terms. For the first (positive) sideband this is equivalent to the approximation in Eq. (2.2.24), while for the second and third ones we have way less elements than needed to form a reliable curve. Instead, in Figure 2.10b we notice how SB^{+} deviates from its approximation. SB^{2+} is exactly on its approximation, while SB^{3+} begins to assume a more accurate shape. By moving on to Figure 2.10c we notice hardly any difference in SB^{+} and a small deviation on SB^{2+} and on SB^{3+} akin to that of the previous figure for the first sideband. Finally, if we look at the last figure, Figure 2.10d, we see that nearly no difference is present with the previous plot, thus we may confound those curves with actual generalised Bessel functions.

Therefore, truncating to fewer terms leads to a negligible error, especially if we consider

that our experiment is going to take place in a smaller range of intensities than what is shown in the previous figures. Namely, we are going to perform experiments up to an IR intensity of $I_{IR} = 2 \cdot 10^{12}$, where we have an acceptable margin of error, as we can observe from Figure 2.11.

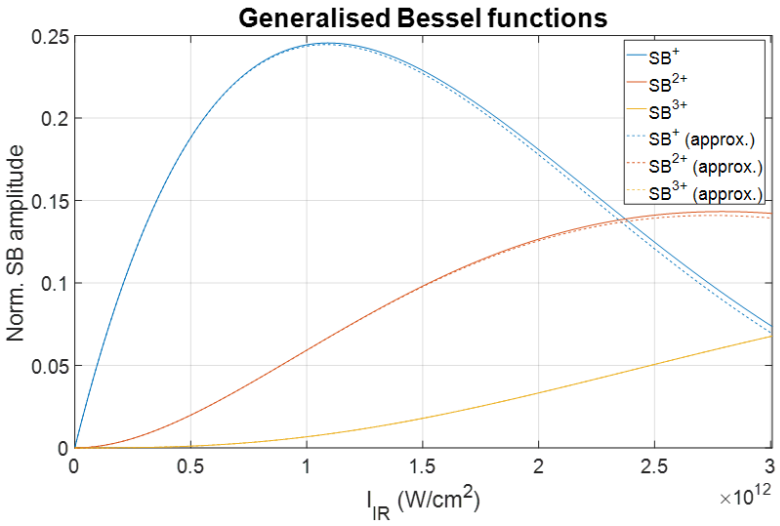

Figure 2.11: Generalised Bessel functions and their approximations for the first three positive sidebands within the experimental range.

Up to this moment we have analysed positive sidebands exclusively. If we consider the negative sidebands as well, we find a result which at first glance may be unexpected: while the peak of negative sidebands is shifted with respect to that of positive ones, as we already anticipated from the simple Bessel model for monochromatic beams, they possess a lower amplitude too. What is the reason behind this behaviour? In order to understand this, we can study an example.

Let us employ the previous approximation of

$$SB_0^+ \simeq |J_{-1}(u)J_1(v) + J_1(u)J_0(v)|^2 \doteq |A + B|^2$$

and the similar truncation for its negative counterpart

$$SB_0^- \simeq |J_1(u)J_{-1}(v) + J_{-1}(u)J_0(v)|^2 \doteq |A' + B'|^2$$

and remember the property of Bessel functions for odd[11] values of n

[11] Instead, for even values we have $J_n(z) = J_{-n}(z)$.

$$J_n(z) = -J_{-n}(z) \tag{2.2.32}$$

As a consequence, we can analyse how the terms A and A', and the terms B and B' relate to one another. If we start from A and A', by applying Eq. (2.2.32) we are able to calculate the following:

$$A' = J_1(u)J_{-1}(v) = [-J_1(u)] \cdot [-J_{-1}(v)] = J_{-1}(u)J_1(v) = A$$

On the other hand, B and B' behave as indicated below:

$$B' = J_{-1}(u)J_0(v) = [-J_1(u)] \cdot J_0(v) = -J_1(u)J_0(v) = -B$$

Hence, we have that $A' = A$ and $B' = -B$, which implies that we can rewrite our sidebands amplitude as

$$SB_0^+ \simeq |A + B|^2$$
$$SB_0^- \simeq |A - B|^2$$

where it is easy to notice the difference between the two, and also why the peaks of SB^- are at lower intensities[12] than those of SB^+.

[12]By analysing the parity of Bessel functions we are able to notice that both A and B have a negative first peak around similar values of intensity, so an addition of the B term actually corresponds to an increase in absolute value of the first peak. Naturally, the opposite happens if we subtract B. Therefore, in terms of the amplitude of the first peak we have $\mathrm{SB}^+ > \mathrm{SB}^-$. The same happens for later peaks.

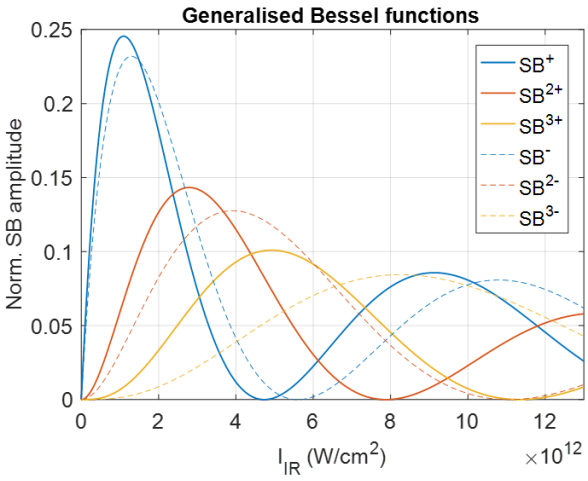

Figure 2.12: Generalised Bessel functions for the first three positive (solid lines) and negative (dashed lines) sidebands.

If we now return to analysing the dependence of the sidebands amplitude on the IR duration, what we observe is the following:

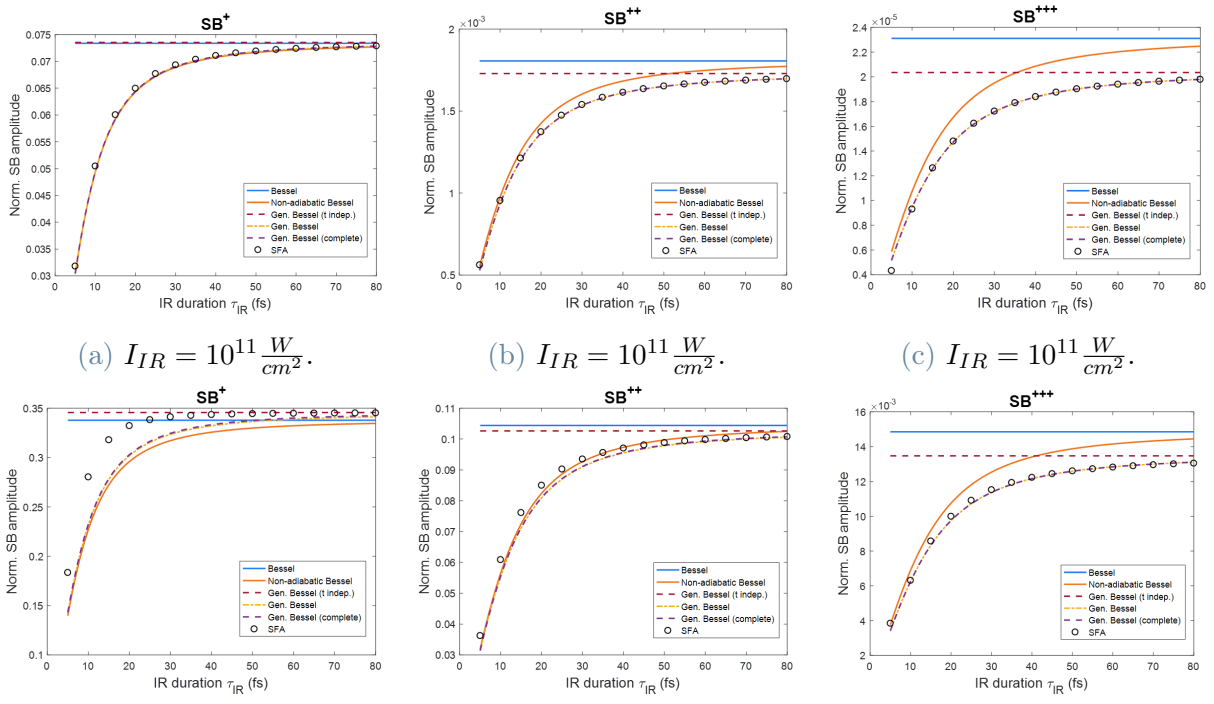

(a) $I_{IR} = 10^{11} \frac{W}{cm^2}$. (b) $I_{IR} = 10^{11} \frac{W}{cm^2}$. (c) $I_{IR} = 10^{11} \frac{W}{cm^2}$.

(d) $I_{IR} = 10^{12} \frac{W}{cm^2}$. (e) $I_{IR} = 10^{12} \frac{W}{cm^2}$. (f) $I_{IR} = 10^{12} \frac{W}{cm^2}$.

Figure 2.13: Dependence of the amplitude of SB$^+$, SB^{++} and SB^{+++} on τ_{IR}. In these graphs the following models are compared: the time-independent Bessel, the non-adiabatic Bessel, the time-independent generalised Bessel, the truncated generalised Bessel, the complete generalised Bessel, and the SFA model. Here, $\tau_{XUV} = 11$ fs.

The first detail is that now the asymptotic value reached by the curve is no longer the same which we had with the simple Bessel functions; the addition of the quadratic term has in fact moved the limit for long duration pulses. This difference gains a higher relevance the more we increase the IR intensity, and the higher is the order of the sideband we are considering.

Then, it is clear that truncating the generalised Bessel functions at higher orders (in this instance at $n = 200$) does not yield a significant improvement with respect to the approximation we made in Eq. (2.2.24) and in Eq. (2.2.25), hence we are justified to use the latter instead of the former.

A further point can be made about the comparison between the three time-dependent models we used (i.e. SFA, non-adiabatic Bessel and generalised Bessel). Concerning the first sideband, the three models are superimposed up to an intensity of $I_{IR} \simeq 10^{11} \frac{W}{cm^2}$. After that, while the non-adiabatic Bessel functions and the generalised Bessel curves are still roughly superimposed, the deviation from the SFA model is definitely non-negligible. This may be attributed to the approximation performed in Eq. (2.2.10). As we can see from Figure 2.14c, this approximation becomes weaker right after an intensity of $I_{IR} \sim 2 \cdot 10^{11} \frac{W}{cm^2}$, where the difference between the exact value of $|J_1|^2$ and its approximation begins to manifest. On the other hand, if we look at the temporal profile of the function in Figure 2.14a, we begin to see a splitting of the main peak at $I_{IR} > 10^{12} \frac{W}{cm^2}$, which is not present in Figure 2.14b due to the Gaussian nature of the approximation. After this point we can no longer employ the approximation of Eq. (2.2.10) to find an analytical solution and we require numerical calculations.

Instead, by analysing the second and third positive sidebands it is possible to notice how a difference is immediately present. Indeed, the SFA simulations lie onto the generalised Bessel curves instead of the non-adiabatic Bessel model, which are visibly distinct one from the other. Even at higher intensities ($I_{IR} \simeq 10^{12} \frac{W}{cm^2}$) the accord appears to be reliable enough.

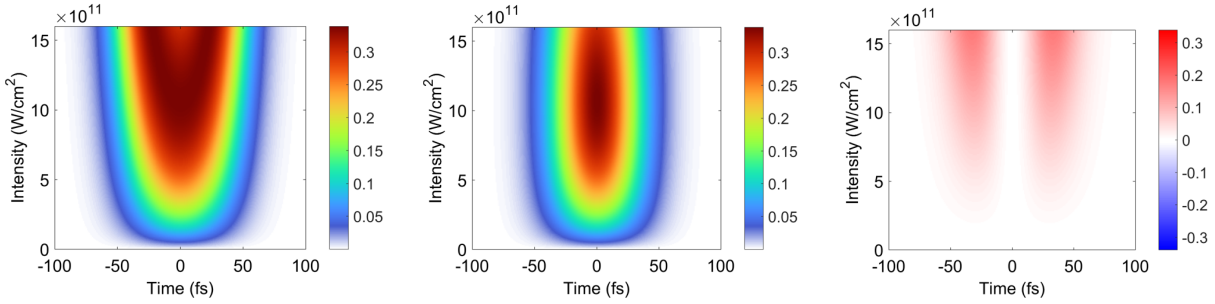

Figure 2.14: (a) exact value of $|J_1|^2$; (b) approximation of Eq. (2.2.10); (c) difference between the two.

2.3. Effects of dispersion

As we already mentioned in Chapter 1.2, the generated sidebands may not have the shape displayed in previous simulations (see Figure 1.17). In fact, they are likely to be distorted by *dispersion*.

Before introducing the effects of both non-linear and linear dispersion (also referred to as *chirp*), it is of fundamental importance to fully understand what they are from a theoretical standpoint.

Let us begin by considering a simple, non-monochromatic electric field $E(t)$ having a central frequency of ω_0. We wish to isolate a few frequency around $\bar{\omega}$, another frequency comprised in the wave packet which is far enough from ω_0. Our objective now is trying to understand when this frequency will arrive.

If we take into account a small range of frequencies around $\bar{\omega}$, namely the range $\bar{\omega} - \Delta\omega < \omega < \bar{\omega} + \Delta\omega$, we can write:

$$E_{\bar{\omega}}(t) = \frac{1}{2\pi} \int_{\bar{\omega}-\Delta\omega}^{\bar{\omega}+\Delta\omega} \left|\tilde{E}(\omega)\right| e^{i\phi(\omega)} e^{i\omega t} d\omega \tag{2.3.1}$$

where we indicated as $\tilde{E}(\omega)$ the Fourier transform of $E(t)$ and we wrote it as the product of its modulus and phase $\phi(\omega)$.

We can then make an expansion of our phase $\phi(\omega)$ centred around $\bar{\omega}$, thus obtaining

$$\phi(\omega) = \phi(\bar{\omega}) + \left.\frac{\mathrm{d}\phi}{\mathrm{d}\omega}\right|_{\bar{\omega}} (\omega - \bar{\omega}) + \ldots \tag{2.3.2}$$

For the moment we shall stop at the first order expansion. Therefore, our $E(t)$ field will become:

$$\begin{aligned} E_{\bar{\omega}}(t) &= \frac{1}{2\pi}\int_{\bar{\omega}-\Delta\omega}^{\bar{\omega}+\Delta\omega} \left|\tilde{E}(\omega)\right| e^{-i[\phi(\bar{\omega})+\frac{\mathrm{d}\phi}{\mathrm{d}\omega}\big|_{\bar{\omega}}(\omega-\bar{\omega})]} e^{i\omega t} d\omega = \\ &= \frac{1}{2\pi}\int_{\bar{\omega}-\Delta\omega}^{\bar{\omega}+\Delta\omega} \left|\tilde{E}(\omega)\right| e^{-i\phi(\bar{\omega})} e^{-i\frac{\mathrm{d}\phi}{\mathrm{d}\omega}\big|_{\bar{\omega}}\omega} e^{i\frac{\mathrm{d}\phi}{\mathrm{d}\omega}\big|_{\bar{\omega}}\bar{\omega})} e^{i(\omega t-\bar{\omega}t)} e^{i\bar{\omega}t} d\omega = \\ &= \frac{1}{2\pi} e^{i[\bar{\omega}t-\phi(\bar{\omega})]} \int_{\bar{\omega}-\Delta\omega}^{\bar{\omega}+\Delta\omega} \left|\tilde{E}(\omega)\right| e^{i(\omega-\bar{\omega})[t-\frac{\mathrm{d}\phi}{\mathrm{d}\omega}\big|_{\bar{\omega}}]} d\omega \end{aligned} \tag{2.3.3}$$

We immediately notice that we have the maximum for $E(t)$ when $t - \frac{\mathrm{d}\phi}{\mathrm{d}\omega}\big|_{\bar{\omega}} = 0$, that is when t is equal to the so-called *group delay* $\tau_g(\bar{\omega})$. Hence, $\tau_g(\bar{\omega}) = \frac{\mathrm{d}\phi}{\mathrm{d}\omega}\big|_{\bar{\omega}}$.

If we now wish to extend the previous reasoning to the whole pulse, we can perform the same expansion of $\phi(\omega)$ around the central frequency ω_0 instead. Therefore,

$$\phi(\omega) = \phi(\omega_0) + \left.\frac{\mathrm{d}\phi}{\mathrm{d}\omega}\right|_{\omega_0}(\omega-\omega_0) + \frac{1}{2}\left.\frac{\mathrm{d}^2\phi}{\mathrm{d}\omega^2}\right|_{\omega_0}(\omega-\omega_0)^2 + \frac{1}{6}\left.\frac{\mathrm{d}^3\phi}{\mathrm{d}\omega^3}\right|_{\omega_0}(\omega-\omega_0)^3 + ... \tag{2.3.4}$$

From this we gather that the final group delay calculated for a generic frequency ω must be:

$$\begin{aligned} \tau_g(\omega) = \frac{\mathrm{d}\phi}{\mathrm{d}\omega} &= \left.\frac{\mathrm{d}\phi}{\mathrm{d}\omega}\right|_{\omega_0} + \left.\frac{\mathrm{d}^2\phi}{\mathrm{d}\omega^2}\right|_{\omega_0}(\omega-\omega_0) + \frac{1}{2}\left.\frac{\mathrm{d}^3\phi}{\mathrm{d}\omega^3}\right|_{\omega_0}(\omega-\omega_0)^2 + \frac{1}{6}\left.\frac{\mathrm{d}^4\phi}{\mathrm{d}\omega^4}\right|_{\omega_0}(\omega-\omega_0)^3 + ... = \\ &= \tau_g(\omega_0) + D_2(\omega-\omega_0) + \frac{1}{2}D_3(\omega-\omega_0)^2 + \frac{1}{6}D_4(\omega-\omega_0)^3 + ... \\ &= \tau_g(\omega_0) + GDD(\omega-\omega_0) + \frac{1}{2}TOD(\omega-\omega_0)^2 + \frac{1}{6}FOD(\omega-\omega_0)^3 + ... \end{aligned} \tag{2.3.5}$$

In Eq. (2.3.5) we have defined a few critical quantities, which are the focus of this discussion, and indicate the dispersion of the pulse. While $\tau_g(\omega_0)$ is a constant term and can generally be disregarded, we have that the others are pivotal in the discussion on the phase, being multiplied by the frequency itself and therefore leading to a value which is

not invariable.

The first important term we encounter is D_2, or GDD, and it is the *second order dispersion*, or *group delay dispersion*. It represents the *linear chirp*, which we also hinted at in Chapter 1.1.4. D_3, or TOD, is the *third order dispersion*, and it gives a parabolic contribution, while D_4, or FOD, is the *fourth order dispersion*, which resembles a cubic function, and they will be followed by the fifth order, the sixth order, and so on. These represent the *non-linear dispersion*. We will limit to consider up to the fourth order, since above the fifth order the influence of those terms can be deemed trivial in our discussion.

Let us transpose these terms into our model. For an easier visualisation of these concepts we will employ simulations performed through the STRIPE algorithm. In our case, we will be able to decompose the phase terms $\phi_{IR}(\omega)$ and $\phi_{XUV}(\omega)$ of Eq. (2.1.42) as we did in Eq. (2.3.4). This will result in a phase that may be written as:

$$\begin{aligned}\phi_{IR}(\omega) &= \frac{1}{2}GDD_{IR}(\omega-\omega_0)^2 + \frac{1}{6}TOD_{IR}(\omega-\omega_0)^3 + \frac{1}{24}FOD_{IR}(\omega-\omega_0)^4 \\ \phi_{XUV}(\omega) &= \frac{1}{2}GDD_{XUV}(\omega-\omega_0)^2 + \frac{1}{6}TOD_{XUV}(\omega-\omega_0)^3 + \frac{1}{24}FOD_{XUV}(\omega-\omega_0)^4\end{aligned} \tag{2.3.6}$$

bringing us to the following spectrograms:

$$\begin{aligned}S_{IR}(\omega) &= S_{0,IR}(\omega)\cdot e^{-i[\frac{1}{2}GDD_{IR}(\omega-\omega_0)^2+\frac{1}{6}TOD_{IR}(\omega-\omega_0)^3+\frac{1}{24}FOD_{IR}(\omega-\omega_0)^4]} \\ S_{XUV}(\omega) &= S_{0,XUV}(\omega)\cdot e^{-i[\frac{1}{2}GDD_{XUV}(\omega-\omega_0)^2+\frac{1}{6}TOD_{XUV}(\omega-\omega_0)^3+\frac{1}{24}FOD_{XUV}(\omega-\omega_0)^4]}\end{aligned} \tag{2.3.7}$$

We can observe how the constant and linear terms have been neglected. This is due to the fact that their derivative results in a null and constant contribution respectively, and we do not mind for a constant delay of all frequencies.

Now we can start analysing the effects of the the single components of the phase. Let us go in order, from lower to higher order dispersion, to then see a few examples of mixed terms.

- **TL pulses:**
  We begin by considering transform limited (TL) pulses. This implies that all the previous terms, both pertaining to the IR phase and to the XUV phase, are set to

zero. We only have the terms $\tau_g(\omega_0)$ and $\tau_g(\omega_x)$ for the IR and XUV respectively, which (as already mentioned) we will not consider. This makes for an intuitive picture which is akin to that of Figure 1.15: firstly, the XUV pulses ionise the gas, and subsequently the IR beam hits the photoelectrons, causing stimulated emission or absorption, thus generating the sidebands. Here is an example of simulation with no dispersion, accompanied by the respective schematic sidebands plot:

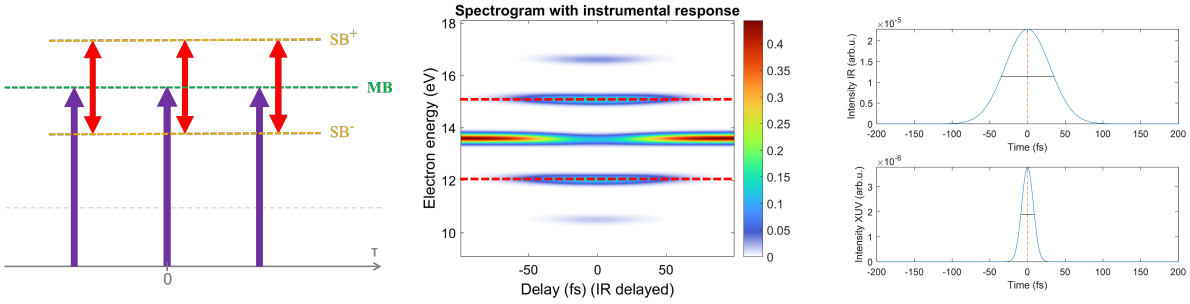

(a) (b) (c)

Figure 2.15: In Figure 2.15a we can see a straightforward scheme of the ionisation of the Ne atoms. If no chirp is present, the sidebands are always centered around the same values. Only two sidebands were plotted, for simplicity. In Figure 2.15b we see the SHS spectrogram, which indeed possesses straight sidebands at the expected values. It was obtained with an intensity of $I_{IR} = 8 \cdot 10^{11} \frac{W}{cm^2}$. In Figure 2.15c, the generating pulses.

- **GDD_{IR}-only pulses:**
  Now we consider a spectrogram which is affected exclusively by the second order dispersion of the IR pulse. As previously mentioned, since D_2 represents the *linear* chirp, it must have a *linear* effect on the sidebands of the spectrogram. Indeed, what happens in case of an IR beam affected only by GDD is that the frequency of the IR pulse increases (*up-chirp*) or decreases (*down-chirp*) linearly with time, therefore varying its energy in time too (Figure 2.16). Hence, with an XUV pulse whose energy is constant and a time-varying IR pulse, we will have diverging or converging sidebands.

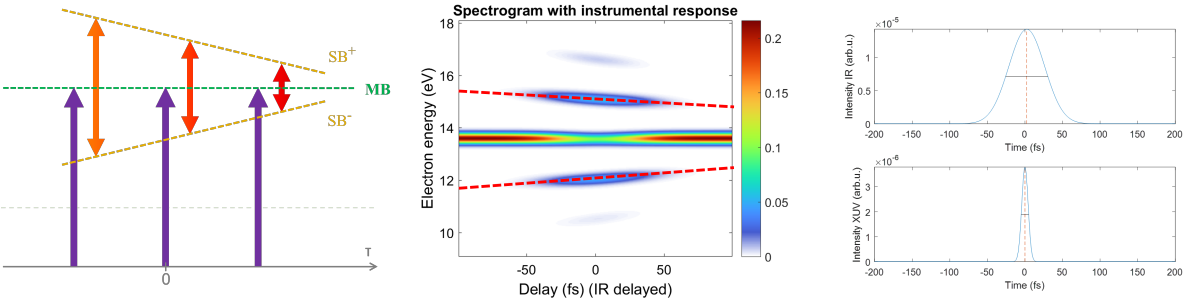

(a) (b) (c)

Figure 2.16: Case of a linearly chirped IR pulse (up-chirp) after ionisation by a TL XUV pulse. The XUV beam ionises photoelectrons to the same energy, while the chirped IR pulses hit ionised photoelectrons with different energies depending on the delay τ. Since higher frequencies in this case are faster, we will have higher energies at negative delays and while lower frequencies for $\tau > 0$, resulting in converging sidebands. The opposite happens in case of down-chirp, and the sidebands are diverging. Note that in this instance the probe is delayed, differently from the previously used formulas (with a delayed XUV the result is similar to the one shown for the down-chirp, instead). This behaviour is confirmed by Figure 2.16b, in which a $GDD_{IR} = -250$ fs^2 and an intensity $I_{IR} = 5 \cdot 10^{11} \frac{W}{cm^2}$ were used. The third picture represents the employed pulses. We notice how their shape is still Gaussian, since the linear chirp depends on the square of the frequency.

- **GDD$_{\mathbf{XUV}}$-only pulses:**
  Let us consider the case in which only the XUV pulses are affected by group delay dispersion. At first glance, it may appear similar to the previous one, yet it yields a different result. We foresee that having another linear chirp will imply again some kind of tilt of the sidebands, except now it is the XUV beam to possess different energies and ionise photoelectrons differently. Then, no matter the delay τ, the IR radiation is going to affect the particles with the same quantity of energy. So, the distance between main band and sidebands will be the same for every delay, but this time the main band will be at different energies depending on τ, therefore being tilted, together with its sidebands.

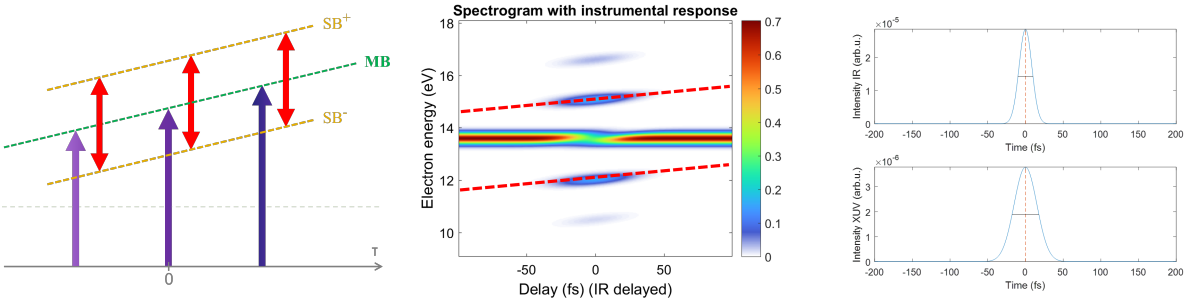

(a) (b) (c)

Figure 2.17: Simulated spectrogram with linear up-chirp on the XUV pulse. The sidebands result parallel and tilted upwards, instead of being converging or diverging. The sidebands are tilted downwards in case of down-chirp. In this figure a $GDD_{XUV} = 100$ fs^2 and an $I_{IR} = 10^{12} \frac{W}{cm^2}$ were employed.

- **GDD$_{\mathbf{IR}}$-only and GDD$_{\mathbf{XUV}}$-only pulses:**
  Now that we have seen the effects of chirp in both IR and XUV taken individually, we can see a few examples of what happens if we have both pulses with a non-zero GDD. What we expect is certainly a tilt in the sidebands, and we can imagine this tilt will vary from SB^+ to SB^-.

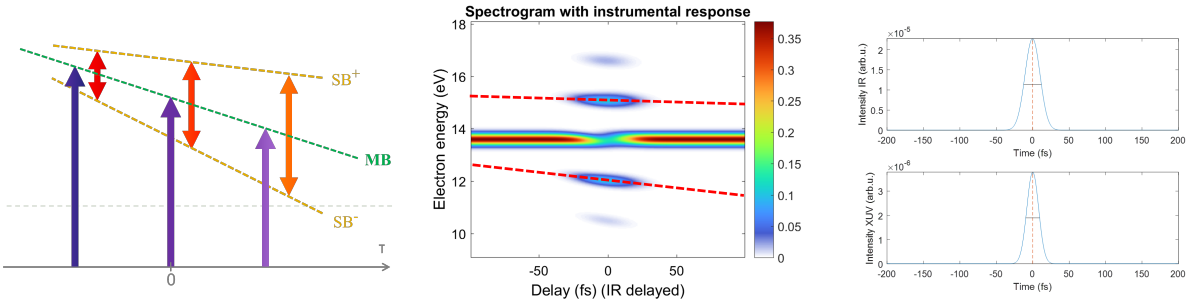

(a) (b) (c)

Figure 2.18: Case of both IR and XUV pulses affected by down-chirp. Here, $GDD_{IR} = -100$ fs^2, $GDD_{XUV} = -50$ fs^2 and $I_{IR} = 8 \cdot 10^{11} \frac{W}{cm^2}$.

- **TOD$_{\mathbf{IR}}$-only pulses:**
  From this point on, the dispersion we are going to analyse will no longer be linear. This is the reason why we are not able to represent in a clear and simple way as in Figure 2.15a, Figure 2.16a or Figure 2.17a the energy of our photoelectrons and the shape of the sidebands. Now we will analyse the case of a TL XUV pulse and an IR pulse with third order dispersion (TOD). By inspecting the shape of the sidebands,

we are able to discern a parabolic form. This is given by the fact that our TOD term in the derivative of the phase is actually proportional to ω^2.

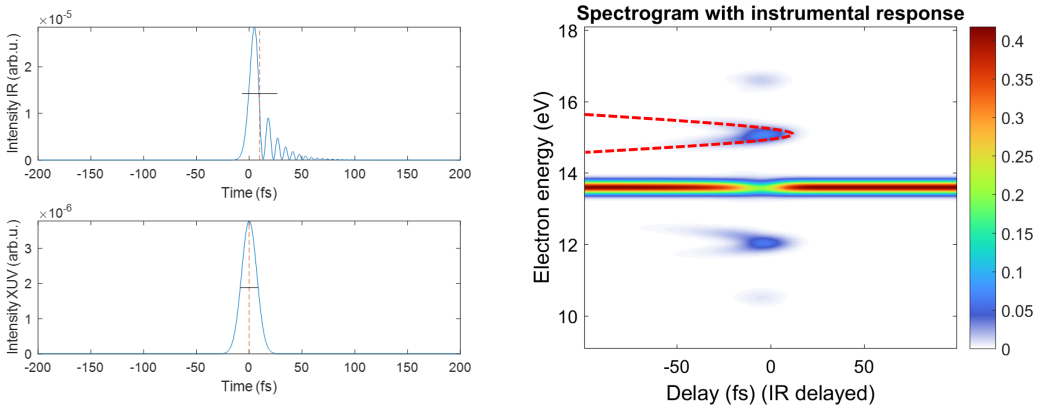

(a) (b)

Figure 2.19: In the case of $TOD_{IR} \neq 0$, the IR pulse is no longer Gaussian: it possesses a main peak with a steeper side, after which lower, decreasing peaks are collocated. This allows the formation of the aforementioned parabolic shape, visible in Figure 2.19b. Changing the sign of the TOD would vary the concavity of the parabola. This spectrogram is also symmetric with respect to the main band. In this figure only one sideband is marked with the red dashed line to better appreciate the parabolic shape. The values used for this simulation are $TOD_{IR} = 350$ fs^3 and $I_{IR} = 10^{12} \frac{W}{cm^2}$.

- **TOD_{XUV}-only pulses:**
  In the linear chirp case, when we switched from a non-null GDD_{IR} to a GDD_{XUV} different from zero our simulations changed visibly. On the other hand, altering the current hypothesis from $TOD_{IR} \neq 0$ to $TOD_{XUV} \neq 0$ does not have a substantial impact on the overall shape of the sidebands. The only difference this time is the position of the vertex of the parabola. With a positive TOD_{IR} (as in Figure 2.19) the vertex could be found for an IR delay $\tau > 0$, and conversely for a negative dispersion. In our case of a non-null TOD_{XUV} the opposite happens: in case of positive dispersion the vertex is at negative delays and vice versa. Having this kind of parallelism makes so that it is impossible to distinguish a negatively chirped XUV from a positively chirped IR (or vice versa) from the SHS spectrogram alone.

- **TOD_{IR}-only and TOD_{XUV}-only pulses:**
  Given the previous two points, what happens if we have a combination of both TOD_{IR} and TOD_{XUV}? Naturally, it depends on the amount of third order dispersion present in each type of pulse and on its sign. Since the sidebands have

a mirrored behaviour, With an opposite dispersion we expect them to sum up to obtain a similar shape as the one we started with. However, if the two signs of the dispersion are equal, their value is more or less the same, and the duration of the pulses is comparable, we can watch how the overall TOD changes form. The "tails" from the parabolic shape are now visible on both sides, rendering the sidebands almost symmetrical around $\tau = 0$. Also, due to this symmetry the case of both positively chirped pulses is almost indistinguishable from the case of both negatively chirped pulses.

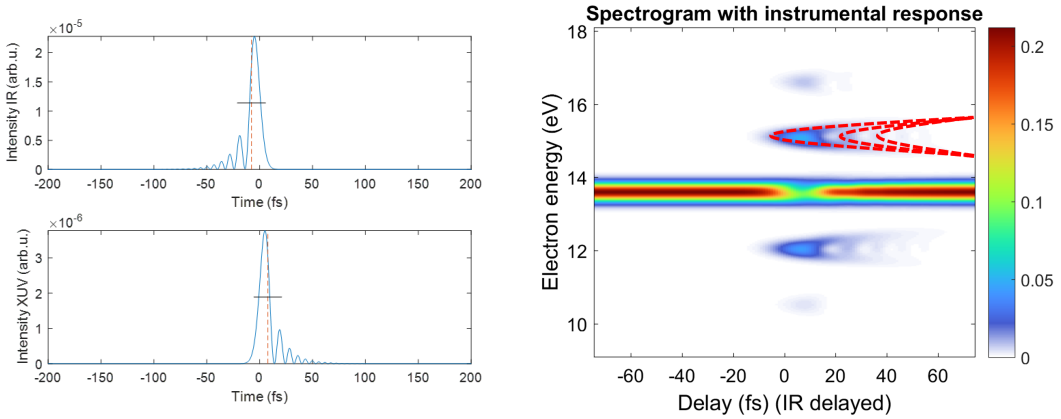

(a) (b)

Figure 2.20: IR and XUV beams with opposite TOD. In this case the pulses have a comparable duration, causing interference. The lower peaks will behave like pulses themselves and create many smaller parabolic figures. In this instance $TOD_{IR} = 400$ fs^3, $TOD_{XUV} = -400$ fs^3 and $I_{IR} = 10^{12} \frac{W}{cm^2}$.

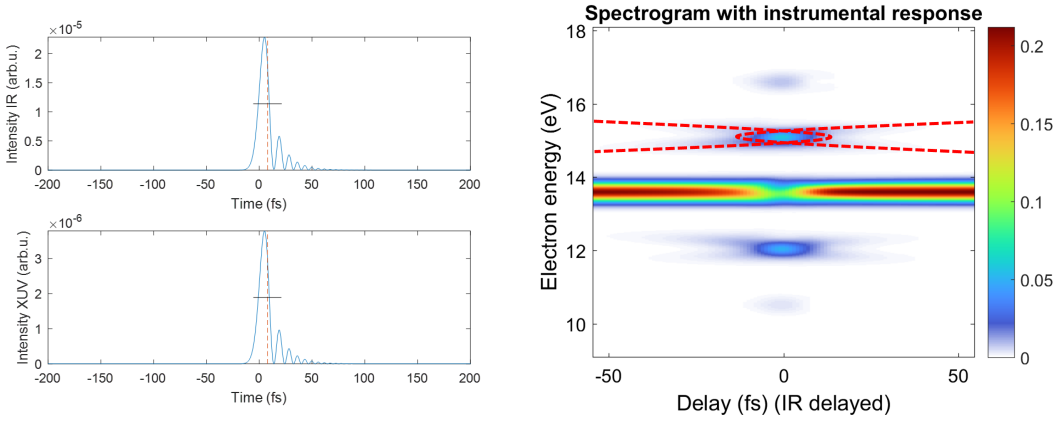

(a) (b)

Figure 2.21: In this picture we have both positive third order dispersions. We notice how this "cross-shaped" spectrogram is actually the superposition of two parabolic curves with vertices on opposite sides of $\tau = 0$. In this case we have $TOD_{IR} = TOD_{XUV} = 400$ fs^3 and $I_{IR} = 8 \cdot 10^{11} \frac{W}{cm^2}$.

- **FOD$_{IR}$-only pulses:**
  As we might expect having in mind the previous points, the fourth order dispersion (FOD) for the IR pulse will lead to a sideband which is shaped like a cubic function. This is of course given by the dependence of $\tau_g(\omega)$ on the third power of ω. D_4 is in fact multiplied by $(\omega - \omega_0)^3$. Furthermore, we notice that these sidebands are symmetric with respect to the main band. Here are a couple of examples of FOD-affected pulses and the resulting spectrograms.

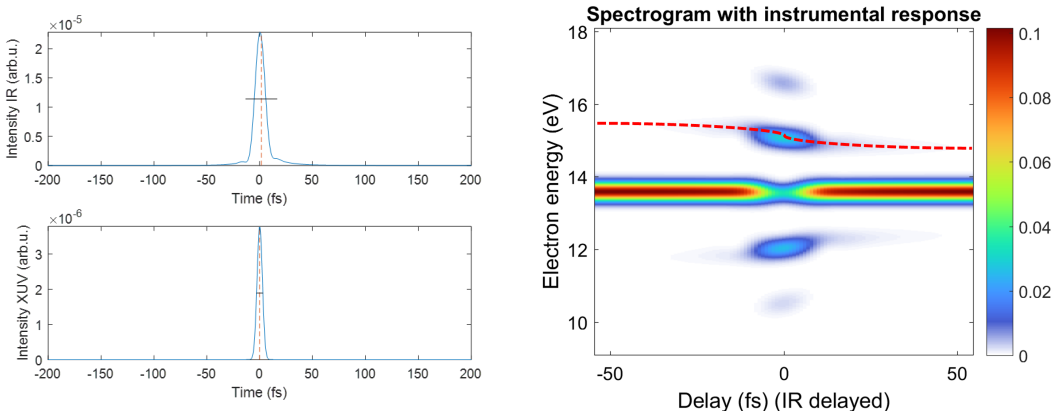

(a) (b)

Figure 2.22: SHS spectrogram generated by a TL XUV pulse and an IR pulse affected by fourth order dispersion. The pulse is nearly symmetrical in time with an almost Gaussian peak, but it also presents two pedestals which prolong its final duration and confer to the spectrogram it characteristic cubic shape, as seen in Figure 2.22b. In this picture, the following factors were used: $FOD_{IR} = 2500$ fs^4, $I_{IR} = 8 \cdot 10^{11} \frac{W}{cm^2}$.

- **FOD$_{XUV}$-only pulses:**
  Since the sidebands assume the shape of an odd function, having the FOD on the IR or on the XUV changes the shape of the spectrogram. In fact, if the fourth order dispersion is on the XUV it breaks the symmetry around the MB (as in case of GDD-only pulses) and we have that the sidebands have the same shape instead of being mirrored.

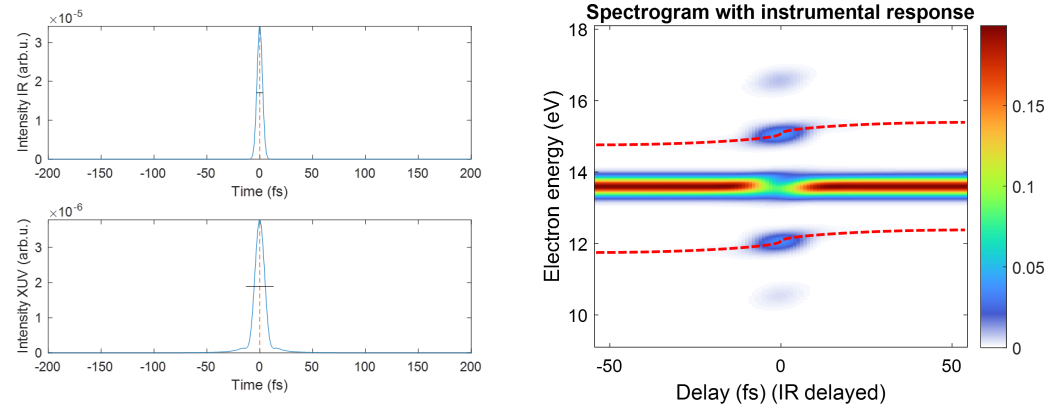

(a) (b)

Figure 2.23: SHS of positive XUV non-linear chirp of the fourth order. In this case $FOD_{XUV} = 2200$ fs^4 and $I_{IR} = 1.2 \cdot 10^{12} \frac{W}{cm^2}$.

- **FOD_{IR}-only and FOD_{XUV}-only pulses:**
  Due to the peculiar kind of symmetry of fourth order dispersion, we expect to always have one of the two sidebands to be the consequence of a "constructive" sum, giving origin to a sideband which looks similar to the previous ones, while the other one results in a sort of "destructive" sum, having a cross-like shape, not unlike those coming from TOD-only pulses. Here is an example:

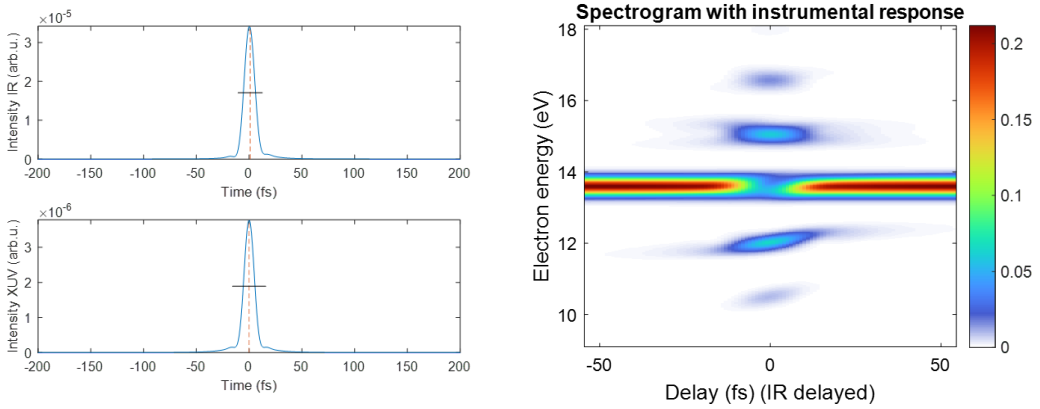

(a) (b)

Figure 2.24: In this picture we can clearly observe a cubic SB^- and a cross-shaped SB^+. This happens when both pulses have same sign dispersion. In this image both signs are positive; if they were negative, the lower sideband would be mirrored around zero delay. With opposite sign dispersion we would have a cubic SB^+ and a cross-shaped SB^-. In the above picture, $FOD_{IR} = 3000$ fs^4, $FOD_{XUV} = 2700$ fs^4 and $I_{IR} = 1.2 \cdot 10^{12} \frac{W}{cm^2}$.

- **Example of pulses with mixed dispersion:**

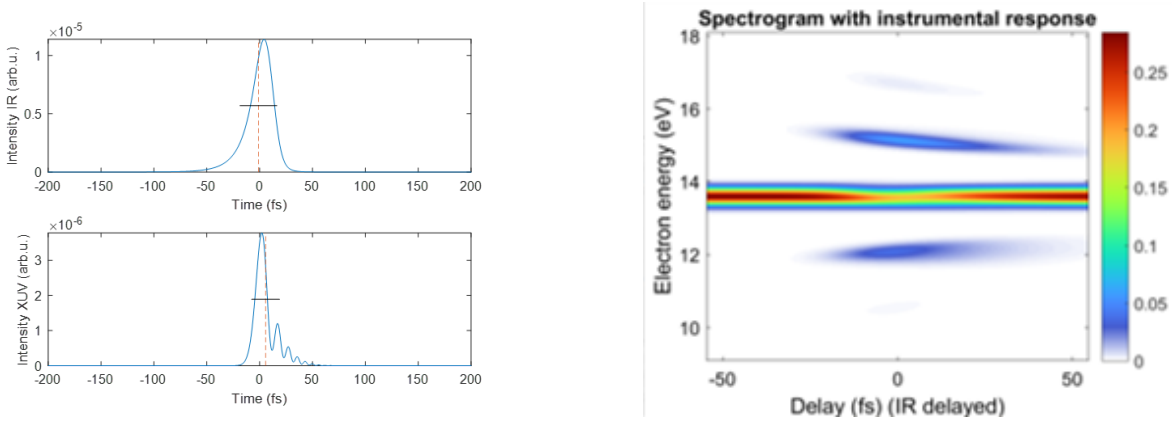

(a) (b)

Figure 2.25: $GDD_{IR} = 70$ fs^2, $TOD_{IR} = -230$ fs^3, $FOD_{IR} = 1250$ fs^4, $GDD_{XUV} = -60$ fs^2, $TOD_{XUV} = 400$ fs^3, $FOD_{XUV} = 1400$ fs^4, $I_{IR} = 4 \cdot 10^{11} \frac{W}{cm^2}$.

Now we wish to enquire how these pulses behave compared to our models. We are therefore going to run SFA simulations of pulses with different kinds of dispersion, and plot the amplitude of the resulting sidebands as a function of the duration of the IR pulse. In these simulations we are going to use an IR intensity of $I_{IR} = 10^{11} \frac{W}{cm^2}$ and a TL duration of the XUV pulses of $\tau_{XUV} = 11$ fs. Furthermore, we are going to investigate the first positive sideband exclusively, as the other sidebands behave similarly.[13]

We are going to study linear chirp to begin with. We shall consider a chirped IR pulse first. From Eq. (2.3.5) we know that chirp is going to vary the time of arrival of certain frequencies, thus broadening the pulse in time. Given the same chirp for each pulse, shorter pulses are the ones which are going to be more affected, experiencing a large dispersion compared to their duration. Hence, shorter pulses are going to be stretched in time and behave like longer ones, resulting in sidebands with a higher-than-expected amplitude. Therefore, we need not consider their TL duration any longer for this type of plot; instead, we must plot the amplitude of the sidebands as a function of the actual $FWHM_{IR}$.

An equivalent reasoning can be applied to linearly chirped XUV pulses. In this case, we are going to need a correction factor for our models, in which $FWHM_{XUV}$ is employed instead of τ_{XUV} inside the square root of Eq. (2.2.11), (2.2.24), and (A.0.4), so to obtain $\frac{1}{\sqrt{1+\frac{FWHM_{XUV}^2}{\tau_{IR}^2}}}$ (and similarly for the other sidebands).

Hence, if we have both pulses which are linearly chirped and we apply both corrections, we anticipate to find again a robust correspondence between models. This is in fact the case, as we see from Figure 2.26. In the following figures, the generating pulses are also shown, in the case of $\tau_{IR} = 10$ fs and $\tau_{XUV} = 11$ fs.

[13] As a final remark, in the following graphs the Taylor expansion presented in Appendix A is considered as well, so to have a more complete outlook on all the models.

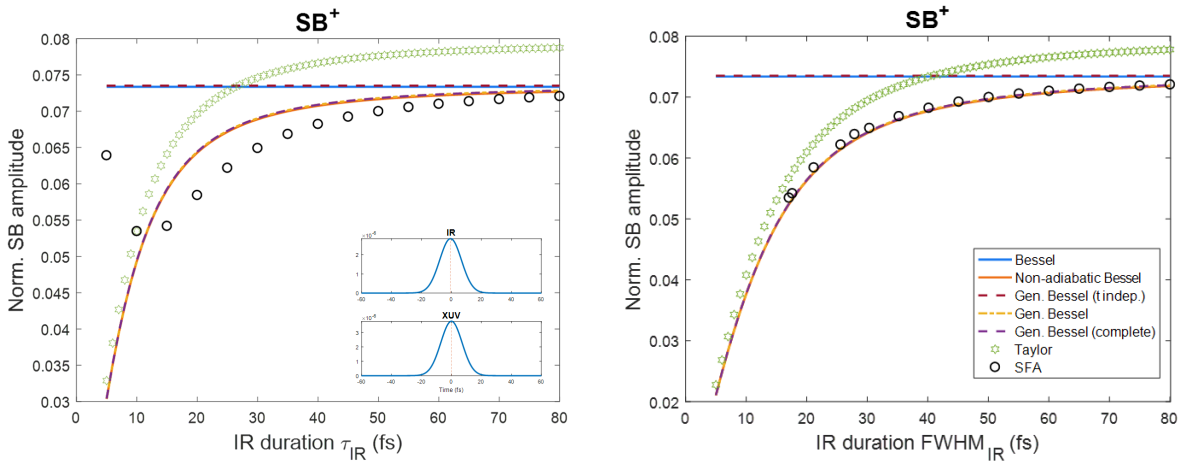

(a) (b)

Figure 2.26: Comparison between models with linearly chirped IR and XUV pulses. $GDD_{IR} = -50$ fs^2, $GDD_{XUV} = 50$ fs^2.

Now we shall move on to non-linear dispersion. Both TOD and FOD result in a distortion of the temporal distribution of the pulses, which now present tails and peaks that are not contemplated by our theory. As a result, our model begins to be less reliable. Indeed, if we simulate a non-linearly dispersed IR pulse we find that the temporal shape of shorter pulses is so distorted that they possess a large $FWHM_{IR}$, while still having a sideband amplitude which is smaller than expected. Therefore, our generalised Bessel model is not valid for these pulses, while it still holds for longer ones. This is true both for the case of a non-null TOD_{IR} and FOD_{IR} (Figure 2.27).

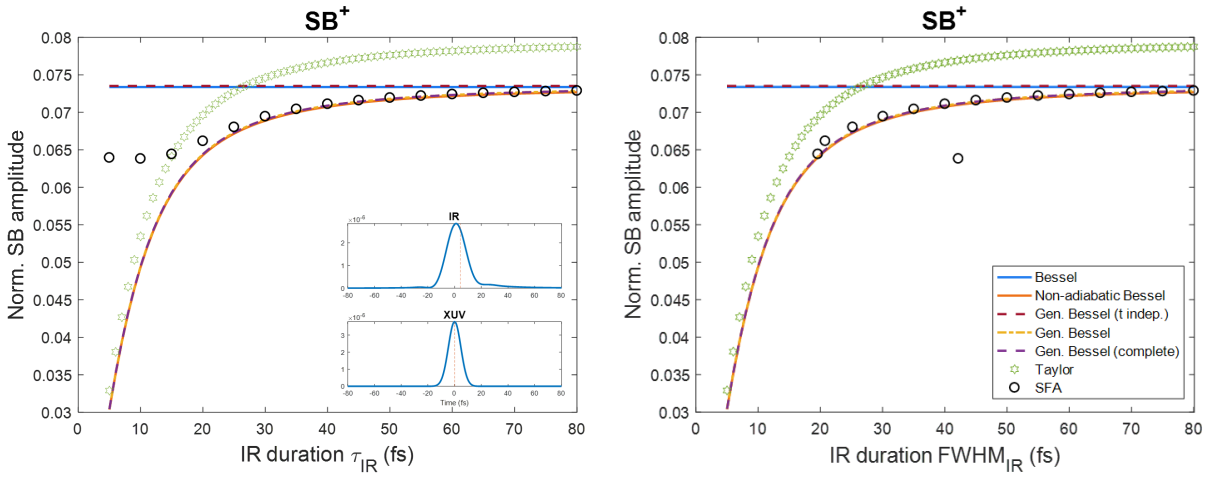

(a) (b)

Figure 2.27: Comparison between models with non-linearly dispersed IR pulse. $TOD_{IR} = 450$ fs^3, $FOD_{IR} = 15000$ fs^4.

On the other hand, with a non-linear dispersion on the XUV pulse we obtain a different result. In fact, since the duration of the XUV pulse is kept constant throughout all the simulations, we are going to have a deformation of the whole curve, without any "jumps" for particular values like those of Figure 2.27b. We can notice this deviation in Figure 2.28b.

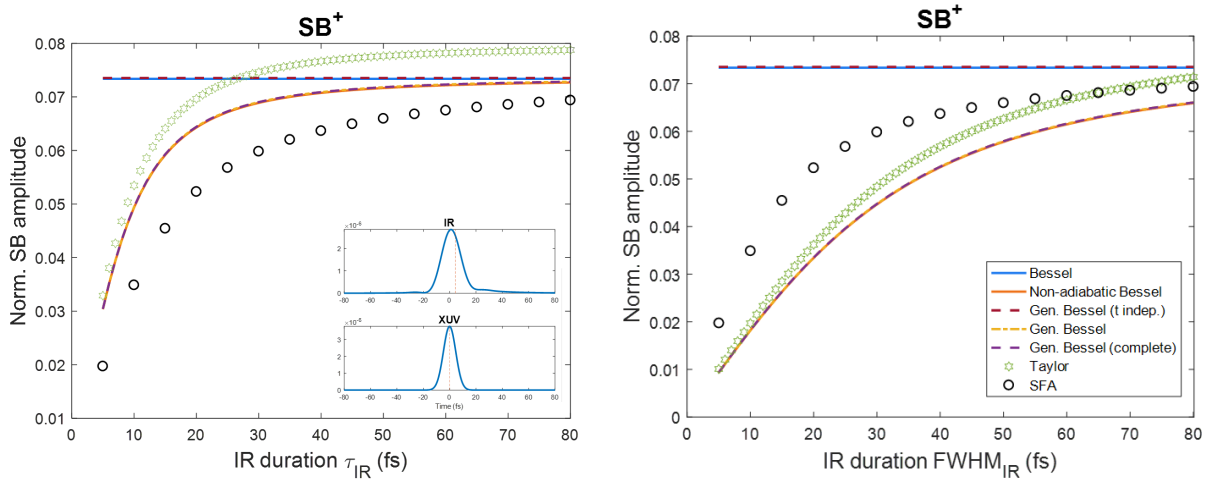

(a) (b)

Figure 2.28: Comparison between models with non-linearly dispersed XUV pulse. $TOD_{XUV} = 650$ fs^3, $FOD_{XUV} = -19000$ fs^4.

Naturally, by combining all these types of dispersion we obtain pulses which are not

temporally Gaussian and which do not strictly follow the previous curve, rather they follow a mixture of the previous trends. As we expect and observe from Figure 2.29 and Figure 2.30, the smaller the dispersion, the more the points calculated through SFA simulations lay on the generalised Bessel line.

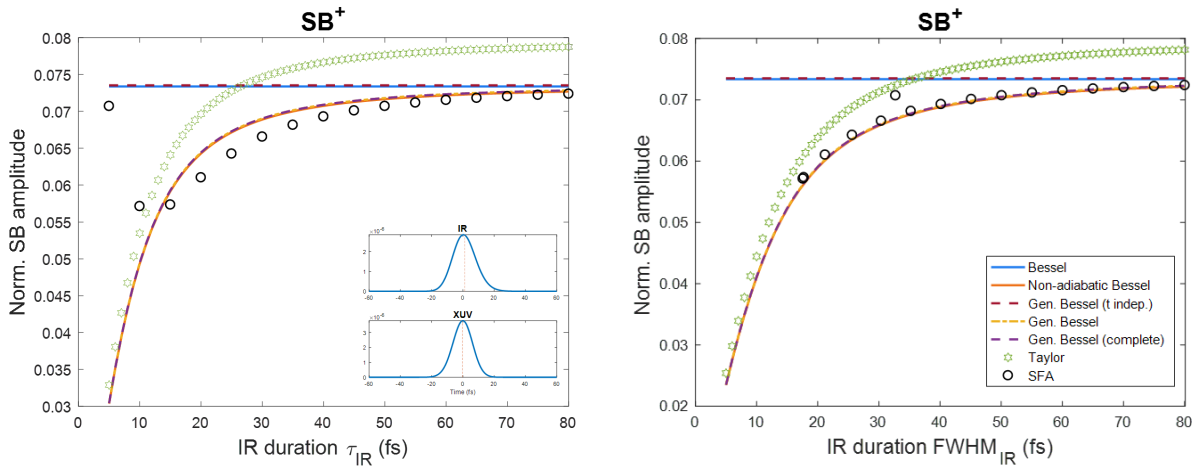

(a) (b)

Figure 2.29: Comparison between models with slightly dispersed IR and XUV pulses. All but one point follow the generalised Bessel model. That deviant point comes from the $\tau_{IR} = 5$ fs pulse, as we expect, and is not very distant from the rest of the curve. $GDD_{IR} = 50$ fs^2, $TOD_{IR} = 75$ fs^3, $FOD_{IR} = 130$ fs^4, $GDD_{XUV} = 40$ fs^2, $TOD_{XUV} = -45$ fs^3, $FOD_{XUV} = -120$ fs^4.

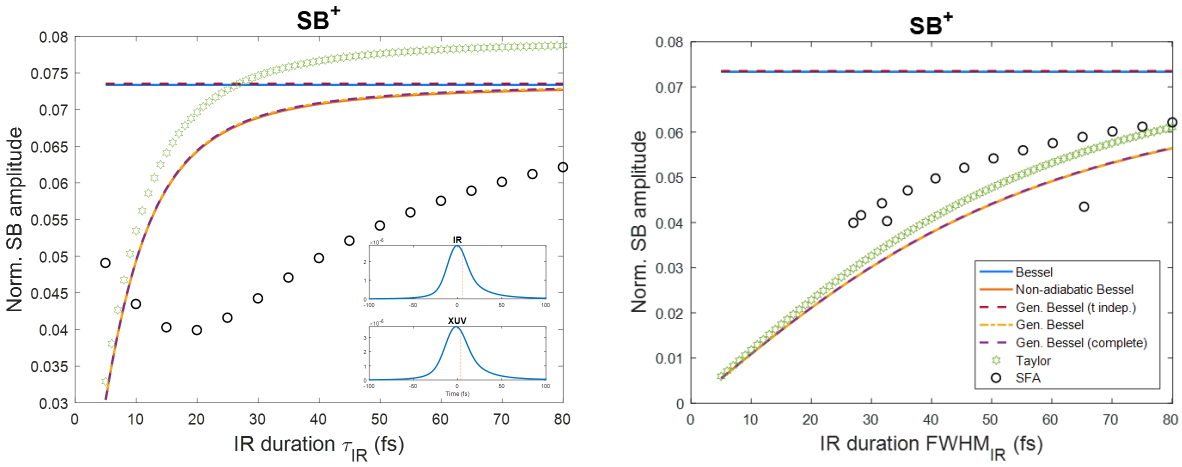

(a) (b)

Figure 2.30: Comparison between models with strongly dispersed IR and XUV pulses. The deviation from the curve is highly visible, and some of the points deriving from shorter pulses do not follow the same curve as the others. $GDD_{IR} = 100$ fs^2, $TOD_{IR} = 500$ fs^3, $FOD_{IR} = 15000$ fs^4, $GDD_{XUV} = -131$ fs^2, $TOD_{XUV} = 656$ fs^3, $FOD_{XUV} = -19000$ fs^4.

3 | Data analysis

After studying the theoretical models, time has come to verify whether they are consistent with the experimental results. In this chapter we will check whether or not the experimental points are close the theoretical lines. If that is not the case, we will also examine the reasons behind the discrepancies and how we can adjust our data accordingly, so to find again a match between model and reality.

3.1. Long-IR limit

We start by considering long IR pulses ($\tau_{IR} \to +\infty$)[1], and we perform our experiments with a variable IR average intensity, in a range spanning from $I_{IR} = 5 \cdot 10^{10} \frac{W}{cm^2}$ to $I_{IR} = 2 \cdot 10^{12} \frac{W}{cm^2}$. We recall from Chapter 2 that we expect to see for each sideband a pattern which follows the modulus square of a generalised Bessel function.

[1] In our case, given $\tau_{XUV} \simeq 11$ fs we will require $\tau_{IR} \gtrsim 100$ fs

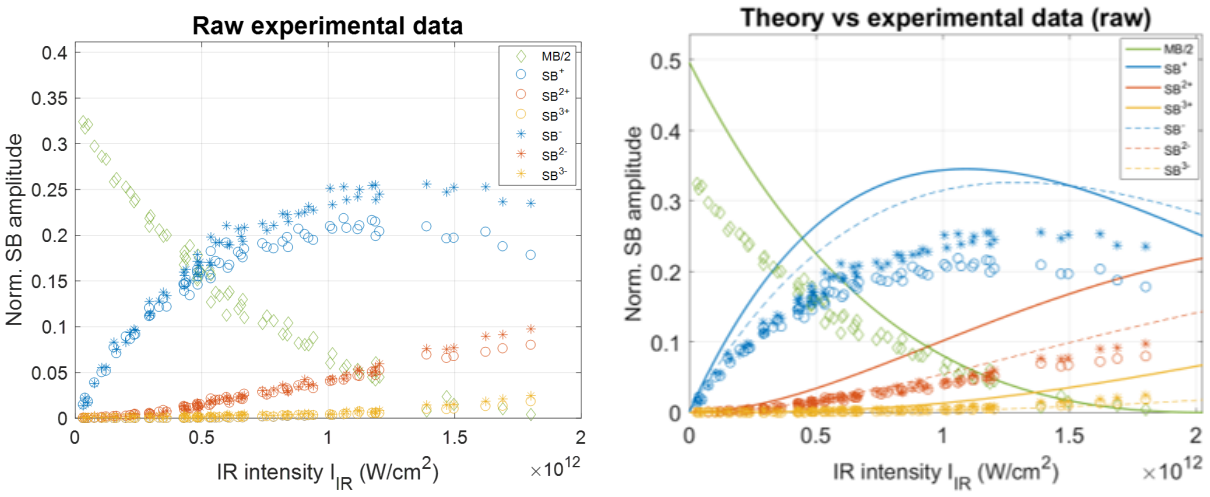

(a) (b)

Figure 3.1: (a) Behaviour of raw data from the first three positive and negative sidebands and from the main band, and (b) comparison with the generalised Bessel model. The amplitude of the main band has been halved in both data and model for better visualisation. In Figure 3.1b, the solid lines represent positive order sidebands (and main band), while the dashed lines represent negative order ones.

From Figure 3.1 it is clear that the experimental points are well below the expected curves. Furthermore, the negative sidebands seem to be at higher values than the positive ones. Nonetheless, they all appear to be following the expected generalised Bessel shape. How can we explain this behaviour?

The reason behind this deviation from the model is to be attributed to the transfer function of the ToF spectrometer. As a matter of fact, the electromagnetic lens generating the electric field inside the ToF acts on the ionised electrons by means of two parameters, namely *lens* and *drift*. The first one controls the focusing of the electrons, whereas the second one dictates their acceleration. They can be selected by the user, and usually having higher lens and drift factors improves the efficiency of counts as a function of time. On the downside, this creates the need for a greater correction.

Therefore, we need to rescale our experimental results considering these two parameters as well. In Figure 3.2 the scaling factors applied to each sideband and to the main band are shown, which are increasing in a monotonic fashion as a function of the sideband order. They were found by minimising the RMS distance between experimental data and the curve of each SB. In Figure 3.3 we observe how this affects our results, which now lie onto the theoretical curves.

Figure 3.2: Correction factor α as a function of the sideband order. It is a monotonically increasing function, and the error grows with the order (positive or negative) of the sideband.

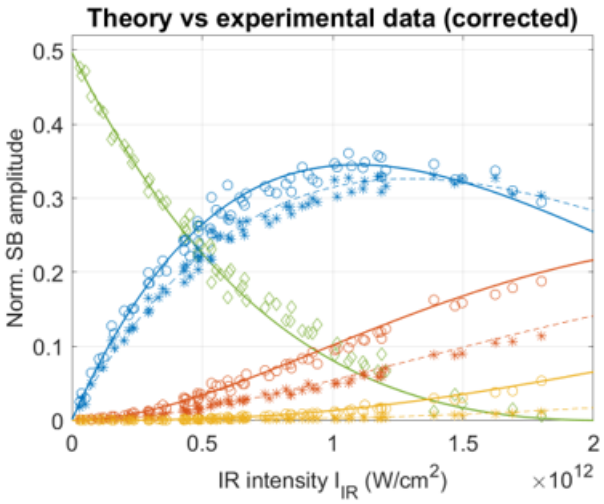

Figure 3.3: Comparison between corrected data and theoretical model. The data have a good match with the respective generalised Bessel lines. As expected, the negative order sidebands are now below the positive ones.

Hence, we conclude that in the range of intensities we explored, Floquet theory in the approximation of generalised Bessel functions is **reliable** in its description of the generation and population of sidebands due to two-colour photoemission, provided we are in the limit of long IR pulses ($\tau_{IR} >> \tau_{XUV}$) and that we account for both lens and drift factors.

Now we shall investigate the case of IR pulses of variable time duration.

3.2. Variable IR duration

The duration of the IR pulses is now set to explore the range between $\tau_{IR} = 5$ fs and $\tau_{IR} = 50$ fs, using an average intensity of $I_{IR} = 5 \cdot 10^{11} \frac{W}{cm^2}$. The following figures display the outcome of these measurements, side by side with the theoretical values given by the generalised Bessel approximation. Only the main band and the first two positive sidebands will be considered, for simplicity (the other sidebands yield similar results).

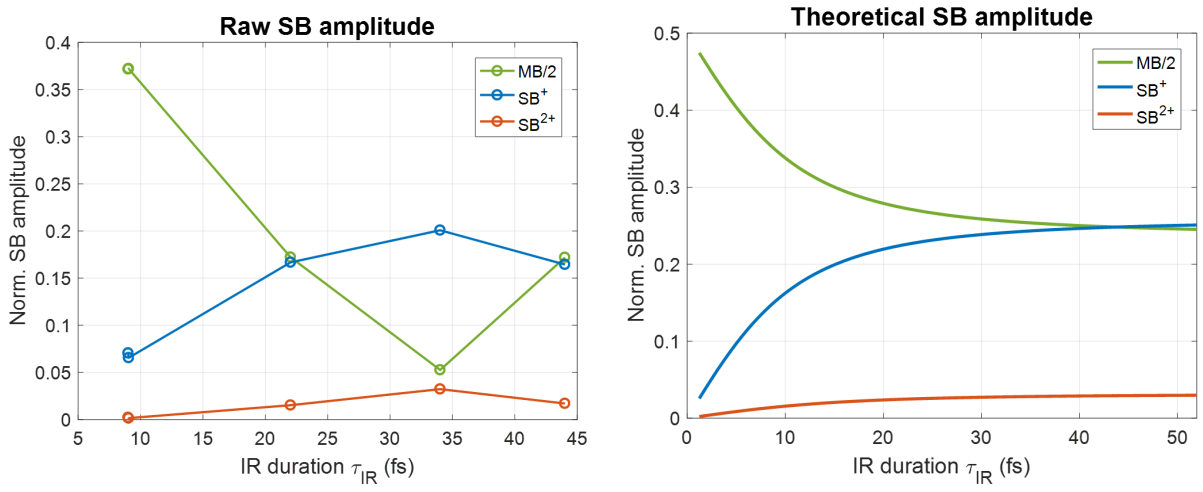

(a) (b)

Figure 3.4: (a) Raw data compared to (b) theoretical model. In Figure 3.4b, $\tau_{XUV} = 12.33$ fs was considered.

What we immediately observe from Figure 3.4, is that the general trend of the data abides by the expected behaviour of the theoretical curves obtained through the generalised Bessel functions, i.e. the data do actually depend on time and the sideband amplitudes grow with τ_{IR}. Nevertheless, the final curve given by the data does not seem to adhere to the anticipated shape, which is monotonic and does not present any extreme.

We can make sense of this discrepancy by recalling that each pulse is affected by dispersion. Since different duration IR pulses are obtained through the variation of the pressure of gas inside the HCF, the pulses generated in each experiment are subject to different amounts of GDD, TOD, and FOD. Hence, by knowing the dispersion of every pulse we should be able to predict the behaviour of the main band and of the sidebands. Through STRIPE reconstructions of the pulses and of the spectrogram, we are capable of retrieving all of the required values of dispersion and of calculating the values of the bands in $\tau = 0$. In Figure 3.5, the comparison between the raw data and the STRIPE reconstructions, which take into consideration the dispersion of the single pulses.

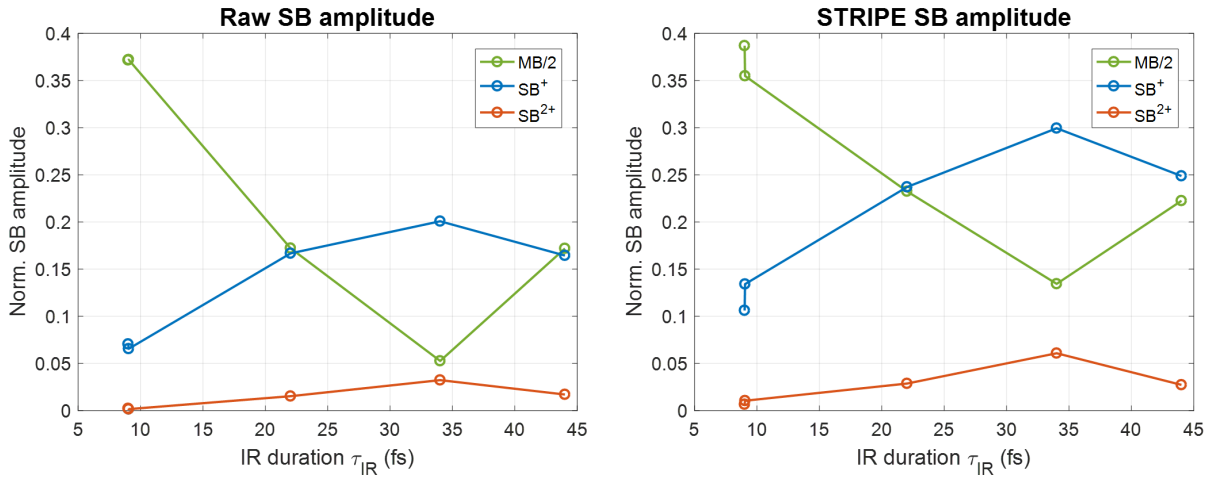

(a) Raw data from the experiments.

(b) STRIPE reconstruction.

Figure 3.5: (a) Raw data compared to (b) STRIPE reconstruction, which considers the dispersion of both IR and XUV pulses.

The trend of the acquired data now aligns to that of the reconstructed bands, yet the actual values do not match the expected ones. The first issue we encounter is the duration of the XUV pulses. We considered the same duration for all pulses, but this was just a reasonable assumption. It is necessary to check whether τ_{XUV} deviates from the value we utilised. In Figure 3.6 we examine the duration of both IR and XUV pulses, and the effect of the variation of the XUV duration on the theoretical curve of the first positive sideband.

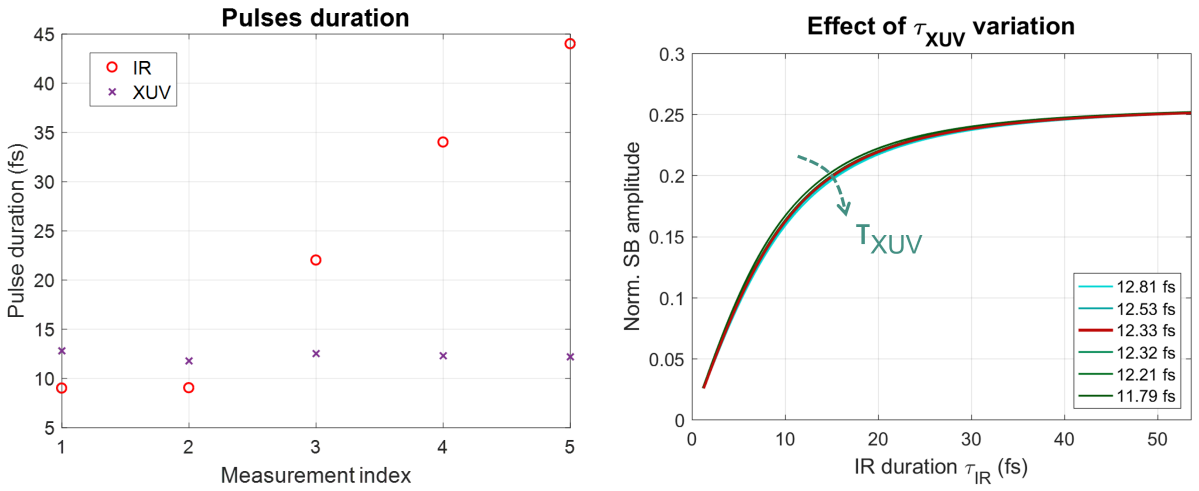

(a) (b)

Figure 3.6: (a) duration of the employed IR and XUV pulses; (b) effect on the SB amplitude of the variation in XUV duration. The durations plotted in Figure 3.6b are those of the actual pulses and their mean (in red), which is the value used in the previous simulations.

From the previous graphs it is clear that the XUV pulses do not undergo substantial variations. Hence, by using the average value in the theoretical model we do not commit a tangible error. Therefore, in order to understand why we have a deviation between model and data we need to look into two different parameters which might change: the average intensity of the IR beam (Figure 3.7) and the generating IR wavelength (Figure 3.8).

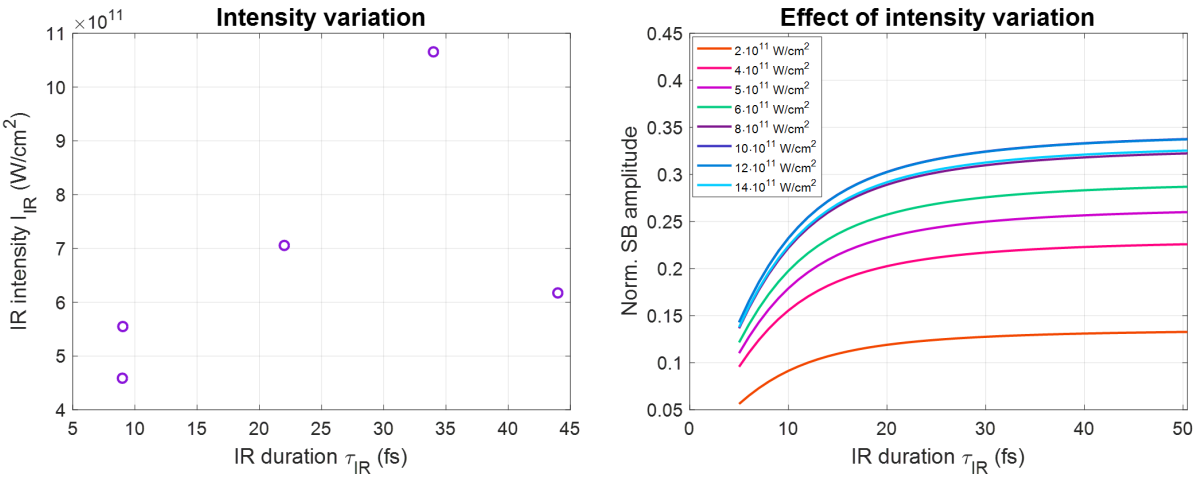

(a) (b)

Figure 3.7: (a) variation in intensity for each pulse; (b) effect of this intensity variation. In Figure 3.7b, the aqua line represents the expected intensity, which was used in the simulations.

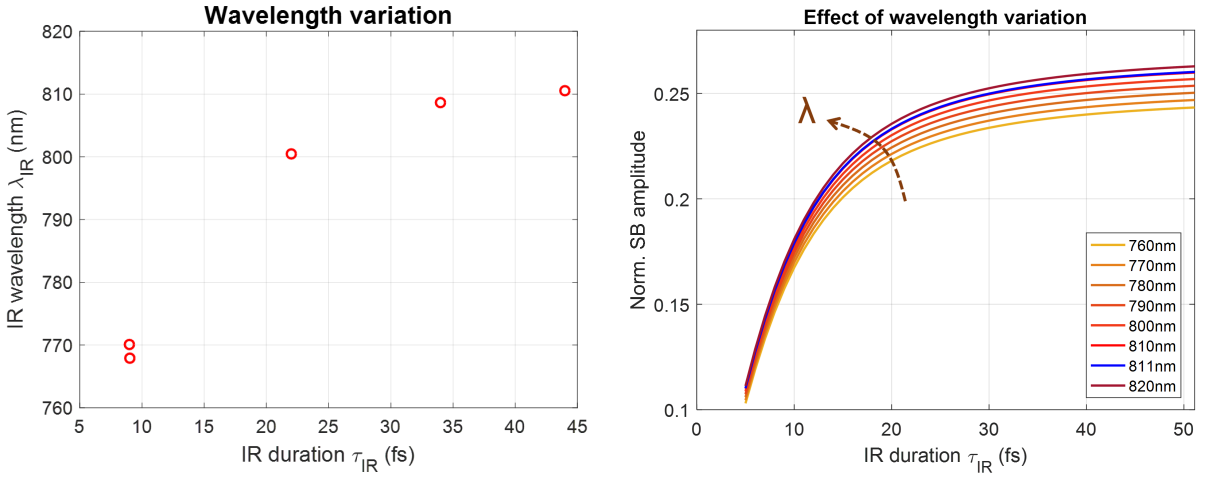

(a) (b)

Figure 3.8: (a) variation in wavelength for each pulse; (b) effect of this wavelength variation. In Figure 3.8b, the blue line represents the expected wavelength, which was used in the simulations.

The fluctuations from pulse to pulse in both intensity and wavelength are non-negligible, and their effect on the amplitude of main band and sidebands is manifest. It was already known that a variation in intensity leads to the bands moving in amplitude in a generalised Bessel trend. Therefore, a large variation in intensity such as the one experienced for

$\tau_{IR} = 34$ fs is bound to contribute to a large deviation from the reconstructed value. Similarly, having different IR wavelengths for each pulse creates a difference in the outcome of our measurement, especially at a higher IR duration. Hence, if these two factors diverge from their expected values of $I_{IR} = 5 \cdot 10^{11} \frac{W}{cm^2}$ and $\lambda_{IR} = 811$ nm, this results in a discrepancy between theoretical model and acquired data.

Nevertheless, the general behaviour of the bands is clear. Through Floquet theory we were able to predict the decreasing trend in the sidebands amplitude (increasing in case of the main band) as the IR pulses decrease in duration. This implies that Floquet theory may still be applied to short, few-cycle pulses, even if we have a loss of periodicity and an increase in border effects. Moreover, we demonstrated that having $\tau_{IR} > \tau_{XUV}$ is not strictly necessary, as in the previous graphs we employed two IR pulses at $\tau_{IR} = 9$ fs while having $\tau_{XUV} \simeq 12$ fs. This also suggests that it is not necessary for τ_{IR} to be much greater than T_{IR}. Indeed, in the case of $\tau_{IR} = 9$ fs we have $T_{IR} = 2.57$ fs ($\lambda_{IR} = 770$ nm), therefore we only require $\tau_{IR} > T_{IR}$ (which is the simple condition to have a pulse).

As a final remark, we can observe in Figure 3.9 the complete behaviour of the first two positive sidebands and of the main band, spanning the range of $\tau_{IR} = 5 \div 160$ fs. In the short IR duration range we notice the bend in the graph given by the presence of the $\frac{1}{\sqrt{1+N\cdot(\frac{\tau_{XUV}}{\tau_{IR}})^2}}$ term, while in the long IR pulse limit the curve goes towards the asymptotic value given by the original Floquet theory.

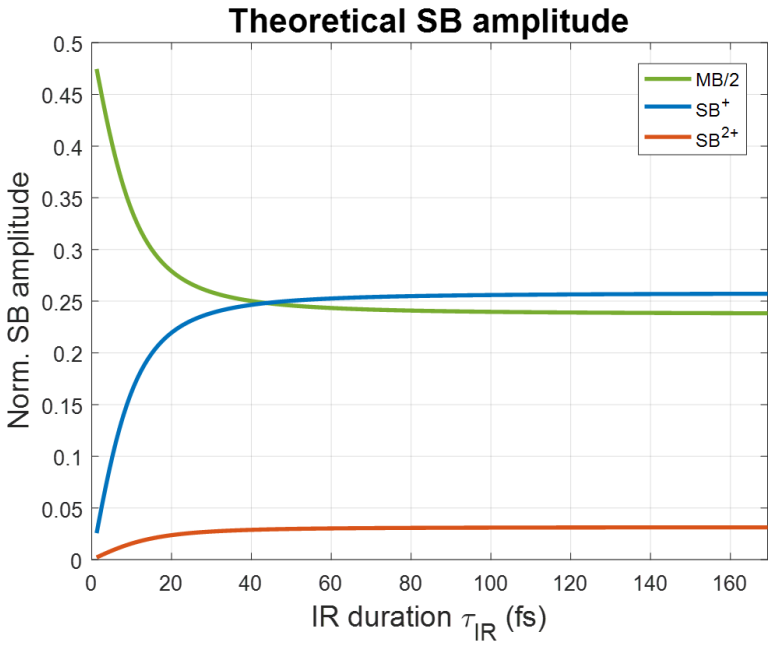

Figure 3.9: Complete behaviour of the theoretical model, considering the range of both short and long IR pulses.

4 | Conclusions

During the course of this thesis work we employed principles of ultrafast optics to explore Floquet theory in the limit of short pulse duration.

In the beginning we discussed the general concept of Floquet theory as a way to describe systems undergoing a periodic perturbation, together with some of its implications. In particular, we discussed the Floquet theorem and how it is possible to write the wave function of a particle in the Time-Dependent Schrödinger Equation as $|\psi(t)\rangle = |\phi(t)\rangle\, e^{-i\epsilon t}$, with ϕ being a T-periodic function and ϵ the Floquet quasi-energy. This gives the opportunity for a series expansion that will be largely exploited in our theoretical analysis of the experiment.

We also mentioned some of its practical applications in the description of physical phenomena, especially in condensed matter physics and in optics, and in the relatively new field of Floquet engineering. Specifically, we focused on ultrafast optics and inquired whether the use of ultrashort pulses would hinder the utilisation of Floquet theory due to their non-perfect periodicity. As a solution to this quandary, we proposed an experiment consisting in a pump-probe technique with ultrashort (femtosecond) IR and XUV pulses to research the behaviour of Ne gas. Afterwards, we analysed the optical setup employed for the aforementioned pump-probe experiment and presented the experimental results.

In our experiments we used the XUV pulses to ionise the gas and generate the main band, and employed the IR beam to drive the electron dynamics and dress the Floquet states, thus populating the sidebands. This process was repeated for numerous time delays between probe and pump until we obtained a complete spectrogram of the amplitudes as a function of both energy and delay. To characterise these spectrograms the main figures of merit of the IR and XUV beams needed to be analysed as well, such as their spectra, phase, intensity, or beam profile. Many techniques were employed to characterise both pulses. Some of them were already well-known, such as the FROG setup, while others were implemented ad hoc for this experiment, like STRIPE. Through these methods, and by normalising, fitting and cleaning the signal from the tails caused by electronic effects, we were able to reconstruct both IR and XUV pulses. This also helped us retrieve the

values of dispersion, which were of paramount importance in the study of the theoretical model.

4.1. Interpretation of the results

We started from the derivation of the model through Strong Field Approximation, to then simplify it by taking advantage of approximations and series expansions. At first, we chose not to consider the quadratic term of the vector potential (A_{IR}^2), as it was deemed negligible. Afterwards, as a first approximation we decided to perform a frequency expansion. This expansion was found to be considerably effective. In fact, each order of approximation, consisting in a Bessel function of the first kind, fully represents a single sideband. This expansion was performed in an adiabatic fashion, without considering the duration of the pulses, which on the contrary we believed to have an impact on the result. Indeed, through a non-adiabatic approximation and considering temporally Gaussian pulses we observed a substantial attenuation of the amplitude of the Bessel functions for $\frac{\tau_{XUV}^2}{\tau_{IR}^2} \to +\infty$.

Further studies were performed to examine the dependence of the sideband amplitude on the IR duration. Here we found a discrepancy between non-adiabatic Bessel expansion and SFA model with the variation of intensity. The A_{IR}^2 term resulted to be less and less negligible the more we raised the IR intensity. The threshold over which we could still tolerate the absence of the quadratic term depended on the order of the sideband we were considering: first order sidebands were nearly unaffected by the initial approximation until I_{IR} was in the order of $10^{11}\frac{W}{cm^2}$, whereas from the second order sidebands on we noticed a discrepancy between models already at $I_{IR} = 10^9\frac{W}{cm^2}$. Hence, we decided to include the missing term in the frequency expansion, obtaining a final model which follows the behaviour of the so-called generalised Bessel functions. This new approximation, although slightly more complex than the previous ones, seems to be remarkably close to the results of the SFA model for higher order sidebands, while SB^+ and SB^- are still not perfectly aligned with the expected values. Finally, we observed the effects of non-idealities such as dispersion. We concluded that GDD does not have a relevant effect on our models, as it maintains the Gaussian shape of the pulse, whereas TOD and especially FOD strongly impact the final results, which do not always match.

As a final step, we compared the results of our theoretical analysis with the actual data acquired from the experiments. The first results were devoted to verify the behaviour of the amplitudes of MB and SB as a function of the IR intensity in the long IR limit. The general trend of the data followed the generalised Bessel functions predicted by the

theoretical model, confirming that our generalised Bessel approximation is reliable and accurate in the range of intensities we explored ($I_{IR} = 5 \cdot 10^{10} \div 2 \cdot 10^{12} \frac{W}{cm^2}$).

Afterwards, we focused on the impact of the duration of our pulses on the theoretical model. We set the average intensity at $I_{IR} = 5 \cdot 10^{11} \frac{W}{cm^2}$ and let the IR duration vary in the range $\tau_{IR} = 5 \div 50$ fs, while keeping $\tau_{XUV} \simeq 12$ fs. We immediately verified the decreasing of the amplitude for shorter IR pulses, yet the data curve did not completely follow the theoretical line. In fact, the model does not account for dispersion, so we had to use the STRIPE algorithm to retrieve GDD, TOD and FOD of the pulses and reconstruct the main band and sideband amplitudes. Then, we decided to inspect the values which we considered to be constant, such as the XUV duration, the IR intensity and the wavelength of the generating IR beam. What we discovered is that the XUV pulses maintained a similar duration throughout the whole experiment ($\tau_{XUV} = 11.79 \div 12.81$ fs), thus leading to small differences with the theory. On the other hand, I_{IR} and λ_{IR} were subject to non-negligible variations ($I_{IR} = 0.92 \cdot 10^{12} \div 2.13 \cdot 10^{12} \frac{W}{cm^2}$ and $\lambda_{IR} = 768 \div 811$ nm), which resulted in the deviations from the generalised Bessel model we observed. Regardless of these dissimilarities, the general behaviour of the experimental results demonstrated that we do not necessarily require long IR pulses to apply Floquet theory, nor having $\tau_{IR} > \tau_{XUV}$ is needed. Furthermore, it is sufficient to have τ_{IR} slightly greater than T_{IR} (in our case $\tau_{IR}^{min} \simeq 2 \cdot T_{IR}$, less than an order of magnitude greater).

4.2. Future developments

The results obtained in this thesis may be considered satisfactory, yet some improvements could be made to advance our knowledge on Floquet theory and its limits.

Regarding the dependence on the intensity of the sideband amplitudes, we observed the beginning of the depleting process in the first positive and negative sidebands. It would be interesting to study the full depletion of those sidebands and verify whether they actually reach a zero like the main band, or if some other physical effects come into play, disrupting the model. For such an improvement we would need to be capable of increasing the intensity of the laser up to around $I_{IR} \sim 10^{13} \frac{W}{cm^2}$. A possible way of increasing the total power (aside from substituting the laser system) is diminishing the losses of the HCF. To do so we may implement a stretchable HCF [35] which would substitute the current one and allow to reach higher IR intensities. Moreover, a stretchable fibre could allow a shorter pulse duration, which would be useful to verify which is the lower limit for τ_{IR} with respect to T_{IR}. The model predicts that the SB amplitudes should also depend on the XUV time duration. In a future experiment we could test if this prediction is

correct by changing the duration of the XUV pulses in the monochromator. Moreover, the SB amplitude is expected to change with the electron momentum. This aspect could be verified by repeating the experiment with a different selected harmonic (at higher or lower energy).

Another improvement could be to perform new STRIPE simulations to take into consideration and quantify the variation of IR intensity and wavelength, so to correct our data accordingly. This way we would be able to further verify the accuracy of our model. Therefore, an additional objective would be to gather more data with several values of τ_{IR}, spanning the $5 \div 50$ fs range multiple times.[1]

In this dissertation we investigated Floquet theory employing Ne gas as the only target in our pump-probe experiment. Being a noble gas, Ne possesses a simple structure, it is inert and is naturally a monoatomic element. When we excited it with our XUV pulses, we generated free electrons, and those were the subject of our study. It would be fascinating to explore not only free electrons, but also bound states of more complex systems, starting from diatomic molecules, up to organic molecules and solid-state materials. Theoretical analyses of bound states through Floquet theory have been performed [12, 27, 53], it would be significant to explore experimentally their behaviour when brought to the limit of ultrashort pulses. In particular, bound states of few-layer semiconductors, semimetals and topological insulators are of particular interest for electronic applications, and are therefore some of the most investigated materials for Floquet engineering [18, 28]. So, an intriguing future perspective would be to characterise the behaviour of some of these materials according to Floquet theory through ultrashort pulses using a few-femtosecond pump-probe technique.

[1] Note that the above-mentioned IR range is to be considered for a fixed τ_{XUV} close to 12 fs, which is what we employed in Chapter 3. If τ_{XUV} changes significantly, the range of interest will too.

Bibliography

[1] K. Amini, J. Biegert, F. Calegari, and M. F. Ciappina. Symphony on strong field approximation. *Reports on Progress in Physics*, 82(11):116001, oct 2019. doi: 10.1088/1361-6633/ab2bb1. URL https://doi.org/10.1088/1361-6633/ab2bb1.

[2] A. Armaroli and F. Biancalana. Tunable modulational instability sidebands via parametric resonance in periodically tapered optical fibers. *Opt. Express*, 20(22):25096–25110, Oct 2012. doi: 10.1364/OE.20.025096. URL http://www.osapublishing.org/oe/abstract.cfm?URI=oe-20-22-25096.

[3] A. Bain and R. Dumont. Introduction to floquet theory: The calculation of spinning sideband intensities in magic-angle spinning nmr. *Concepts in Magnetic Resonance*, 13:159 – 170, 01 2001. doi: 10.1002/cmr.1006.

[4] M. Bukov, L. Dalessio, and A. Polkovnikov. Universal high-frequency behavior of periodically driven systems: from dynamical stabilization to floquet engineering. *Advances in Physics*, 64, 07 2014. doi: 10.1080/00018732.2015.1055918.

[5] L. Cattaneo, J. Vos, M. Lucchini, L. Gallmann, C. Cirelli, and U. Keller. Comparison of attosecond streaking and rabbitt. *Opt. Express*, 24(25):29060–29076, Dec 2016. doi: 10.1364/OE.24.029060. URL http://opg.optica.org/oe/abstract.cfm?URI=oe-24-25-29060.

[6] C. Chicone. *Ordinary Differential Equations with Applications*, volume 34. 01 2006. ISBN 978-0-387-30769-5. doi: 10.1007/0-387-35794-7.

[7] Coherent. Astrella - integrated khz ultrafast ti:s amplifiers, . URL https://www.coherent.com/lasers/amplifiers/astrella.

[8] Coherent. Vitara - flexible ultrashort pulse ti:s lasers, . URL https://www.coherent.com/lasers/oscillators/vitara.

[9] Coherent. Revolution - high energy khz green lasers, . URL https://www.coherent.com/lasers/amplifiers/revolution.

[10] S. Coop, S. Palacios, P. Gomez, Y. N. M. de Escobar, T. Vanderbruggen, and

M. W. Mitchell. Floquet theory for atomic light-shift engineering with near-resonant polychromatic fields. *Opt. Express*, 25(26):32550–32559, Dec 2017. doi: 10.1364/OE.25.032550. URL http://www.osapublishing.org/oe/abstract.cfm?URI=oe-25-26-32550.

[11] U. De Giovannini and H. Huebener. Floquet analysis of excitations in materials. *Journal of Physics: Materials*, 3, 08 2019. doi: 10.1088/2515-7639/ab387b.

[12] G. Della Valle and S. Longhi. Floquet-hubbard bound states in the continuum. *Phys. Rev. B*, 89:115118, Mar 2014. doi: 10.1103/PhysRevB.89.115118. URL https://link.aps.org/doi/10.1103/PhysRevB.89.115118.

[13] A. Eckardt. Colloquium: Atomic quantum gases in periodically driven optical lattices. *Reviews of Modern Physics*, 89:011004, 2017. doi: 10.1103/RevModPhys.89.011004. URL https://doi.org/10.1103/RevModPhys.89.011004.

[14] H. Eckert. Solid-state be-9 nmr of beryllium compounds. *Zeitschrift für Naturforschung B*, 75(5):441–458, 2020. doi: doi:10.1515/znb-2020-0026. URL https://doi.org/10.1515/znb-2020-0026.

[15] T. Elsaesser. Introduction: Ultrafast processes in chemistry. *Chemical Reviews*, 117 (16):10621–10622, 2017. doi: 10.1021/acs.chemrev.7b00226. URL https://doi.org/10.1021/acs.chemrev.7b00226. PMID: 28830148.

[16] G. Floquet. Sur les équations différentielles linéaires à coefficients périodiques. *Annales scientifiques de l'École Normale Supérieure*, 2e série, 12:47–88, 1883. doi: 10.24033/asens.220. URL http://www.numdam.org/articles/10.24033/asens.220/.

[17] P. Gabolde, P. Bowlan, and R. Trebino. Measuring everything you've always wanted to know about an ultrashort pulse but thought couldn't be done. In *Frontiers in Optics 2007/Laser Science XXIII/Organic Materials and Devices for Displays and Energy Conversion*, page FWG1. Optica Publishing Group, 2007. doi: 10.1364/FIO.2007.FWG1. URL http://opg.optica.org/abstract.cfm?URI=FiO-2007-FWG1.

[18] H. Hübener, M. A. Sentef, U. De Giovannini, A. F. Kemper, and A. Rubio. Creating stable floquet–weyl semimetals by laser-driving of 3d dirac materials. *Nature Communications*, 8(1), Jan 2017. ISSN 2041-1723. doi: 10.1038/ncomms13940. URL http://dx.doi.org/10.1038/ncomms13940.

[19] T. Iadecola and T. Hsieh. Floquet supersymmetry. *Physical Review Letters*, 120, 10 2017. doi: 10.1103/PhysRevLett.120.210603.

[20] K. L. Ivanov, K. R. Mote, M. Ernst, A. Equbal, and P. K. Madhu. Floquet

theory in magnetic resonance: Formalism and applications. *Progress in Nuclear Magnetic Resonance Spectroscopy*, 126-127:17–58, 2021. ISSN 0079-6565. doi: https://doi.org/10.1016/j.pnmrs.2021.05.002. URL https://www.sciencedirect.com/science/article/pii/S0079656521000169.

[21] M. Jangjan and M. Hosseini. Floquet engineering of topological metal states and hybridization of edge states with bulk states in dimerized two-leg ladders. *Scientific Reports*, 10, 08 2020. doi: 10.1038/s41598-020-71196-3.

[22] M. A. Jørgensen. Driven problems in quantum and classical mechanics with floquet theory. Master's thesis, Niels Bohr Institute, University of Copenhagen, 2015.

[23] C. Kastl, C. Karnetzky, A. Brenneis, F. Langrieger, and A. Holleitner. Topological insulators as ultrafast auston switches in on-chip thz-circuits. *IEEE Journal of Selected Topics in Quantum Electronics*, 23(4):1–5, 2017. doi: 10.1109/JSTQE.2016.2641343.

[24] M. Kitzler-Zeiler, N. Milosevic, A. Scrinzi, F. Krausz, and T. Brabec. Quantum theory of attosecond xuv pulse measurement by laser dressed photoionization. *Physical review letters*, 88:173904, 05 2002. doi: 10.1103/PhysRevLett.88.173904.

[25] J. Ladislas Wiza. Microchannel plate detectors. *Nuclear Instruments and Methods*, 162(1):587–601, 1979. ISSN 0029-554X. doi: https://doi.org/10.1016/0029-554X(79)90734-1. URL https://www.sciencedirect.com/science/article/pii/0029554X79907341.

[26] N. Lindner, G. Refael, and V. Galitski. Floquet topological insulator in semiconductor quantum wells. *Nature Physics*, 7(6):490–495, June 2011. ISSN 1745-2473. doi: 10.1038/nphys1926.

[27] S. Longhi and G. D. Valle. Floquet bound states in the continuum. *Scientific Reports*, 3, 2013. doi: 10.1038/srep02219.

[28] A. Lubatsch and R. Frank. Evolution of floquet topological quantum states in driven semiconductors. *The European Physical Journal B*, 92(9), Sep 2019. ISSN 1434-6036. doi: 10.1140/epjb/e2019-100087-0. URL http://dx.doi.org/10.1140/epjb/e2019-100087-0.

[29] L. B. Madsen. Strong-field approximation in laser-assisted dynamics. *American Journal of Physics*, 73(1):57–62, 2005. doi: 10.1119/1.1796791. URL https://doi.org/10.1119/1.1796791.

[30] J. Maurer and U. Keller. Ionization in intense laser fields beyond the electric dipole approximation: concepts, methods, achievements and future directions. *Journal of*

Physics B: Atomic, Molecular and Optical Physics, 54(9):094001, may 2021. doi: 10.1088/1361-6455/abf731. URL https://doi.org/10.1088/1361-6455/abf731.

[31] L. Medišauskas, U. Saalmann, and J. Rost. Floquet approach for dynamics in short and intense laser pulses. *Journal of Physics B: Atomic, Molecular and Optical Physics*, 52, 06 2017. doi: 10.1088/1361-6455/aaef42.

[32] B. Moio, F. Medeghini, G. L. Dolso, G. Inzani, N. D. Palo, R. Borrego-Varillas, M. Nisoli, and M. Lucchini. Reconstruction of few-fs XUV pulses with a perturbative approach. *EPJ Web of Conferences*, 255:11008, 2021. doi: 10.1051/epjconf/202125511008. URL https://doi.org/10.1051/epjconf/202125511008.

[33] S. Mondal, Q. Wei, M. A. Fareed, H. A. Hafez, X. Ropagnol, S. Sun, S. Kahaly, and T. Ozaki. Ultrafast plasma electron dynamics: A route to terahertz pulse shaping. *Phys. Rev. Applied*, 13:034044, Mar 2020. doi: 10.1103/PhysRevApplied.13.034044. URL https://link.aps.org/doi/10.1103/PhysRevApplied.13.034044.

[34] P. Mulser and D. Bauer. *High Power Laser-Matter Interaction*. Springer Berlin Heidelberg, 2010. doi: 10.1007/978-3-540-46065-7. URL https://doi.org/10.1007/978-3-540-46065-7.

[35] T. Nagy, P. Simon, and L. Veisz. High-energy few-cycle pulses: post-compression techniques. *Advances in Physics: X*, 6(1):1845795, 2021. doi: 10.1080/23746149.2020.1845795. URL https://doi.org/10.1080/23746149.2020.1845795.

[36] M. Nisoli, P. Decleva, F. Calegari, A. Palacios, and F. Martín. Attosecond electron dynamics in molecules. *Chemical reviews*, 117 16:10760–10825, 2017.

[37] T. Oka and S. Kitamura. Floquet engineering of quantum materials. *Annual Review of Condensed Matter Physics*, 10, 04 2018. doi: 10.1146/annurev-conmatphys-031218-013423.

[38] T. Polenova, R. Gupta, and A. Goldbourt. Magic angle spinning nmr spectroscopy: A versatile technique for structural and dynamic analysis of solid-phase systems. *Analytical Chemistry*, 87(11):5458–5469, 2015. doi: 10.1021/ac504288u. URL https://doi.org/10.1021/ac504288u. PMID: 25794311.

[39] L. Poletto and P. Villoresi. Time-delay compensated monochromator in the off-plane mount for extreme-ultraviolet ultrashort pulses. *Applied Optics*, 45(34):8577, Dec. 2006. doi: 10.1364/ao.45.008577. URL https://doi.org/10.1364/ao.45.008577.

[40] H. R. Reiss. Effect of an intense electromagnetic field on a weakly bound system.

Phys. Rev. A, 22:1786–1813, Nov 1980. doi: 10.1103/PhysRevA.22.1786. URL `https://link.aps.org/doi/10.1103/PhysRevA.22.1786`.

[41] G. Santoro. Introduction to floquet. Lecture Notes, 2019.

[42] M. Sayraç. Computation of refractive index values of inert gases at near infrared and xuv region based on mathematica software. *Adıyaman University Journal of Science*, 04 2021. doi: 10.37094/adyujsci.754497.

[43] D. Shin, H. Hübener, U. De Giovannini, H. Jin, A. Rubio, and N. Park. Phonon-driven spin-floquet magneto-valleytronics in mos2. *Nature Communications*, 9, 02 2018. doi: 10.1038/s41467-018-02918-5.

[44] StandfordComputerOptics. Image intensifier: Phosphor screen. URL `https://stanfordcomputeroptics.com/technology/image-intensifier/phosphor-screen.html`.

[45] V. Strelkov, V. Platonenko, A. Sterzhantov, and M. Ryabikin. Attosecond electromagnetic pulses: Generation, measurement, and application. generation of high-order harmonics of an intense laser field for attosecond pulse production. *Physics-Uspekhi*, 59:425–445, 01 2016. doi: 10.3367/UFNe.2015.12.037670.

[46] O. Svelto. *Principle of Lasers*. Springer, 5 edition, 2010.

[47] SwampOptics. Frequency-resolved optical gating: Frog. URL `https://www.swampoptics.com/frog.html`.

[48] R. Trebino, K. DeLong, D. Fittinghoff, J. Sweetser, M. Krumbuegel, B. Richman, and D. Kane. Measuring ultrashort laser pulses in the time-frequency domain using frequency-resolved optical gating. *Review of Scientific Instruments*, 68:3277–3295, 09 1997. doi: 10.1063/1.1148286.

[49] F. Vismarra. Strong field-electron-xuv interaction simulator: study of ensemble effects in attosecond streaking spectroscopy. Master's thesis, Politecnico di Milano, 2020.

[50] C. Weitenberg and J. Simonet. Tailoring quantum gases by Floquet engineering. *Nature Physics*, 17(12):1342–1348, Aug. 2021. doi: 10.1038/s41567-021-01316-x.

[51] E. Wientjes and P. Lambrev. Ultrafast processes in photosynthetic light-harvesting. *Photosynthesis Research*, 144, 04 2020. doi: 10.1007/s11120-020-00755-6.

[52] M. Zavelani-Rossi and F. Vismarra. *High Intensity Lasers for Nuclear and Physical Applications*. Società Editrice Esculapio, 2 edition, 2020.

[53] B. Zhu, Y. Ke, W. Liu, Z. Zhou, and H. Zhong. Floquet-surface bound states in the continuum in a resonantly driven one-dimensional tilted defect-free lattice. *Phys. Rev. A*, 102:023303, Aug 2020. doi: 10.1103/PhysRevA.102.023303. URL `https://link.aps.org/doi/10.1103/PhysRevA.102.023303`.

[54] A. Zong, A. Kogar, Y. Bie, T. Rohwer, C. Lee, E. Baldini, E. Ergeçen, M. Yilmaz, B. Freelon, E. Sie, H. Zhou, J. Straquadine, P. Walmsley, P. Dolgirev, A. Rozhkov, I. Fisher, P. Jarillo-Herrero, B. Fine, and N. Gedik. Evidence for topological defects in a photoinduced phase transition. *Nature Physics*, 15, 01 2019. doi: 10.1038/s41567-018-0311-9.

A | Time (Taylor) expansion

A further route which we took at first after Chapter 2.1.2 is making a *time (Taylor) expansion* instead of a frequency (Bessel) expansion. This approach yields much less accurate results, especially at higher intensities (as we will see in a moment), so we will not consider it as a proper way to proceed. Though, it is interesting to show this approach both for completeness and because it is the route that is followed in STRIPE.

Let us reprise Eq. (2.1.41), in which the frequency expansion was not yet performed. If we recall the Taylor expansion of the exponential function

$$e^x = \sum_{n=0}^{+\infty} \frac{x^n}{n!} \tag{A.0.1}$$

we may expand our function $f(t,\tau)$ too. We do it as such:

$$f(t,\tau) = E_{XUV}(t+\tau) \cdot \left[1 + i\frac{p_C}{\omega_0^2} E_{IR}(t) + \frac{1}{2}\left(i\frac{p_C}{\omega_0^2} E_{IR}(t)\right)^2 + \frac{1}{6}\left(i\frac{p_C}{\omega_0^2} E_{IR}(t)\right)^3 + ...\right] \tag{A.0.2}$$

Provided we keep a low enough intensity, we can consider solely the first order, which is responsible for the first sideband:

$$f(t,\tau) = E_{XUV}(t+\tau) + E_{XUV}(t+\tau) \cdot i\frac{p_C}{\omega_0^2} E_{IR}(t) \tag{A.0.3}$$

Hence, we are able to find the maximum of the SB^+ amplitude, given a normalization over the XUV field:

$$SB_0^+ = \frac{p_c^2}{\omega_0^4}\left(\frac{E_0}{2}\right)^2 \frac{1}{\sqrt{1+\frac{\tau_{XUV}^2}{\tau_{IR}^2}}} \tag{A.0.4}$$

Similarly, for the second sideband we can write

$$SB_0^{2+} = \frac{1}{4}\frac{p_c^4}{\omega_0^8}\left(\frac{E_0}{2}\right)^4 \frac{1}{\sqrt{1+2\frac{\tau_{XUV}^2}{\tau_{IR}^2}}} \tag{A.0.5}$$

An issue immediately presents once we take a closer look at these equations. While in the frequency expansion each Bessel function corresponds *exactly* to a sideband, here each odd order of expansion actually gives a small contribution to the previous odd orders, and the same happens for even ones. For instance, the fourth order of expansion will appear not only in SB^{4+}, but also in SB^{2+} and in MB; the same will happen for SB^{5+}, contributing to both SB^{3+} and SB^{+}.

Furthermore, another glaring difference from the frequency expansion is the dependence of the sideband amplitudes on a simple power of the field E_0. This results in a model which is accurate exclusively at low intensities, as illustrated in Figure A.1.

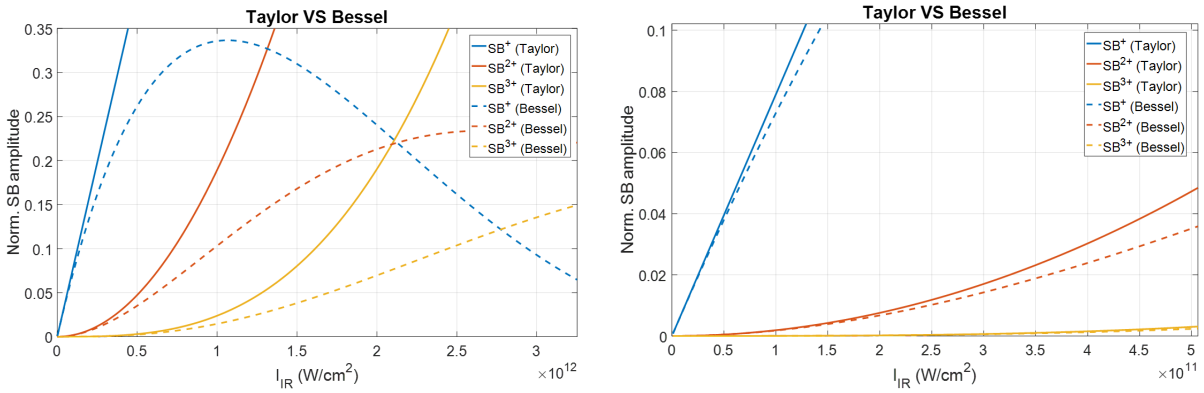

(a) (b)

Figure A.1: Comparison between Taylor expansion and generalised Bessel expansion.

We can also observe this disagreement between models by examining the following graphs:

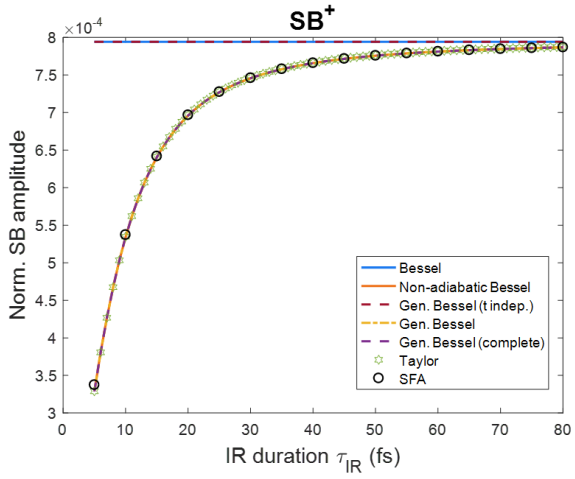

(a) $I_{IR} = 10^9 \frac{W}{cm^2}$, $\tau_{XUV} = 11$ fs.

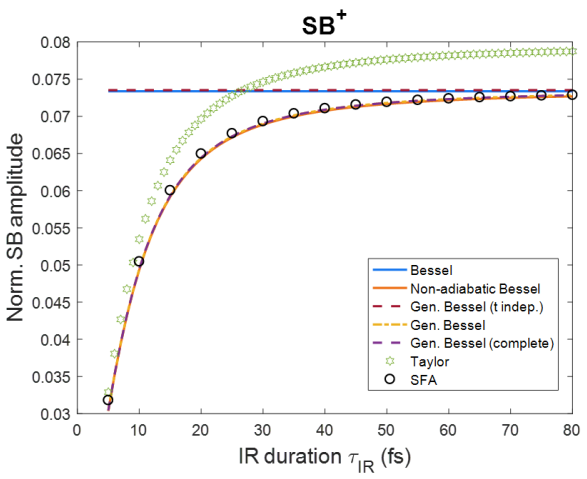

(b) $I_{IR} = 10^{11} \frac{W}{cm^2}$, $\tau_{XUV} = 11$ fs.

Figure A.2: Dependence of the amplitude of SB^+ on τ_{IR}. In these graphs the following models are compared: the time-independent Bessel, the non-adiabatic Bessel, the time-independent generalised Bessel, the truncated generalised Bessel, the complete generalised Bessel, the Taylor expansion, and the SFA model.

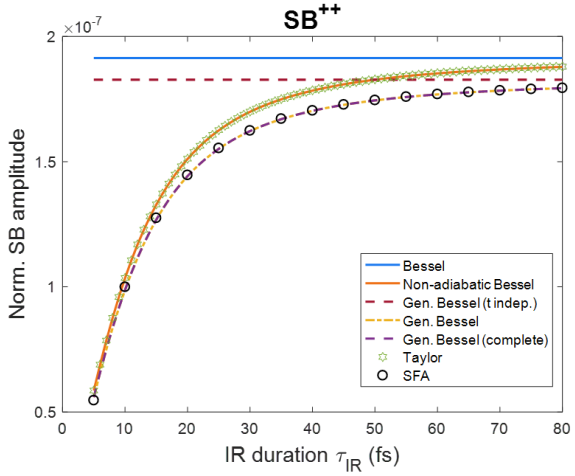

(a) $I_{IR} = 10^9 \frac{W}{cm^2}$, $\tau_{XUV} = 11$ fs.

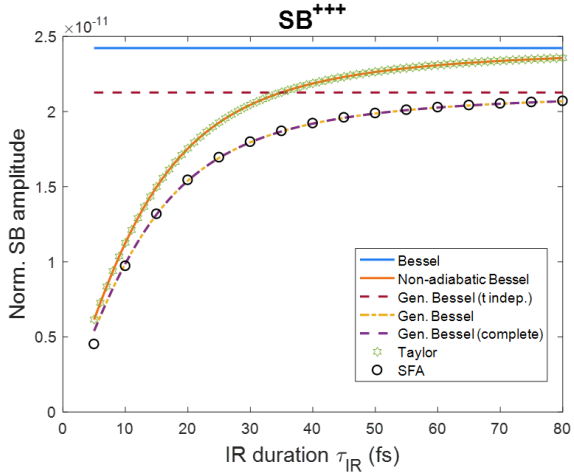

(b) $I_{IR} = 10^9 \frac{W}{cm^2}$, $\tau_{XUV} = 11$ fs.

Figure A.3: Dependence of the amplitude of SB^+ on τ_{IR}. In these graphs the following models are compared: the time-independent Bessel, the non-adiabatic Bessel, the time-independent generalised Bessel, the truncated generalised Bessel, the complete generalised Bessel, the Taylor expansion, and the SFA model.

It is apparent that if we take SB^+ into account, the Taylor expansion results to be a valid model at low intensities. Then, the more I_{IR} increases, the higher the Taylor curve will be,

rapidly parting from the other models (we have a large distance between models already at $I_{IR} \simeq 10^{11} \frac{W}{cm^2}$). Concerning SB^{2+} and SB^{3+} instead, we already notice a distance between Taylor expansion and SFA model and generalised Bessel functions. A steady overlap with the non-adiabatic Bessel model can be found at low intensities, which lasts until the intensity reaches a value of $I_{IR} \simeq 10^{11} \frac{W}{cm^2}$.

In order to correct for high intensities we could use three coefficients a, b, and c to modify the final formula as follows

$$SB_0^+ = \frac{p_c^2}{\omega_0^4} \left(\frac{E_0}{2} \right)^2 \frac{a}{\sqrt{1 + b \cdot (\frac{\tau_{XUV}}{\tau_{IR}})^c}}$$

and the same could be done for the other sidebands as well.

The only issue is that such coefficients would require to be found on a case-by-case basis, without a clear pattern or behaviour. Hence, we will refrain from using this correction. In Figure A.4, an example of the original versus the corrected Taylor model. All the previous models are represented as well.

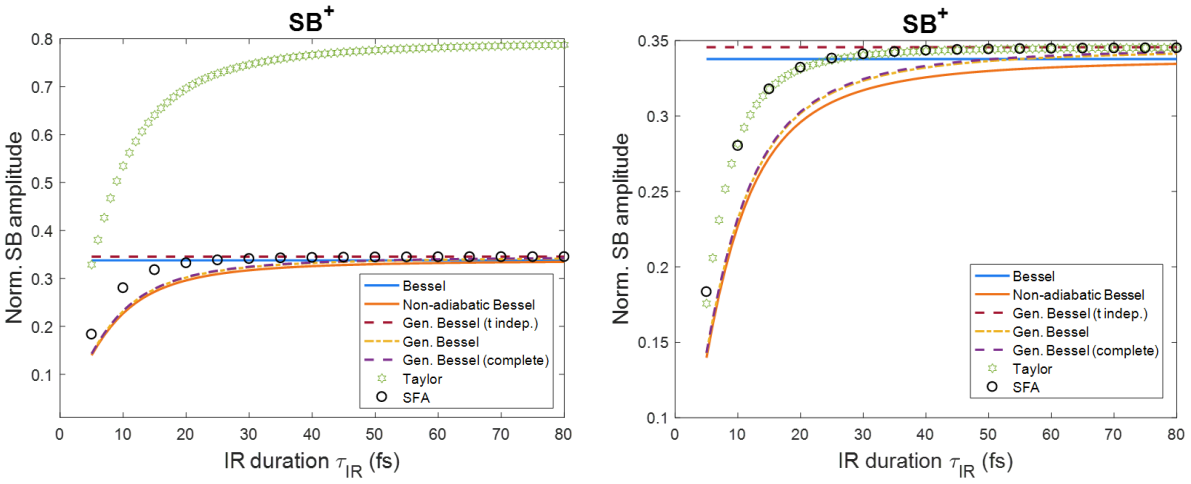

(a) (b)

Figure A.4: Dependence of the amplitude of SB^+ on τ_{IR}. Calculated using $I_{IR} = 10^{12} \frac{W}{cm^2}$ and $\tau_{XUV} = 11$ fs. (a) Original model; (b) corrected model. In this instance, $a = 0.435$, $b = 0.4$, and $c = 2.5$.

B | Two-time approach

In Eq. (2.2.2), the Jacobi-Anger expansion was employed. The use of this formula was justified by the fact that we only considered monochromatic fields, thus having no time dependence inside the argument of the Bessel functions. In actuality, our experiments are going to employ long pulses to simulate the effect of a monochromatic wave, which do possess a dependence on time. Hence, we will have that $A_0 = A_0(t)$, for which the Jacobi-Anger expression might not be applicable. The following appendix serves as a proof that we may still apply our formulas of Chapter 2.2 also in case of a time-dependent A_0.

In [31] the following approach was used, which can be then adapted to our specific case. We start by taking into account the TDSE in SAE approximation in a particular frame of reference called *Kramer-Henneberger*, which takes the form of

$$-i\frac{\partial}{\partial t}\Psi_{KH}(\mathbf{r},t) = \left(-\frac{1}{2}\boldsymbol{\nabla}^2 + V(\mathbf{r}+\alpha(t))\right)\Psi_{KH}(\mathbf{r},t) \tag{B.0.1}$$

where the coupling with the laser field is indicated exclusively by the shift $\alpha(t)$. Considering a potential $V(\mathbf{r}+\alpha(t))$ in which $\alpha(t) = \alpha_0(t)\cos(\omega_0 t + \varphi)$, we can introduce a *two-time potential* $\bar{V}$ such that:

$$\bar{V}(\mathbf{r},t,t') = V(\mathbf{r}+\alpha_0(t)\cos(\omega_0 t' + \varphi)) \tag{B.0.2}$$

in which we considered a slower evolution in time of α_0 than that of the cosine, hence justifying the presence of both t and t'. With that in mind, we can expand $V(\mathbf{r},t)$ in Taylor series, so to have:

$$V(\mathbf{r},t) = \sum_m \tilde{V}_m e^{-im\omega_0 t} \tag{B.0.3}$$

with the single components $\tilde{V}_m$ which can be calculated through the integral in Eq. (B.0.4):

$$\tilde{V}_m = \frac{1}{T_{IR}} \int_0^{T_{IR}} \bar{V}(\mathbf{r}, t, t') e^{im\omega_0 t'} dt' \tag{B.0.4}$$

having $T_{IR} = \frac{2\pi}{\omega_0}$ as the period of the IR pulse. It is possible to verify the correctness of the previous statements as such:

$$\begin{aligned} V(\mathbf{r}, t) &= \sum_m \left(\frac{1}{T_{IR}} \int_0^{T_{IR}} \bar{V}(\mathbf{r}, t, t') e^{im\omega_0 t'} dt' \right) e^{-im\omega_0 t} = \\ &= \frac{1}{T_{IR}} \int_0^{T_{IR}} \bar{V}(\mathbf{r}, t, t') \sum_m e^{im\omega_0 (t'-t)} dt' = \\ &= \frac{1}{T_{IR}} \int_0^{T_{IR}} \bar{V}(\mathbf{r}, t, t') \delta_\omega(t' - t) dt' = \\ &= \frac{1}{T_{IR}} \int_0^{T_{IR}} \bar{V}(\mathbf{r}, t) dt' = V(\mathbf{r}, t) \end{aligned}$$

□

In our case, the aforementioned potentials are equal to

$$\begin{aligned} V(\mathbf{r}, t) &= e^{ip_C \frac{A_0(t)}{\omega_0} \sin(\omega_0 t)} \\ \bar{V}(\mathbf{r}, t, t') &= e^{ip_C \frac{A_0(t)}{\omega_0} \sin(\omega_0 t')} \end{aligned} \tag{B.0.5}$$

where we can assume that $A_0(t)$ evolves more slowly than $\sin(\omega_0 t')$ thanks to the SVEA. From this and from Eq. (B.0.3) and Eq. (B.0.4) we calculate:

$$\tilde{V}_m(t) = \frac{\omega_0}{2\pi} \int_0^{\frac{2\pi}{\omega_0}} e^{ip_C \frac{A_0(t)}{\omega_0} \sin(\omega_0 t')} e^{im\omega_0 t'} dt' \tag{B.0.6}$$

If we apply again the Jacobi-Anger expansion of Eq. (2.2.1) we manage to obtain

$$\begin{aligned} \tilde{V}_m(t) &= \frac{\omega_0}{2\pi} \int_0^{\frac{2\pi}{\omega_0}} \sum_{n=-\infty}^{+\infty} J_n \left(p_C \frac{A_0(t)}{\omega_0} \right) e^{in\omega_0 t'} e^{im\omega_0 t'} dt' = \\ &= \frac{\omega_0}{2\pi} \sum_{n=-\infty}^{+\infty} J_n \left(p_C \frac{A_0(t)}{\omega_0} \right) \int_0^{\frac{2\pi}{\omega_0}} e^{i(n+m)\omega_0 t'} dt' = \\ &= \frac{\omega_0}{2\pi} J_{-m} \left(p_C \frac{A_0(t)}{\omega_0} \right) \frac{2\pi}{\omega_0} = \\ &= J_{-m} \left(p_C \frac{A_0(t)}{\omega_0} \right) \end{aligned} \tag{B.0.7}$$

in which we have that $\int_0^{\frac{2\pi}{\omega_0}} e^{i(n+m)\omega_0 t'} dt' \neq 0 \quad iif \quad n = -m$. Then, if we substitute into the first equation of Eq. (B.0.3) we find

$$V(\mathbf{r}, t) = \sum_m \tilde{V}_m e^{-im\omega_0 t} = \sum_m J_{-m}\left(p_C \frac{A_0(t)}{\omega_0}\right) e^{-im\omega_0 t} \tag{B.0.8}$$

As a last step, we can substitute $n = -m$ to get the final expression, which is

$$V(\mathbf{r}, t) = \sum_{n=-\infty}^{+\infty} J_n\left(p_C \frac{A_0(t)}{\omega_0}\right) e^{in\omega_0 t} \tag{B.0.9}$$

What we just found is formally the same as Eq. (0.1.5), indicating that $J_n\left(p_C \frac{A_0(t)}{\omega_0}\right)$ represents the amplitude of our sidebands, which is what we found through the frequency expansion as well. Therefore, we can state that in our conditions Eq. (2.2.2) may be safely applied, even in the presence of a time-varying argument.

List of Figures

Acknowledgements

I wish to thank Professor Matteo Lucchini and Professor Mauro Nisoli for giving me the opportunity to conduct my thesis work in one of their Attosecond Research Center laboratories, and for always being open and willing to advise and aid me.

I would like to thank Fabio, for guiding me through all my thesis work, for showing me the ropes of this job, and for his patience in explaining all the concepts and procedures. He treated me like a colleague and a friend from the beginning, and for this I am grateful.

A special mention goes to everyone working in the lab. They encouraged me throughout the whole experience, lending me their knowledge and their expertise. Most importantly, they welcomed me and showed me both their professional and their human side.

I wish to thank from the bottom of my heart my "brothers-in-arms", Federico, Marco and Niki. This accomplishment would not have been possible without their emotional support and without the reciprocal assistance during these trying years in this course of study.

Then, I have to express my gratitude towards Marta and Gabriele, my dearest friends. I cannot even put into words how significant this relation with them has been along my journey. I could not have hoped for better souls to share moments with, both inside and outside Politecnico.

Finally, the warmest, most heartfelt thank you goes to my parents, Dario and Anna. They have always encouraged me in every and any endeavour, supported me, put up with me. They have always believed in me even when I did not, and they have always stood by my side. So much so, that by now they probably know as much physics as I do...

To conclude, I would like to acknowledge everyone who I have not mentioned, yet has been part of my personal and professional growth. My teachers, my friends, and all those whose actions left a mark in my path. To all of them, I say thank you.

Ringraziamenti

Desidero ringraziare il Professor Matteo Lucchini e il Professor Mauro Nisoli per avermi concesso l'opportunità di svolgere la tesi in uno dei loro laboratori all'interno dell'Attosecond Research Center, e per essere sempre stati aperti e disponibili a consigliarmi ed aiutarmi.

Vorrei ringraziare Fabio, per avermi guidato attraverso tutto il lavoro di tesi, per avermi insegnato i ferri del mestiere, e per la pazienza che ha avuto nello spiegarmi tutti i concetti e le procedure. Mi ha trattato come un collega e un amico fin dall'inizio, e per questo gli sono grato.

Una menzione speciale va a tutti coloro che lavorano in laboratorio. Mi hanno incoraggiato durante tutta questa esperienza, prestandomi la loro conoscenza e competenza, ma soprattutto mi hanno accolto, mostrandomi sia il loro lato professionale che quello umano.

Voglio porgere un sincero ringraziamento ai miei "compagni d'arme", Federico, Marco e Niki. Questo traguardo non sarebbe stato possibile senza il loro supporto morale e senza il sostegno reciproco che ci siamo dati in questi anni impegnativi per affrontare questa facoltà.

Devo inoltre esprimere la mia gratitudine nei confronti di Marta e Gabriele, i miei più cari amici. Non riesco nemmeno ad esprimere quanto questo legame con loro sia stato fondamentale nel mio cammino. Non avrei potuto sperare in anime migliori con cui condividere momenti, sia dentro che fuori dal Politecnico.

Infine, il grazie più sentito e di cuore lo riservo per i miei genitori, Anna e Dario. Mi hanno sempre incoraggiato in ogni impresa, sostenuto, sopportato. Hanno sempre creduto in me anche quando io stesso non lo facevo, e sono sempre rimasti al mio fianco. Così tanto, che ora probabilmente conoscono la fisica tanto quanto me...

Per concludere, vorrei ringraziare tutti coloro che non ho menzionato ma che sono stati parte della mia crescita professionale e personale. I miei insegnanti, i miei amici, e tutti coloro le cui azioni hanno lasciato un segno nel mio percorso. A tutti loro dico grazie.